MECHANICAL METAMATERIALS FOR WAVE CONTROL: EFFECTS OF MODULARITY AND NONLINEARITY

BY

SETARE HAJAROLASVADI

DISSERTATION

Submitted in partial fulfillment of the requirements
for the degree of Doctor of Philosophy in Civil Engineering
with a concentration in Computational Science and Engineering
in the Graduate College of the
University of Illinois Urbana-Champaign, 2021

Urbana, Illinois

Doctoral Committee:

Associate Professor Ahmed E. Elbanna, Chair and Director of Research
Professor Larry A. Fahnestock
Assistant Professor Kathryn H. Matlack
Professor Alexander F. Vakakis

Abstract

Periodic structures have been a focus of research for decades due to their unprecedented wave-control functionalities. This has made them potential candidates for applications such as wave-filtering, vibration/seismic isolation, and wave-guiding. Periodic systems fall under two broad categories: phononic structures and metamaterials, both of which have been extensively investigated. More recent efforts focus on how to make these systems even more versatile and adaptable. As such, the objective of this dissertation is two-fold:

1. to investigate a modular approach to the design of metamaterials in an attempt to broaden the design space and achieve new wave-control functionalities that go beyond that of the conventional designs proposed.

2. to exploit nonlinearities for realizing passive-adaptive wave-control. In the former, we primarily focus on a special category of modular systems in which elements are entangled through periodic connections along their length. We explore the second area in the context of surface waves pursuant to our interest in potential seismic applications.

We start by a theoretical investigation of dispersion properties for a metamaterial beam that consists of flexural elements periodically coupled (entangled) along their length. We will show that the structure possesses multiple Bragg scattering and local resonance band gaps, and has unique wave-filtering properties unlike its constituents. We will also show how static tuning of connection properties can be used to alter the system's band structure. Next, entangled monoatomic chains are considered in two configurations. One is a configuration where each mass in one chain is connected to its corresponding mass in the other chain (full coupling). The other, consists of chains that are periodically coupled only at certain locations (partial coupling). We derive closed-form dispersion relations for both cases and discuss their eccentric dynamic properties, such as double-speed wave propagation zones, emergence of negative group velocity dispersion branches and flat bands. For each study, we use numerical

simulations to verify our theoretical results, and present example devices targeted at wave propagation control using finite prototypes of each meta-structure.

In the remainder of this work, we focus our attention on embedding nonlinearity in the design of metamaterials to control surface waves in a passive-adaptive manner. First, we present an approximate theoretical framework for how Rayleigh waves interact with a periodic array of Duffing oscillators. Our analysis indicates that the presence of nonlinearities makes dispersion amplitude-dependent. We further show that for hardening (softening) nonlinearities, dispersion branches shift towards higher (lower) frequencies as the amplitude of motion increases. In the light of this promising preliminary results, we attempt to realize the phenomenon in an experiment. In order to do this, we leverage a compact experimental setup consisting of a plate, serving as an elastic substrate, and bead-magnet assemblies, in lieu of nonlinear resonators. We will study the dynamics of the constituting elements of this structure in detail to present, for the first time, experimental evidence of amplitude-dependent dispersion for surface acoustic waves.

The findings of this two-part study will inform the design of more versatile metamaterials at different scales. Finally, we will also discuss some promising future directions that may be considered as both short-term and long-term extensions to this work.

To the love of my life, Kiomars.

Acknowledgments

I would like to start by thanking my advisor, Professor Ahmed Elbanna. He's inspired me throughout the years with fascinating ideas and has been tremendously supportive of the different paths I've chosen to explore. His openness to discussing the most trivial questions and his passion for exploring new areas of science are traits that I hope to be able to carry with me throughout my own profession. I would also like to thank my co-adviser Professor Larry Fahnestock, who's been a great mentor to me. I have learnt a great many things from him, in both research and teaching. I extend my gratitude to my PhD committee members, Professors Kathryn Matlack and Alexander Vakakis, who inspired me time and again in the courses I took with them and supported me in research with stimulating discussions.

During the last year of my PhD, I was fortunate enough to visit Caltech and work with Professors Chiara Daraio, Paolo Celli (now at Stony Brook University) and Domniki Asimaki. I cannot express enough thanks to them for sharing their knowledge with me so generously.

Apart from the great mentors I've had, I would also like to acknowledge my group members: Darin Peetz, Ahmad Ghareeb, Mohamed Ezze El-Din, Qianli Chen and Xiao Ma, who have fueled my research by being open to discussions. I would also like to acknowledge Brittany Kamai, Danilo Kusanovic, and Joaquin Garcia-Suarez for their friendship and intellectual contribution to my research while I was at Caltech.

There are not enough words that can express how thankful I am to my parents, Pari and Hasan. They were my first mentors, teachers and motivators as a child. They helped me follow my dreams and supported me through this journey. To my sisters, Neda and Nooshin: I'm blessed to have you and your support in my life.

Last but not least, I would like to thank my husband, Kiomars. I'm grateful for his unconditional love and support throughout the years. The road through grad school is not a straight one. He's constantly been my biggest motivator and source of inspiration.

Contents

Chapter 1

Introduction

1.1 Fundamentals of wave propagation in periodic structures

Periodic structures have been widely used to control the propagation of acoustic and elastic waves. A periodic structure is one that exhibits periodicity in either material properties, internal geometry or boundary conditions [1]. The study of these structures may be traced back to Newton's attempt to measure the speed of sound in air and Rayleigh's early studies on the propagation of waves in continuous periodic systems [2] and has, ever since, found applications for wave-control over broad length scales: from Nanotubes, MEMS filters and biomedical implants [3, 4, 5, 6, 7] to multi-span bridges, pipelines [8, 9, 10, 11] and aircraft structures [12, 13, 14] (Figure 1.1).

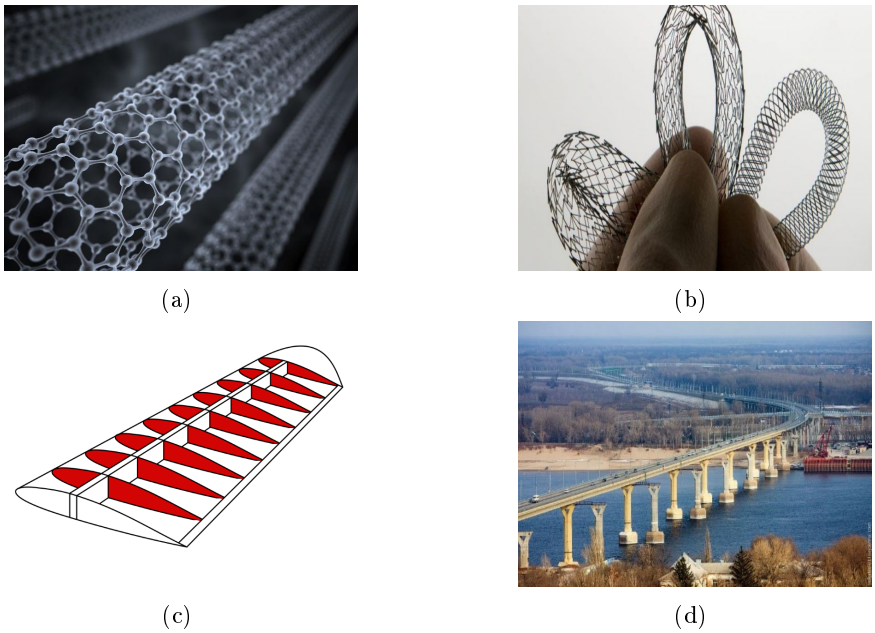

(a) (b) (c) (d)

Figure 1.1: Examples of structures systems, in the order of increasing length scale: (a) carbon nanotubes (from thoughtco.com/what-are-carbon-nanotubes-820395), (b) heart stents (from augustahealth.com/health-focused/cardiology-101-understanding-heart-stents), (c) aircraft ribs (from quora.com/Aviation-What-is-Wing-Spar-Ribs), and (d) multi-span bridge (from pinterest.com/pin/314407617714507401/).

Periodic structures may be considered as the spatial repetition of a so-called unit-cell. The fundamental wave propagation properties of an infinite periodic system can be captured by studying the dynamics of the corresponding unit-cell by assuming plane-wave solutions and imposing Floquet-Bloch boundary conditions. Bloch's theorem states that the change in complex wave amplitude of a non-attenuating propagating wave in an infinitely-periodic system does not depend on the location of the unit cell within the structure [15]. This will manifest itself as a set of relationships between displacements/forces on the boundaries of the unit-cell. The outcome of a unit-cell analysis is a set of eigenvalue problems, solving which leads to the dispersion relation for the overall system. The dispersion relation of a structure contains information about the inter-dependency of wave number k and frequency ω of waves that freely propagate in the system. This function may be visualized using a band diagram or dispersion curve plot. Figure 1.2c shows the dispersion curve for the well-known 1-D monoatomic lattice. Band diagrams contain important information about the elastodynamics of the structure. For example, the tangent and secant slopes at any point show wave group velocity $c_g = d\omega/dk$ and phase velocity $c_p = \omega/k$. In the next section, two broad categories of periodic structures will be discussed.

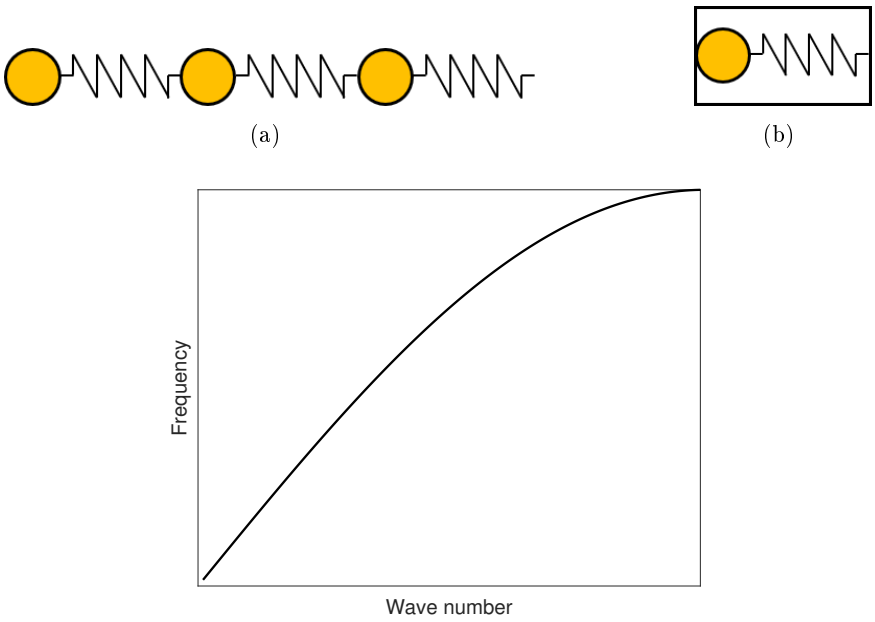

(a) (b)

(c)

Figure 1.2: 1-D monoatomic lattice: (a) infinite lattice configuration, (b) unit-cell, (c) band diagram.

1.2 An overview of phononic structures and metamaterials

It has been well-established that waves in certain frequency ranges cannot freely propagate in periodic systems due to the existence of band gaps in their frequency spectra [1]. This feature has made them potential candidates for applications such as vibration and seismic isolation [16, 17, 18], wave-guiding [19, 20, 21] and cloaking [22, 23, 24]. Two mechanisms have been identified for band gap formation in periodic systems; Bragg scattering (BS) and local resonance (LR). Accordingly, periodic systems may be categorized in two main groups: phononic structures and metamaterials. In the remainder of this section, we give a brief overview of each category and their potential applications.

A phononic structure/crystal is a spatially-periodic arrangement of unit-cells containing components with different geometrical or material properties. Periodic layered composites and engineering structures, such as aircraft ribs and beam-plate systems inspired the study of this category of periodic systems. Phononic structures mainly owe their wave-control characteristics to Bragg scattering and interference effects between the periodic constituents of the system. Phononic systems have been used to realize a wide range of functionalities, from vibration isolation [25, 26] and noise filtering [27, 28] to sensing [29, 30] and wave rectification [31, 32]. Band gaps in these systems occur at wavelengths that are proportional to the periodicity length. This limits their practicality for low-frequency applications.

The seminal work of Liu et al. [33], however, showed that gaps can occur at frequencies nearly two orders of magnitude lower than that of the Bragg frequency if local resonance is exploited. Periodicity is not a prerequisite for such systems but it's exploited to simplify the analysis. This gave born to metamaterials - another group of periodic systems comprising of a periodic arrangement of locally-resonant inclusions in a host medium. Band gaps in these systems form not only due to Bragg scattering but also as a result of local resonances. Therefore, tuning the resonance frequency of the inclusions allows for compact designs with sub-wavelength features with applications from seismic isolation [18, 34, 17] to radiofrequency devices [35]. Local resonance band gaps are usually narrow in width. This restricts the frequency range over which they can operate. Metamaterials may also be engineered to show other eccentric characteristics, such as negative effective dynamic mass density and or modulus. These properties have found applications in wave-focusing [36, 37] and subwavelength imaging [38, 39].

Unconventional designs have been recently proposed that offer a broader range of dispersion characteristics [40]. Among these novel configurations are the concepts of resonator-to-resonator interactions [41, 42] and nonlocal resonances [43]. For example, in Beli et al. 2018 [42], the interaction between

the transverse and rotational modes of a resonator chain consisting of beam elements has been used to achieve a wider band gap in comparison to the case where the resonators perform independently. The authors show how certain Bloch wave modes of the system correspond to the resonance frequencies of the resonator chain. DePauw et al. 2018 [43] propose a configuration called a Phononic Resonator in which each resonator can directly interact with the neighboring masses in the main chain. It is then shown how tuning the stiffness and mass ratios of the main and resonator masses can change the nature of the attenuation mechanism leading to the system behaving as a Phononic Crystal or an Acoustic Metamaterial.

1.3 Modularity in design

Phononic structures and metamaterials come in different forms. For the former, the majority of proposed designs have a layered architecture, in which elements of different material or geometry are used in a periodic arrangement. Design for locally-resonant metamaterials often rely on embedding inclusions with engineered resonance properties in a host material. This work proposes a novel approach to design by introducing the concept of modularity. Here, modularity in design refers to the idea of creating complex systems from a library of building blocks (Figure 1.3). One can envision such library to contain various structural elements of different load-bearing properties and material/geometric designs. Connection between these structural members is idealized as different types of springs (axial, torsional, etc.) as shown in Figure 1.3. As we will discuss in detail in later chapters, this modular approach to design of periodic systems has the following benefits:

- It broadens the design space.
- It enriches the dispersion characteristics of the structure.
- It gives rise to new wave phenomenon and wave-control properties.

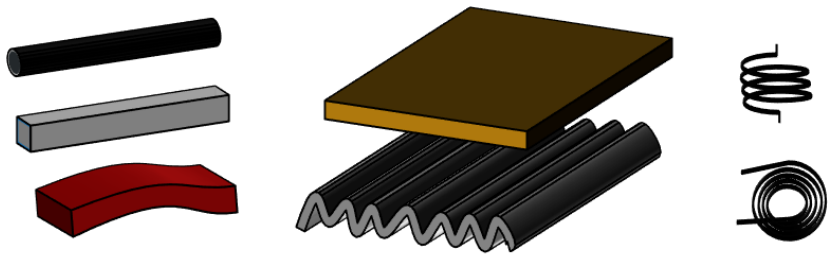

Figure 1.3: Library of structural elements used for modular design.

In this work, we have primarily focused on a special category of modular systems, in which structural elements are connected periodically along their length instead of in series, such as in composite designs. Studying structures that are periodically connected in parallel could be traced back to Sen Gupta's work in 1970 on the so-called rib-skin structures [44], encountered in airplane applications. These structures consist of a pair of plates (skins) joined periodically in parallel by another set of orthogonal plates (ribs). The ribs are usually modeled as rigid bodies while the skins are modeled as elastic beams. Gupta showed that the dispersion relation of one such structure is quadratic in $\cosh \mu$, where μ is the propagation constant, and identified the propagation and attenuation zones. More work has been done since on stiffened plates and beams in the context of periodic systems [14, 45, 46]. More recently, Chen and Elbanna studied the coupling of a pair of bars in parallel and showed that tailoring the properties of the two elastic members may lead to extreme attenuation zones in the band structure of the system. The idea was then used to realize a mechanical switch that is used to modulate elastic waves [47]. On another front, studies on mass-spring chains coupled in parallel have uncovered analogies to quantum-mechanical systems and proved that such structures allow for the propagation of elastic waves with nonconventional topology [48, 49, 50, 51]. More investigation in this area could inform and facilitate the design of systems with desirable wave-control functionalities.

1.4 Effects of Nonlinearity

Although linear metamaterials exhibit many interesting properties, recent works have shown that nonlinear periodic structures offer a myriad of opportunities for enhanced control over wave transmission. These include but are not limited to response tunability/localization [52, 53, 54, 55], frequency conversion [56, 57], irreversible energy transfer and nonreciprocity [58, 59, 60] or merely broadening the frequency region over which strong attenuation is achieved [61, 62]. The classical dispersion analysis methods for linear elastic metamaterials no longer hold in the presence of nonlinear effects.

Multiple frameworks have been developed to allow for integrating different types of nonlinearity directly in the dispersion analysis. For example, Narisetti showed how a modified version of perturbation approaches, such as the method of Lindstedt-Poincaré or Multiple Scales, may be used to determine the band structure of weakly nonlinear periodic structures [63]. In the same work, the author also presents a framework for tackling strong nonlinearities by using the Harmonic Balance method. Manktelow extended this work to account for wave-wave interactions in nonlinear periodic media [64]. More recently, Khajehtourian presented an exact, closed-form formulation for the treatment of nonlinearity

in the strain-displacement gradient relation [65]. However, not much research has been conducted on the interaction of waves in continuous media with nonlinear local resonators. Recently, Silva used a perturbation approach for studying wave-wave interactions in discrete metamaterials with weakly nonlinear quadratic local interactions [66, 67]. The study revealed that energy exchange may occur between propagating and evanescent waves. An experimental realization was offered in [68].

Considering the above, investigating the interaction of waves propagating in continuous media with a periodic array of nonlinear local resonators is of interests in two regards: one, to develop a unified theoretical framework for this class of problems, and two, in order to design metamaterials with new functionalities.

1.5 Motivation and outline

The objective of the present work is two-fold:

- to investigate a modular approach to the design of metamaterials in an attempt to broaden the design space and achieve new wave-control functionalities that go beyond the conventional designs proposed. We primarily focus on a special category of modular systems, in which structural elements are connected periodically along their length, and investigate their dispersion characteristics, wave-control properties and applications.

- to investigate the interaction of waves propagating in continuous media with discrete nonlinear local resonators. Pursuant to our interest in structural and earthquake engineering applications, we specifically focus our attention on the effect of discrete nonlinear local resonators on the propagation of surface waves.

The work is organized as follows: The first two chapters are dedicated to theoretical and numerical studies on two classes of structural systems coupled in parallel. One contains continuous flexural beam elements and another consists of discrete lattices. Both configurations follow a modular approach to design in which structural systems with previously known dispersion characteristics are coupled to create a new structure with richer dynamic properties and potential applications for wave and vibration control. Chapters three and four focus on how periodic nonlinear local resonances may be exploited to realize amplitude-dependent dispersion characteristics for surface acoustic waves. More specifically, chapter three considers the interaction of Rayleigh waves with Duffing-type oscillators, and presents a theoretical framework for dispersion analysis using the effective medium approach. Chapter

four proposes a compact table-top experimental setup for realizing amplitude-dependent dispersion for surface acoustic waves.

The findings of this two-part study will inform the design of more versatile metamaterials at different scales. Finally, we will also discuss some promising future directions that may be considered as both short-term and long-term extensions to this work.

Chapter 2

Dynamics of metamaterial beams: periodically-coupled flexural elements

The content of this chapter has been published in the Journal of Physics D: Applied Physics [69]

2.1 Introduction

Wave propagation in periodic structures has been investigated for decades: from large-scale structures, such as multi-story buildings, multi-span bridges and pipelines [8, 9, 10, 11] to atomic lattices [4]. These structures have been a focus of attention due to their wave-filtering properties. It has been well-established that waves in certain frequency ranges cannot freely propagate in periodic systems due to the existence of band gaps in their frequency spectra [1]. This feature has made them potential candidates for applications such as vibration and seismic isolation [16, 17, 18], wave-guiding [19, 20, 21] and cloaking [22, 23, 24]. Two mechanisms have been identified for band gap formation in periodic systems: Bragg scattering (BS) and local resonance (LR). Bragg band gaps occur due to multiple scattering and interference effects between the periodic constituents of the system. Hence, these gaps occur at wavelengths comparable to the structural periodicity. The seminal work of Liu et al. [33], however, showed that gaps can occur at frequencies nearly two orders of magnitude lower than that of the Bragg frequency if local resonance is exploited. In an attempt to further enhance the dispersion characteristics of these systems, researchers have recently proposed novel designs that aim to combine the features of both mechanisms. These designs range from systems with interconnected resonators [41, 42] to configurations with resonators directly attached to neighboring masses in the host structure [43].

Periodic beams have been particularly studied to a great extent in literature. As early as the 1960s, the natural frequencies and steady-state responses of beams with periodic supports and periodic impedances were studied [70, 71]. Since then, many researchers have investigated flexural vibration band gaps in beams with various periodicity features. Attention was first drawn to periodic beams with

a binary configuration, in which the unit cell consists of two flexural elements with different material or geometric properties placed in series [8, 72, 73]. The Bragg scattering mechanism is responsible for band gap formation in these structures. More recent studies have focused on Locally Resonant (LR) beams, in which a periodic array of local resonators leads to the emergence of band gaps in the frequency spectra of the system [74, 75, 76, 77, 78, 79]. Band gaps in this class of structures form due to both BS and LR mechanisms [80, 81]. Liu and Hussein studied wave propagation in flexural beams from both categories and mathematically characterized the condition for transition between Bragg scattering and local resonance band gaps in LR beams [82]. Most research in the area of LR beams has focused mainly on the effect of discrete resonators. However, recently, Wang et al. studied a local resonant beam with continuum beam resonators and proved its effectiveness in comparison with the conventional force-only resonators [83]. Beli et al. proposed a metamaterial beam with interconnected beam attachments, forming a resonator chain. The authors showed that the interaction between the translational and rotational modes of this chain enriches the band structure in comparison to the case where the beam resonators perform independently[42].

Studying structures that are periodically connected in parallel could be traced back to Sen Gupta's work in 1970 on the so-called rib-skin structures [44], encountered in airplane applications. These structures consist of a pair of plates (skins) joined periodically in parallel by another set of orthogonal plates (ribs). The ribs are usually modeled as rigid bodies while the skins are modeled as elastic beams. Gupta showed that the dispersion relation of one such structure is quadratic in $\cosh \mu$, where μ is the propagation constant, and identified the propagation and attenuation zones. More work has been done since on stiffened plates and beams in the context of periodic systems [14, 45, 46]. More recently, Chen and Elbanna studied the coupling of a pair of bars in parallel and showed that tailoring the properties of the two elastic members may lead to extreme attenuation zones in the band structure of the system. The idea was then used to realize a mechanical switch that is used to modulate elastic waves [47].

In this chapter, we focus our attention on parallel beam elements that are periodically connected by enforcing compatibility of deformation and force balance at discrete attachment points along their length. We carry out a parametric study to show the effects of material and section properties as well as connection compliance on the band structure of the system. We, then, show that the system may possess rich dispersion properties in the low frequency ranges by tuning the parameters properly.

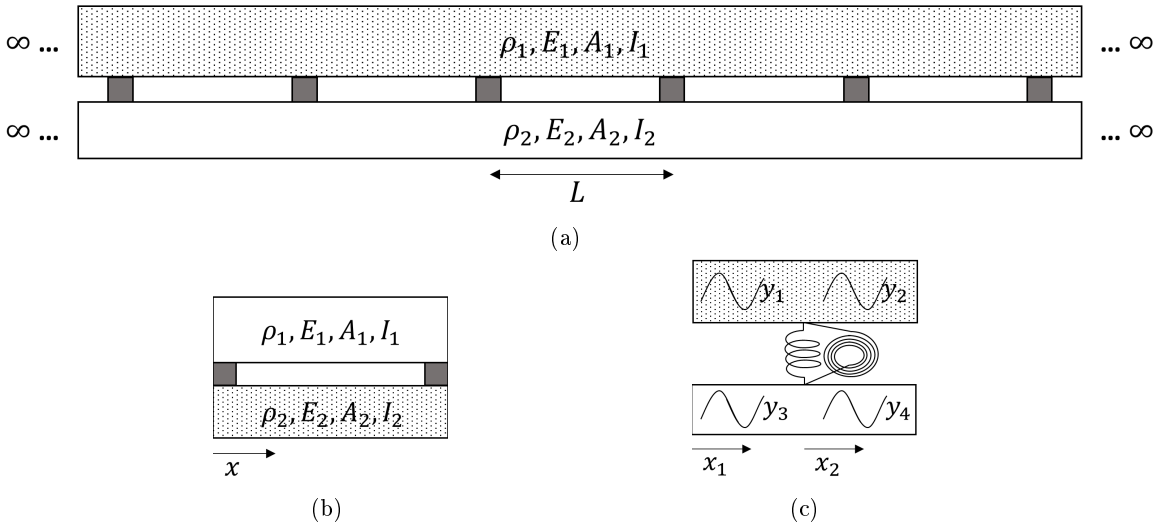

Figure 2.1: Model setup. (a) Metamaterial beam structure consisting of two uniform beams that are periodically attached. (b) Unit cell configuration for rigid connections. (c) Unit cell configuration for compliant connections.

2.2 Methods

2.2.1 Analytical model

Rigid connections The setup of the metamaterial beam with rigid connections is shown in Fig. 2.1a. The system consists of two uniform beams periodically coupled with rigid arms that enforce equal transverse displacement and rotation at the connection points between the two beam elements. The spacing of the periodic attachments is L. The dynamics of the infinite metamaterial beam is studied by deriving the governing equations for one of its unit cells (Fig. 2.1b) following the Euler-Bernoulli beam theory and assuming that the coupling of the two beams is exactly imposed at the boundaries of the unit cell. The governing equations are written as follows:

$$\frac{\partial^2}{\partial x^2}[E_1 I_1 \frac{\partial^2 Y_1(x,t)}{\partial x^2}] + \rho_1 A_1 \frac{\partial^2 Y_1(x,t)}{\partial t^2} = 0 \tag{2.1a}$$

$$\frac{\partial^2}{\partial x^2}[E_2 I_2 \frac{\partial^2 Y_2(x,t)}{\partial x^2}] + \rho_2 A_2 \frac{\partial^2 Y_2(x,t)}{\partial t^2} = 0 \tag{2.1b}$$

where, ρ and E refer to the density and Young's modulus of the beam material, respectively and A and I denote the cross-sectional area and moment of inertia of the members. The solution of the PDEs is written as $Y_1(x,t) = y_1(x)e^{i\omega t}$ and $Y_2(x,t) = y_2(x)e^{i\omega t}$, where $y_1(x)$ and $y_2(x)$ are of the following

general form:

$$y_1(x) = a_{11}\cos\frac{\sqrt{\omega}x}{\beta_1} + a_{12}\sin\frac{\sqrt{\omega}x}{\beta_1} + a_{13}\cosh\frac{\sqrt{\omega}x}{\beta_1} + a_{14}\sinh\frac{\sqrt{\omega}x}{\beta_1} \tag{2.2a}$$

$$y_2(x) = a_{21}\cos\frac{\sqrt{\omega}x}{\beta_2} + a_{22}\sin\frac{\sqrt{\omega}x}{\beta_2} + a_{23}\cosh\frac{\sqrt{\omega}x}{\beta_2} + a_{24}\sinh\frac{\sqrt{\omega}x}{\beta_2} \tag{2.2b}$$

Here, $\beta_j = \sqrt[4]{\frac{E_j I_j}{\rho_j A_j}}$ and the a_{jk} coefficients are determined by imposing the boundary conditions (BCs) with $j = 1, 2$ and k ranging from 1 to 4. Enforcing equal transverse displacements and flexural rotations at the ends of the unit cell, where the two beams are coupled with a rigid connection, gives the first set of BCs:

$$y_1(0) = y_2(0) \quad , \quad \theta_1(0) = \theta_2(0) \tag{2.3a}$$

$$y_1(L) = y_2(L) \quad , \quad \theta_1(L) = \theta_2(L) \tag{2.3b}$$

with $\theta_j(x) = \frac{dy_j}{dx}$. Since the structure is periodic, the displacements and forces associated with the two boundaries of the unit cell are related by using the Bloch theorem. This yields the second set of BCs:

$$y_1(L) = e^{iqL}y_1(0) \quad , \quad \theta_1(L) = e^{iqL}\theta_1(0) \tag{2.4a}$$

$$V(L) = e^{iqL}V(0) \quad , \quad M(L) = e^{iqL}M(0) \tag{2.4b}$$

where q is the wave number and $i = \sqrt{-1}$. Due to the coupling at the boundaries, $M(0) = M_1(0) + M_2(0)$ and $V(0) = V_1(0) + V_2(0)$ where $M_j(x) = E_j I_j \frac{d^2 y_j}{dx^2}$ and $V_j(x) = \frac{dM_j}{dx}$ denote the moment and shear force in each beam.

We introduce the variables $k_b^{(1)} = \frac{\sqrt{\omega}}{\beta_1}$ and $k_b^{(2)} = \frac{\sqrt{\omega}}{\beta_2}$ and use the propagation constant, $\mu = iqL$, for convenience. Substituting (2.2) in (2.3) and (2.4), we can construct a system of linear equations as follows

$$[C]\{a\} = 0 \tag{2.5}$$

Matrix $[C]$ is a function of material properties and the geometry of the two beam sections as well as the frequency ω and wave number q. In order for the system to have nontrivial solutions, the determinant of this matrix must be set to zero. Doing so and rearranging parameters gives the dispersion relation in the following form

$$(e^{2\mu} + e^{-2\mu}) + J_1(e^{\mu} + e^{-\mu}) + J_2 = 0 \tag{2.6}$$

or

$$\cosh^2\mu + \frac{J_1}{2}\cosh\mu + \frac{J_2-2}{4} = 0 \tag{2.7}$$

where, $J_1 = \frac{H_1}{H_3}$ and $J_2 = \frac{H_2}{H_3}$ and

$$H_1 = 2\Big[\sum_{i=1}^{2} E^{(i)}I^{(i)}\lambda^{(i)}\sum_{i=1}^{2} E^{(i)}I^{(i)}\bar{\delta}^{(i)} - \sum_{i=1}^{2} E^{(i)}I^{(i)}\bar{\lambda}^{(i)}\sum_{i=1}^{2} E^{(i)}I^{(i)}\delta^{(i)}\Big] \tag{2.8a}$$

$$H_2 = 4\Big[-\big(\sum_{i=1}^{2} E^{(i)}I^{(i)}\eta^{(i)}\big)^2 + \sum_{i=1}^{2} E^{(i)}I^{(i)}\lambda^{(i)}\sum_{i=1}^{2} E^{(i)}I^{(i)}\delta^{(i)}\Big] \tag{2.8b}$$

$$H_3 = \big(\sum_{i=1}^{2} E^{(i)}I^{(i)}\eta^{(i)}\big)^2 - \sum_{i=1}^{2} E^{(i)}I^{(i)}\bar{\lambda}^{(i)}\sum_{i=1}^{2} E^{(i)}I^{(i)}\bar{\delta}^{(i)} \tag{2.8c}$$

The superscript i indicates element number. The parameters $\lambda^{(i)}$, $\delta^{(i)}$, $\bar{\lambda}^{(i)}$, $\bar{\delta}^{(i)}$ and $\eta^{(i)}$ $(i = 1, 2)$ are defined as follows

$$\lambda^{(i)} = [\cos(k_b^{(i)}L)\sinh(k_b^{(i)}L) + \sin(k_b^{(i)}L)\cosh(k_b^{(i)}L)](k_b^{(i)}L)^3/\Delta^{(i)} \tag{2.9a}$$

$$\delta^{(i)} = [-\cos(k_b^{(i)}L)\sinh(k_b^{(i)}L) + \sin(k_b^{(i)}L)\cosh(k_b^{(i)}L)](k_b^{(i)}L)/\Delta^{(i)} \tag{2.9b}$$

$$\eta^{(i)} = [-\cos(k_b^{(i)}L) + \cosh(k_b^{(i)}L)](k_b^{(i)}L)^2/\Delta^{(i)} \tag{2.9c}$$

$$\bar{\lambda}^{(i)} = [\sin(k_b^{(i)}L) + \sinh(k_b^{(i)}L)]/(k_b^{(i)}L)^3\Delta^{(i)} \tag{2.9d}$$

$$\bar{\delta}^{(i)} = [-\sin(k_b^{(i)}L) + \sinh(k_b^{(i)}L)](k_b^{(i)}L)/\Delta^{(i)} \tag{2.9e}$$

$$\Delta^{(i)} = 1 - \cos(k_b^{(i)}L)\cosh(k_b^{(i)}L) \tag{2.9f}$$

Examining the resulting dispersion relation reveals that for arbitrary material and cross-sectional properties of the first beam element- i.e. fixed β_1-, there are only two non-dimensional parameters (namely, $\hat{\rho}\hat{A}$ and $\hat{E}\hat{I}$) that influence the dispersion relation of the system. Here, $\hat{(.)} = \frac{(.)_2}{(.)_1}$. $\hat{\rho}\hat{A}$ indicates the mass ratio between the two beams while $\hat{E}\hat{I}$ shows the stiffness ratio. In Section 3.1, we study how the location and width of the first band gap change when these parameters are varied.

Compliant connections In practice, it may be difficult to have fully-rigid connections. Here, we develop the analytical solution for the case of connections with finite translational and rotational stiffnesses K_s and K_t. The unit cell configuration alongside with the coordinate system in this case is shown in Fig. 2.1c. The governing equations as well as the general form of solution for $y_j(x)$ $(j = 1, ..., 4)$ are the same as the previous section. However, the boundary conditions are different in

this case.

The first set of BCs is determined by imposing continuity of displacements and balance of forces within each beam element:

$$y_1(L/2) = y_2(0) \quad , \quad \theta_1(L/2) = \theta_2(0) \tag{2.10a}$$

$$y_3(L/2) = y_4(0) \quad , \quad \theta_3(L/2) = \theta_4(0) \tag{2.10b}$$

$$-V_1(L/2) + V_2(0) + F_s = 0 \tag{2.10c}$$

$$-V_3(L/2) + V_4(0) - F_s = 0 \tag{2.10d}$$

$$-M_1(L/2) + M_2(0) + M_s = 0 \tag{2.10e}$$

$$-M_3(L/2) + M_4(0) - M_s = 0 \tag{2.10f}$$

In the above, F_s and M_s are the force and moment in the connector springs, respectively and are defined as follows:

$$F_s = K_s[y_2(0) - y_4(0)] \tag{2.11a}$$

$$M_s = K_t[\theta_2(0) - \theta_4(0)] \tag{2.11b}$$

The second set of BCs consists of the Bloch boundary conditions:

$$y_2(L/2) = y_1(0)e^{iqL} \quad , \quad \theta_2(L/2) = \theta_1(0)e^{iqL} \tag{2.12a}$$

$$y_4(L/2) = y_3(0)e^{iqL} \quad , \quad \theta_4(L/2) = \theta_3(0)e^{iqL} \tag{2.12b}$$

$$V_2(L/2) = V_1(0)e^{iqL} \quad , \quad M_2(L/2) = M_1(0)e^{iqL} \tag{2.12c}$$

$$V_4(L/2) = V_3(0)e^{iqL} \quad , \quad M_4(L/2) = M_3(0)e^{iqL} \tag{2.12d}$$

These boundary conditions are used to form a system of linear equations as in the previous section. The problem is formulated as in the previous case. The general solutions can be written in a similar form for all four beam elements (Fig. 2.1c), yielding sixteen unknown coefficients. Setting the determinant of the matrix of coefficients to zero gives the dispersion relation in the following form

$$(e^{4\mu} + e^{-4\mu}) + J_1^*(e^{3\mu} + e^{-3\mu}) + J_2^*(e^{2\mu} + e^{-2\mu}) + J_3^*(e^{\mu} + e^{-\mu}) + J_4^* = 0 \tag{2.13}$$

or

$$\cosh^4\mu + \frac{J_1^*}{2}\cosh^3\mu + \frac{J_2^*-4}{4}\cosh^2\mu + \frac{J_3^*-3J_1^*}{8}\cosh\mu + \frac{J_4^*-J_2^*+1}{8} = 0 \tag{2.14}$$

The dispersion relation is proven to be quartic in $\cos qL$. Again, the coefficients of this fourth-order equation are functions of the material and cross-sectional properties as well as stiffness parameters α and γ. The closed-form expressions of these coefficients will not be presented here.

2.2.2 Numerical model

Bloch mode synthesis [84] is used to determine the band structure of the system numerically. We use a standard Finite Element method to construct the mass and stiffness matrices of the unit cell. The matrices are then partitioned according to the interior and interface nodes and the Craig-Bampton method [73] is chosen to represent the normal and constraint modes. Depending on the highest frequency of interest and for the sake of computational efficiency, only a reduced set of the fixed-interface modes (FIM) is kept. Next, Bloch boundary conditions are imposed through interface nodes to create the mass and stiffness matrices of an infinite metamaterial beam. The reduced model is then used for eigenvalue analysis to determine the band structure of the periodic system. Matlab® is used for all numerical simulations in this paper.

2.3 Results

2.3.1 Infinite metamaterial beams

Parametric study of the band gap structure in rigidly-connected beams In this section, we study the parametric dependence of the first band gap characteristics in terms of the two independent variables identified in the previous section - i.e. the mass ratio and the stiffness ratio of the two beams.

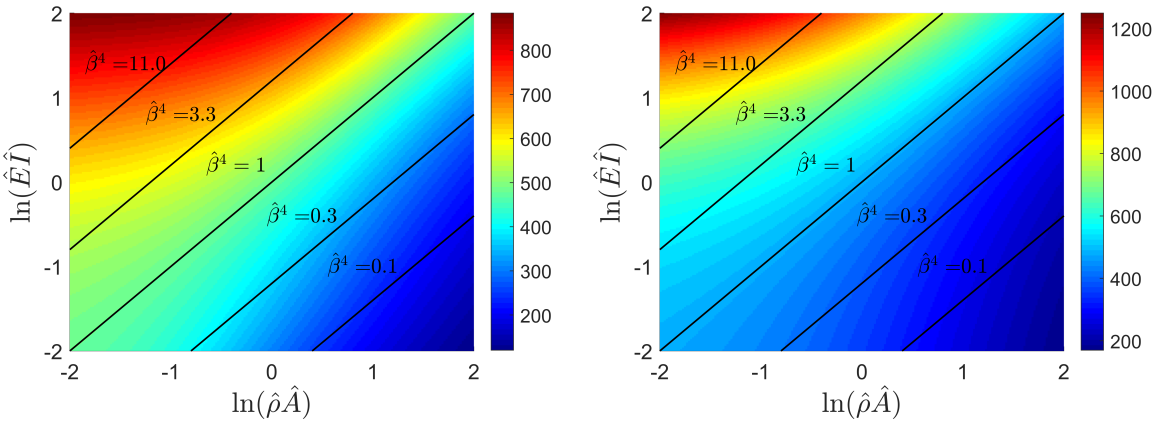

(a) Lower edge frequency

(b) Upper edge frequency

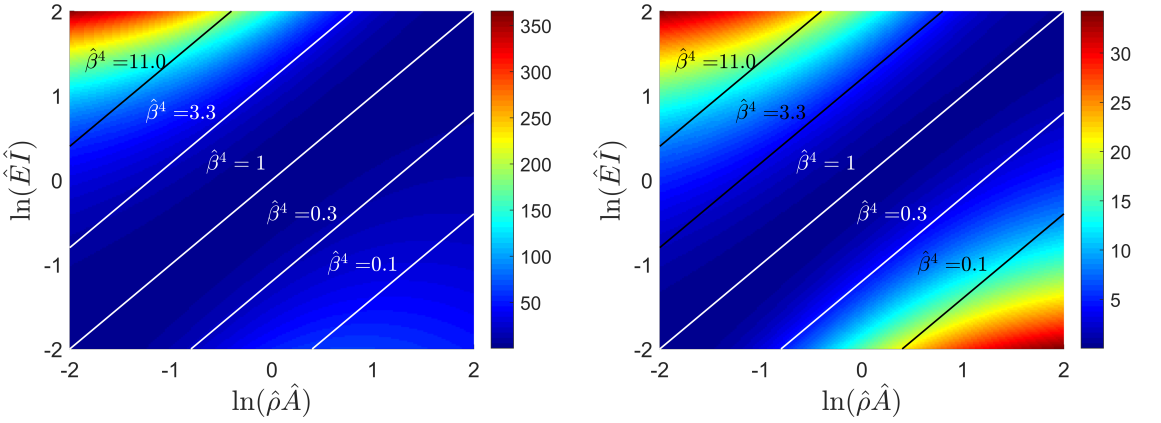

(c) Band gap width

(d) Normalized gap width(%)

Figure 2.2: Variations of the first band gap properties with changes in mass ratio ($\hat{\rho}\hat{A}$) and stiffness ratio ($\hat{E}\hat{I}$). $\hat{\beta}$ represents the ratio of the wave phase speed for the two beams. Lines of constant $\hat{\beta}$ give another measure for comparing the variations of the properties. (a)-(b) The band gap forms at lower frequencies as the mass ratio (stiffness ratio) increases (decreases). (c) The band gap width increases for high stiffness ratios along with low mass ratios. (d) The normalized gap width increases as we move to the two ends of the spectrum. (For the interpretation of the color references in this figure, the reader is referred to the web version of the article.)

We consider one of the beams to be a doubly-symmetric I-beam made of concrete with a Young's modulus of 25 GPa and a density of 2400 kg m^{-3}. The dimensions of the flange and web are 150×40 mm and 170×30 mm, respectively. The properties of the other beam are varied to explore the parameter space. The unit cell length, corresponding to the distance between the coupling points, is 1 meter.

Figures 2.2a and 2.2b show the variation of the lower and upper edge frequencies with the non-dimensional parameters $\hat{\rho}\hat{A}$ and $\hat{E}\hat{I}$. For a fixed mass ratio, as the stiffness ratio increases, the edge

frequencies increase. On the other hand, for a fixed value of stiffness ratio, the lower and upper edge frequencies decrease with an increase in mass ratio. Since for a homogeneous Euler-Bernoulli beam, the phase speed for a wave with radial frequency ω is equal to $\sqrt{\omega}\beta$, the variable $\hat{\beta}$ is, in fact, a measure of the wave's phase speed ratio in the two beams. Fig. 2.2 suggests that the band gap edge frequencies do not vary significantly in the region close to $\hat{\beta} = 1$, i.e. where the two beams have similar dispersive properties.

Fig. 2.2c shows the variation of the first band gap width with the non-dimensional parameters $\hat{\rho}\hat{A}$ and $\hat{E}\hat{I}$. When $\hat{\beta}$ is close to 1, the band gap width is very small. When $\hat{\beta}$ is exactly 1, there is no band gap - even if the two beams have different material and cross-sectional properties. However, as the contrast in the stiffness and mass ratios increases, the band gap width increases as well. In particular, for large stiffness ratios and low mass ratios, the band gap width becomes maximum. A local maximum is also observed in the region with high mass ratios and low stiffness ratios. It should be noted that as the bandwidth increases, so does the frequency corresponding to the lower edge of the band gap. In other words, the set of parameters that maximize bandwidth do not necessarily give the lowest frequency edge. Hence, depending on the target objective, the required mass and stiffness ratio may be tuned.

Fig. 2.2d shows a contour for the percent ratio between the gap width and the mid-gap frequency as a function of the two non-dimensional variables. At the two ends of the spectrum, the gap width-to-midgap frequency ratio is maximum. Thus, choosing high-contrast properties for the two beams leads to higher normalized band gap widths.

The above discussion suggests that achieving low-frequency band-gaps requires very high mass ratios and very low stiffness ratios; whereas, achieving wide band gaps requires low mass ratios and high stiffness ratios. The two, therefore, lie on the two ends of the spectrum. The high contrast required in β values may be accommodated by a high contrast in material properties of the two beams, a high contrast in cross-sectional properties or a combination of both. The resulting band gaps may be of BS or LR type. In the following section we review a classification of the expected band structure zones and follow with a representative numerical example.

Classification of the band structure zones For rigid connections, the dispersion relation for the coupled beam system is quadratic in $\cos qL$ as shown in section 2.2.1. Therefore, two pairs of wave numbers $\pm q_1$ and $\pm q_2$ are determined for a given frequency Ω. The wave numbers in each pair represent the same characteristic wave but travelling in opposite directions. Therefore, we only consider q_1 and

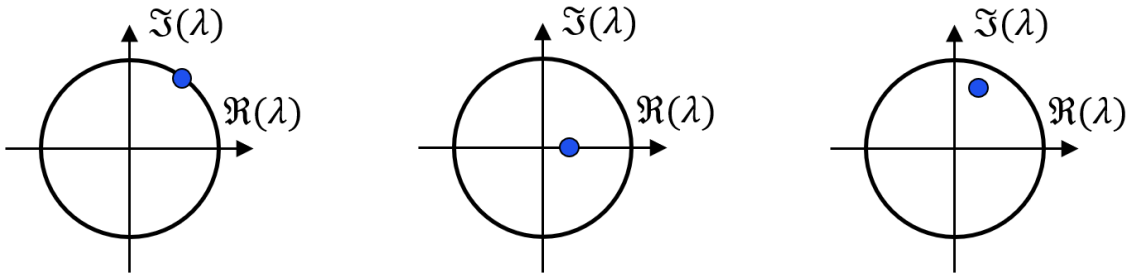

(a) (b) (c)

Figure 2.3: Classification of flexural waves: (a) propagating, (b) attenuating, (c) complex. $\lambda = e^{iqL}$.

q_2 herein to analyze the band gap structure. Physically, a flexural wave may be classified as follows based on its corresponding wave number (see Figure 2.3) [80, 79]:

a. Propagating: The wave number is purely real, $q = Re(q)$. In this case, the wave travels over the unit cells without attenuation and only with a phase change.

b. Attenuating: The real part of the wave number has the form $Re(q) = 0$ or $|Re(q)| = \pi$ and the imaginary part is nonzero. This corresponds to a wave that attenuates while travelling across a unit cell.

c. Complex: The wave number is complex, i.e. $0 < |Re(q)| < \pi$ and $|Im(q)| > 0$. In this case, the wave is propagating and attenuating as it travels along the structure.

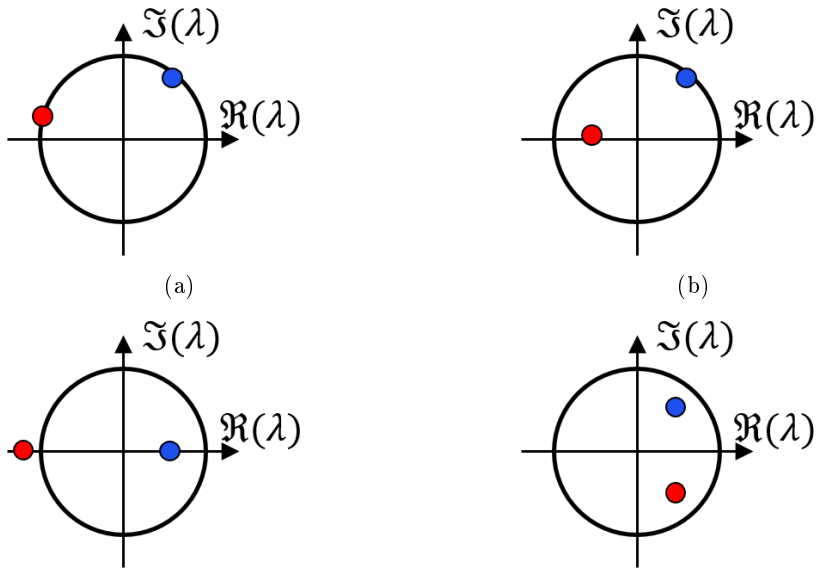

(a) (b) (c) (d)

Figure 2.4: Categorization of different regions in the band structure: (a) propagation-propagation, (b) propagation-attenuation, (c) attenuation-attenuation, and (d) complex. $\lambda_{1,2} = e^{iq_{1,2}L}$.

Depending on which category q_1 and q_2 belong to, the system will have four distinct types of dispersion properties at a given frequency Ω (see Figure 2.4):

I. Propagation-Propagation (PP): in this case both waves are propagating without attenuation across the system.

II. Propagation-Attenuation (PA): Only one of the waves propagates through the system and the other gets attenuated as it travels over multiple unit cells.

III. Attenuation-Attenuation (AA): where both wave numbers belong to the attenuation category. In this case, the adjacent cells vibrate either in phase or out of phase, attenuating the waves as they travel through the structure as a result. This behavior is typical of the classical Bragg Scattering phenomenon. Therefore, this region is also called the Bragg Scattering (BS) zone.

IV. Complex (C): The wave numbers q_1 and q_2 belong to category (c) above and are complex-conjugate. In this case, the two wave numbers essentially represent the same characteristic wave that attenuates and experiences a phase change as it travels across a unit cell. This is usually characteristic of a local resonance mechanism when using a periodic array of resonators. Thus, this region can also be marked as the Local Resonance (LR) zone.

Based on the classification proposed, there are two types of pass bands (PP and PA) and two types of band gaps (AA and C). In the example discussed in the next section, we determine the band structure and study the dispersive behavior of the system based on this classification.

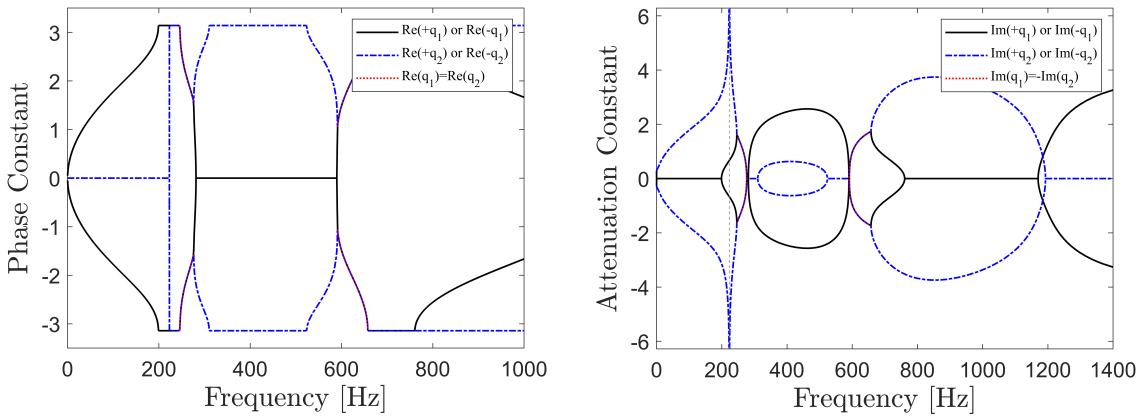

(a) (b)

Figure 2.5: The complex band structure of the periodic flexural system: (a) shows the real part of the wave number pair, which determines the dispersion relation of propagating waves and (b) shows the imaginary part of the wave number pair, governing the attenuation properties of the system.

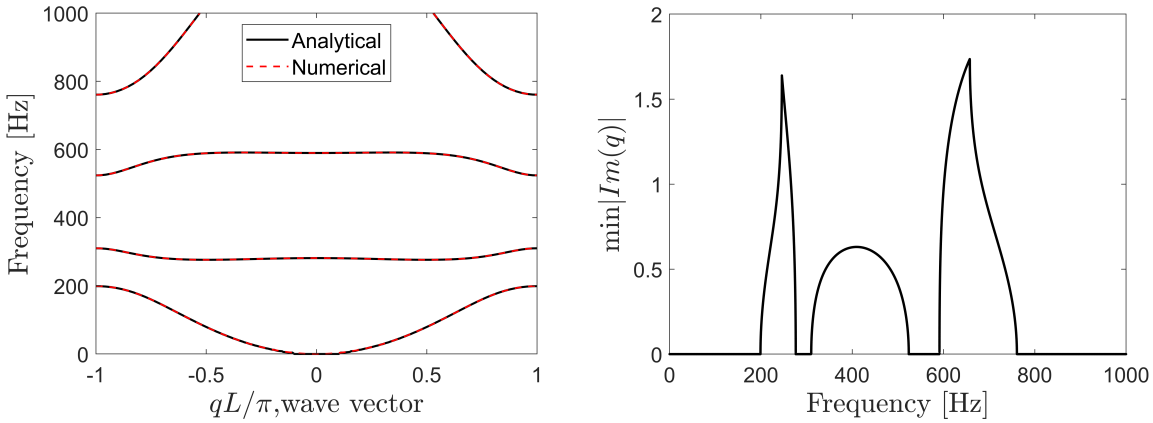

(a) (b)

Figure 2.6: A simplified representation of the complex band structure shown in Figure 2.5. (a) Dispersion curves of the periodically-coupled concrete and Tungsten beams. (b) Minimum absolute value of attenuation constants.

Example To achieve low-frequency band gaps, forming due to a high contrast in β ratios of the two beams, we consider coupling the concrete beam from the previous section to a beam made of a Tungsten alloy (Young's modulus 310 GPa and density 18000 $\mathrm{kg\,m^{-3}}$) with rigid connections. High-density tungsten alloys are widely used for vibration damping in different industries due to their favorable physical properties. This beam element is assumed to have a circular cross section with a radius of 30 millimeters. The length of the unit cell is considered to be 1 meter. The dispersion response of the system is studied in detail next.

The analytical solution given in section 2.2.1 is used to get a comprehensive view of the system's band gap structure (Fig. 2.5) and unravel the dispersion properties of the periodic system. The regions of interest to us are the AA and C regions, in which both waves get attenuated while traveling across the unit cells either by a BS or LR-type mechanism. The plots show that the first and third band gaps are generated by a blend of BS and LR-type mechanisms. In the first band gap, wave numbers transition from an AA region to a C zone as the frequency increases while for the third band gap, the transition between these zones is reversed. The second band gap, however, forms purely due to BS effects.

It should be noted that the dispersion relation of the waves that propagate freely in the system is governed by the purely real wave numbers while the attenuation properties of the system are dominated by the imaginary part of the wave number that has the lowest absolute value. Having this in mind, the complex band structure in Fig. 2.5 may be reduced to the simple representation in Fig. 2.6. Fig. 2.6a shows the dispersion curves of the periodic system and also serves to demonstrate that the analytical

and numerical results match.

Studying the band gap structure of the system shows that the first band gap spans from 199 Hz to 276 Hz with a normalized band gap width of 32.5%. The second band gap edge frequencies are 310 Hz and 524 Hz; this band gap has a normalized gap width of 51.2% . Interestingly, an almost flat dispersion curve lies between the first two band gaps. The ratio of the width of this pass band to the width of the frequency region between 199 Hz and 524 Hz is only 10.4%. Furthermore, waves with frequencies in this pass band region have significantly lower phase velocities than those corresponding to the first and third dispersion lines. These observations indicate that this pass band may be neglected in practice. Doing so, gives a wide band gap with a normalized width of nearly 90%.

Fig. 2.6b demonstrates the attenuation constants of the system within the band gaps. The figure shows that the first and third band gaps are Fano-shaped and highly asymmetric while the second band gap shows a smooth variation in the attenuation constant. These are well-established properties of the LR and BS band gaps, respectively and have been previously documented in the literature [82, 80, 83, 85].

Effect of connection compliance In this section, we study the effects of connection compliance on the band gap structure and attenuation properties of the system. The unit cell configuration in this case is shown in Fig. 2.1c. The analytical dispersion relation is determined in a similar manner as before and is found to be quartic in $\cos qL$ (see section 2.2.1). Therefore, four pairs of wave number solutions exist for a given frequency, with each pair representing the same characteristic wave but propagating in opposite directions. The nature of these characteristic waves (whether each is of Attenuating, Propagating or Complex type) determines the band structure of the system.

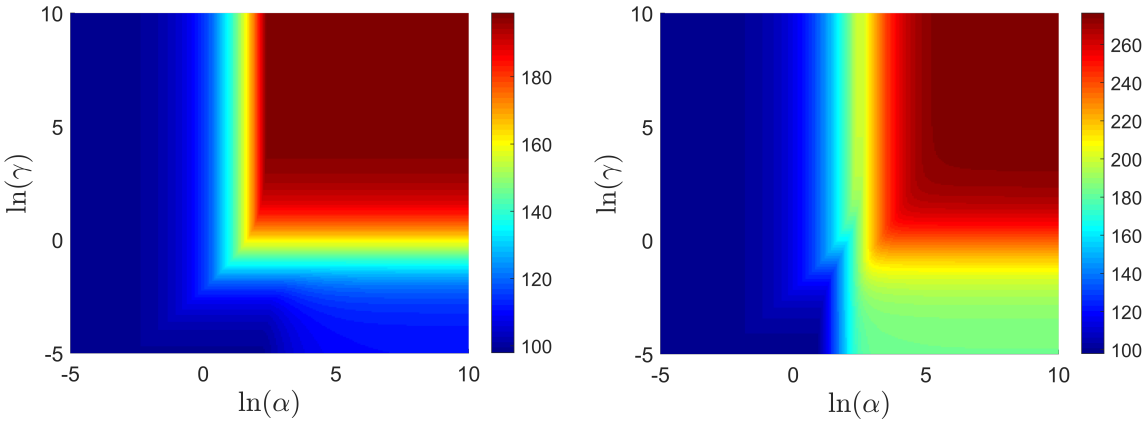

(a) Lower edge frequency

(b) Upper edge frequency

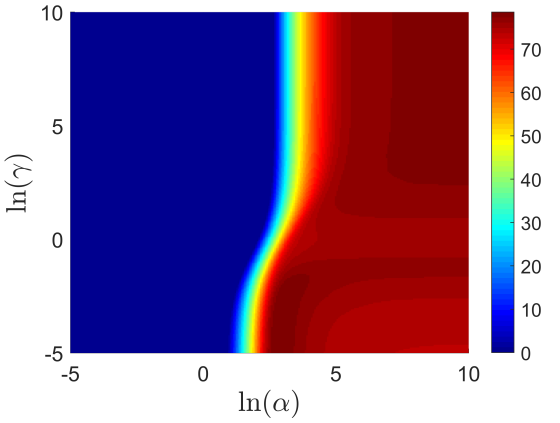

(c) Band gap width

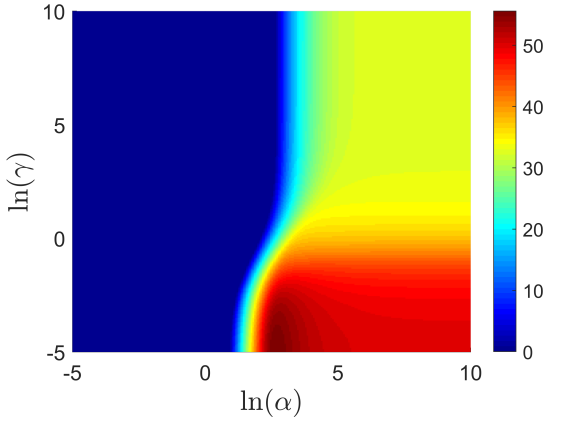

(d) Normalized gap width(%)

Figure 2.7: Variations of the first band gap properties with changes in the normalized stiffnesses of the translational and rotational springs (α and γ). (a)-(b) The edge frequencies increase as the stiffness of the connection increases. (c) The band gap width reaches its maximum in two regions: the stiff end of the spectrum (high α and γ values) and a limited region for very small γ values. (d) The maximum normalized gap width occurs in a localized region of α values for very low rotational stiffnesses. (For the interpretation of the color references in this figure, the reader is referred to the web version of the article.)

To facilitate further investigation, we introduce the non-dimensional parameters $\alpha = K_s/(E_1 I_1/a^3)$ and $\gamma = K_t/(E_1 I_1/a)$. Fig. 2.7 shows the variations in the first band gap properties as α and γ change. For low values of α, no band gaps exist even at high γ values. This suggests that the coupling between the translational displacements of the two beams is essential for generating band gaps. As α increases, the first band gap starts to form. The plots suggest that the band gap edge frequencies and width increase as the connection stiffness increases. Fig. 2.7c shows that the variation of the band gap width with the connection stiffness ratios is non-monotonic. Two local regions of maximized band gap width may be identified. The first region occurs for small values of γ ($\ln\gamma < -2$) and a

limited range of α values ($2.5 < \ln\alpha < 4.5$). The second region occurs towards the high-stiffness end of the spectrum, where both α and γ are large. Fig. 2.7d also suggests that the normalized band gap width varies non-monotonically with connection stiffness parameters. The normalized band gap width is maximized in a limited range of parameter values ($2.5 < \ln\alpha < 3.5$, $\ln\gamma < -3.5$).

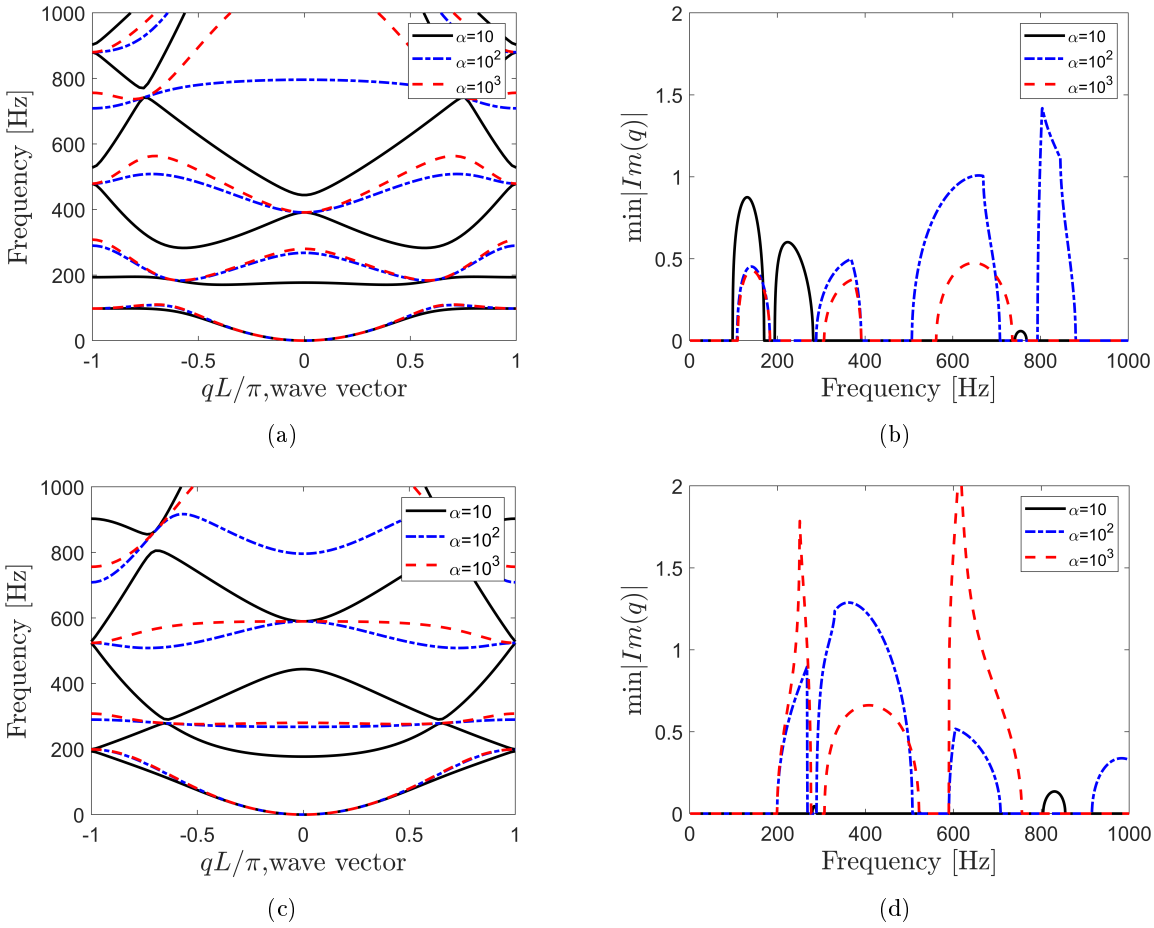

Figure 2.8: Effect of connection compliance on the band structure and attenuation strength of the system. (a)-(b): $\gamma = 0$. (c)-(d): $\gamma = 10^3$

.

The analytical solution discussed in section 2.2.1 is used next to study the effect of connection stiffness on the band gap structure and attenuation strength of the system. Two candidate cases are examined: In the first case, γ is set to 0 and in the second case, it is set to 10^3. In both cases, α values of 10,10^2 and 10^3 are considered. Fig. 2.8 shows how varying the two parameters modifies the dispersion properties of the system. For instance, in the first case, when $\alpha = 10$, there's a possibility of lowering the band gap edge frequency to 98.2 Hz and increasing the normalized gap width to 53.7% in comparison to the case with rigid connections (Fig. 2.6a). As another example, in the second case ($\gamma = 10^3$), when α is 100, the attenuation strength in the second band gap increases significantly. Whereas, when α is 10

in the same case, the band gap widths are very small, making this set of parameters unfavourable.

It should also be noted that when α and γ are both 10^3, the connection between the two beams may be considered as almost rigid. Thus, the overall band structure for this set of parameters is similar to the one for rigid connections (Fig. 2.6). Figures 2.8b and 2.8d show the effect of connection compliance on the attenuation properties of the periodic structure. The plots indicate that tuning the stiffness of the connection may increase the attenuation strength, change the nature of the attenuation mechanisms and make them interact.

Here, we will include the complex band structure of the system with compliant connections for two sample cases in order to highlight the complexity of solution behaviors and the strong interactions between characteristic waves: one corresponds to $\alpha = 100$ and $\gamma = 0$ while the other corresponds to $\alpha = 1000$ and $\gamma = 0$. Figures 2.9a and 2.9b show that within the second band gap, all wave number solutions are of Attenuating type; however, the solution behavior changes within the third band gap. This band gap starts with two Complex and two Attenuating wave number pairs but all solutions become Attenuating as the frequency increases. Figures 2.9c and 2.9d suggest that within the second band gap, all wave numbers are Attenuating while the third one forms with a complex-conjugate pair and two attenuating ones. The solution behavior doesn't change within the band gap in this case. The plots highlight the complexity of the band structure and the strong interactions between the characteristic waves when the connections are not rigid. The observations encourage further future investigation to characterize the propagation/attenuation zones corresponding to different solution behaviors.

Hierarchical systems In this section, we briefly study the effect of coupling more than two beams having different periodicities at different scales on the dispersion properties of the overall structure.

Fig. 2.10 shows the unit cell configurations and the corresponding dispersion curves for three cases: (i) a concrete and tungsten beam coupled periodically with a unit cell length of 1 meter; (ii) a concrete and tungsten beam coupled periodically with a unit cell length of 0.5 m; and (iii) a concrete and tungsten beam periodically coupled at 0.5 m spacing with the whole pair coupled to a third tungsten beam at 1 m spacing. The third configuration is a combination of the first two and involves two periodicity scales. The figure shows that the interaction between the two periodicity scales in case (iii) has modified the system's band structure, creating band gaps where we previously had propagation zones and affecting the edge frequencies. The effect of hierarchy is more pronounced when comparing cases (ii) and (iii):

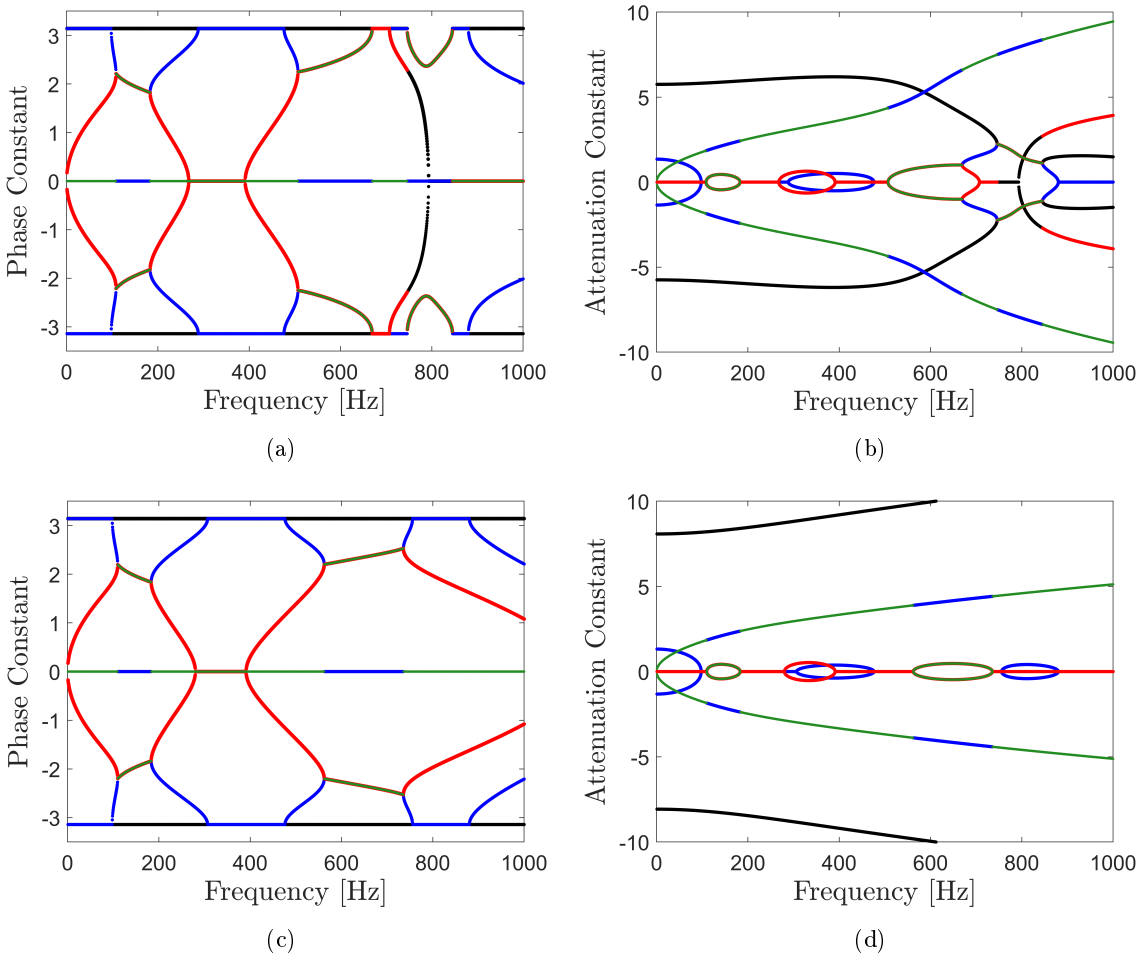

Figure 2.9: The complex band structure of the periodic flexural system with compliant connections for $\gamma = 0$, $\alpha = 100$ (above) and $\alpha = 1000$ (below). The different colors show the four characteristic wave solutions. (a) and (c) show the real part of the wave numbers, which determines the dispersion relation of propagating waves. (b) and (d) show the imaginary part of the wave numbers, governing the attenuation properties of the system. (Colored version of this figure is available online).

the edge frequencies of the first band gap are considerably lower in case (iii) and several band gaps form where we had propagation zones in case (ii). The dispersion curves in case (iii) are close to the ones in case (i) for low frequencies but start to deviate from them at higher frequency ranges. For example the fourth band gap in case (iii) forms in a propagation zone of case (i). These findings suggest that this may potentially be an effective intervention technique for changing attenuation properties of existing metamaterial beam structures.

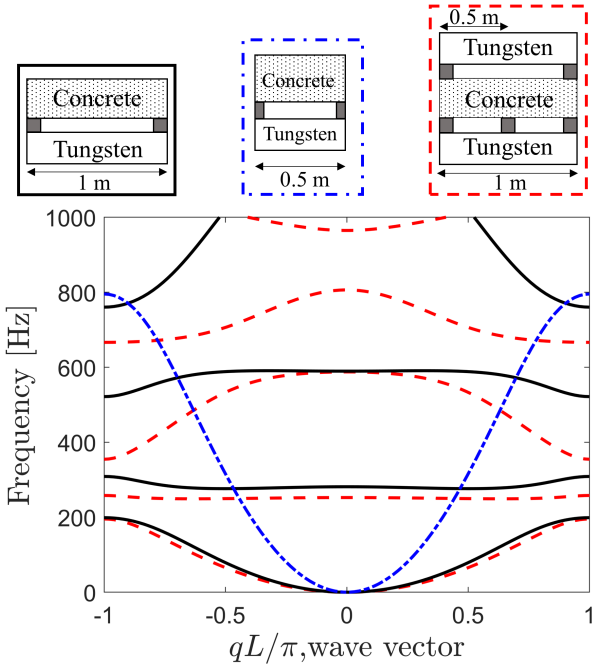

Figure 2.10: The dispersion plots corresponding to the three unit cell configurations in the insert: cases (i)-(iii) as described in the text plotted with solid black line, blue dashed-dotted line and red dashed line, respectively.

2.3.2 Finite systems

In order to study the vibration transmittance properties of the system, we calculate the Frequency Response Function (FRF) of two periodically-connected, simply-supported beams with 20 unit cells. The material and cross-sectional properties of the beams as well as the unit cell length are the same as the example discussed in the previous section. Two cases are considered: one with rigid connections and one with connection stiffness parameters $\alpha = 100$ and $\gamma = 0$. Each beam is divided into 200 finite beam elements. The FRF matrix $[H_{qF}]$ due to a harmonic excitation force of amplitude F_0 can be determined from the FEM model using modal analysis:

$$\begin{aligned} &[M_r]\{\ddot{\eta}_r\} + [C_r]\{\dot{\eta}_r\} + [K_r]\{\eta_r\} = \{F_r\} \\ &[H_{\eta_r f_r}] = [-\Omega^2[M_r] + [K_r] + i\Omega[C_r]]^{-1} \\ &[H_{qF}] = [\Phi][H_{\eta_r f_r}][\Phi^T] \end{aligned} \tag{2.15}$$

where, $[M_r]$, $[K_r]$ and $[C_r]$ are the modal mass, stiffness and damping matrices respectively. The modal damping coefficient ξ is assumed to be equal for all modes. $\{\eta_r\}$ is the vector of modal coordinates and $F_r = \Phi^T F$ ($F = \{0, 0, F_0 e^{i\Omega t}, 0, ...\}^T$) is the modal forcing vector with $[\Phi]$ being the matrix of eigenvectors.

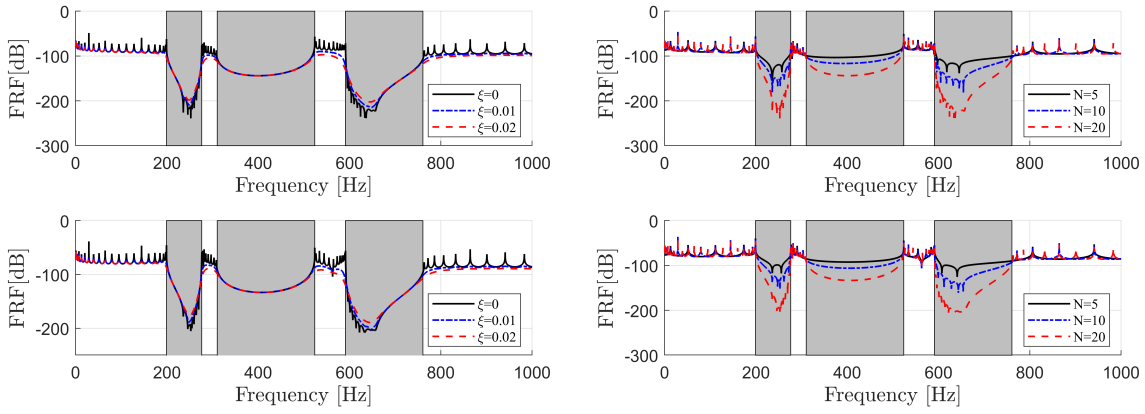

(a) (b)

Figure 2.11: Steady-state response of the periodic system: (a) Frequency Response Function of the concrete beam (above) and Tungsten beam (below) for a structure with 20 unit cells and different damping coefficients. (b) Comparison of the undamped Frequency Response Functions of the concrete beam (above) and Tungsten beam (below) for structures with different number of unit cells.

In all cases, the harmonic excitation is applied at the node adjacent to the left support on the concrete beam and the transverse response is measured at the node adjacent to the right support for each beam. In addition, the node where the harmonic force is applied is not a connection point between the two members. Figures 2.11a and 2.12a show the FRF of the transverse displacement for different levels of damping. The grey areas show the band gap regions predicted in the previous section. The figures show that the regions of strong attenuation lie well within the band gaps. The relative strength of attenuation in each region is consistent with the attenuation constants shown in Figures 2.6b and 2.8b for the case of rigid and compliant connections, respectively. For example, in the case of the rigid connection, the wave attenuation is intensified in the first and third band gaps, where BS and LR effects blend in and the attenuation constants are larger compared to the second band gap with a BS-type mechanism and smaller attenuation constants. The figure also shows that the FRF peaks corresponding to the resonance frequencies of the structure may be smoothened by a slight increase in the damping coefficient.

Figures 2.11b and 2.12b show the Frequency Response Function for different number of unit cells. The figures indicate that as the number of unit cells increases, the reduction in amplitude becomes larger, as is expected in periodic systems.

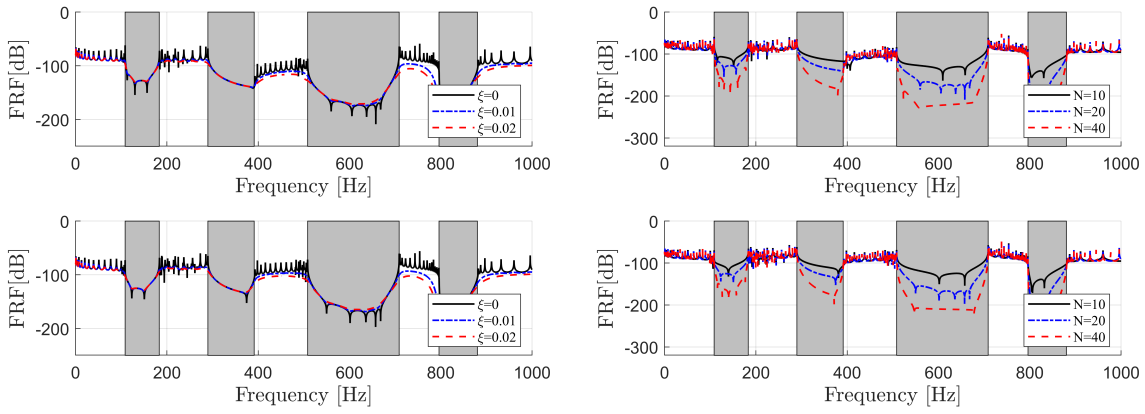

(a) (b)

Figure 2.12: Steady-state response of the periodic system with compliant connections ($\gamma = 0$, $\alpha = 100$): (a) Frequency Response Function of the concrete beam (above) and Tungsten beam (below) for a structure with 20 unit cells and different damping coefficients. (b) Comparison of the undamped Frequency Response Functions of the concrete beam (above) and Tungsten beam (below) for structures with different number of unit cells.

2.4 Discussion

We have presented a mathematical model and analytical representation of the dispersion relation for coupled Euler-Bernoulli beams that are periodically joined by rigid or compliant connections. While each homogeneous beam does not individually have band gaps, multiple band gaps emerge when the two beams are connected in parallel. Our results suggest that a high contrast between the phase speeds in the pair of flexural members affects the band structure of the system and its dispersion properties significantly. In particular, we have shown that for high mass ratios and low stiffness ratios, the edge frequencies may be pushed towards low-frequency ranges but only at the cost of band gap width reduction. For low mass and high stiffness ratios, band gaps have remarkably larger widths but form at higher frequencies. Interestingly enough, $\hat{\beta} = 1$, corresponding to the case of two beams having the same phase speed, is the line of symmetry for the normalized gap width. The contour shows an increase in the normalized gap width when moving away from this line.

By analyzing the regions of propagation and attenuation in the band gap structure, we have shown that, just as in the case of discrete periodic resonators, depending on the nature of the wave numbers, two different mechanisms are responsible for band gap formation: Bragg Scattering (BS) and Local Resonance (LR). Constructing a simplified representation of the complex band structure, showed that the attenuation constant varies smoothly in the band gap regions associated with the BS effect while it possesses sharp peaks and is highly asymmetric where LR is the main attenuation mechanism.

Thus, unlike the conventional binary configuration, in which heterogeneous flexural components are connected in series, leading to the formation of BS-type band gaps, the proposed parallel configuration benefits from both BS and LR attenuation mechanisms.

Investigation of the effect of connection compliance shows that the transverse coupling is necessary for band gap formation. Whereas, the elimination of the rotational spring lowers the first band gap edge while increasing its width for a limited range of transverse spring stiffness values. We also showed that tuning the stiffness of the springs may affect the nature of the band gap formation mechanisms as well as the strength of attenuation. Thus, the compliance of the connection may be used as a means of controlling and/or modifying the band structure of the system.

As a preliminary step towards the hierarchical design of metamaterial beam systems, we have demonstrated how adding periodicity in another length scale may affect the dispersion properties of the original structure. The new system has attenuation zones that do not exist in either of the two structures alone. Stacking flexural elements with different unit cell sizes, thus, seems a promising avenue for benefiting from the interaction between the scales and enriching or altering the dispersion properties of a system.

Although a lot of research has been done on periodic and local resonant metamaterials, many have mainly focused on using discrete resonators [86, 87, 77, 88] or modelling the effect of continuous resonators, such as beams, with spring-mass assemblies [78]. Considering that these discrete resonators affect the dispersion properties of the main system by creating band gaps in regions close to their natural frequency, the use of continuous elements with a countable infinity set of natural frequencies seems to offer more possibilities for enriching the system's band structure. Our study, in particular, shows that by periodically connecting two Euler-Bernoulli beams, a new system with several LR and BS band gaps is created and that varying the coupling strength, by changing the connection's compliance, will let the two mechanisms interact.

As pointed out briefly in Section 1, unconventional designs have been recently proposed that offer a broader range of dispersion characteristics [40]. Among these novel configurations are the concepts of resonator-to-resonator interactions [41, 42] and nonlocal resonances [43]. For example, in Beli et al. 2018 [42], the interaction between the transverse and rotational modes of a resonator chain consisting of beam elements has been used to achieve a wider band gap in comparison to the case where the resonators perform independently. The authors show how certain Bloch wave modes of the system correspond to the resonance frequencies of the resonator chain. DePauw et al. 2018 [43] propose

a configuration called a Phononic Resonator in which each resonator can directly interact with the neighboring masses in the main chain. It is then shown how tuning the stiffness and mass ratios of the main and resonator masses can change the nature of the attenuation mechanism leading to the system behaving as a Phononic Crystal or an Acoustic Metamaterial. In the present work, there can be no distinction between the host and resonating elements since the members periodically connected are both continuous. Therefore, we conjecture that, unlike the previous studies, the resonance frequencies at which the attenuation peaks occur do not solely depend on the properties of one element or the other. Furthermore, Apart from the fact that tuning the physical parameters of the problem could change the nature of the attenuation mechanism within band gaps (such as that observed in DePauw et al. 2018), a mixture of BS and LR effects is observed within certain band gaps. Similar phenomenon has been reported in [81, 79, 83].

Future extensions of this work may include further investigation of the hierarchical coupling, which significantly increases the dimension of the parameter space. Given the surge of interest in non-reciprocal wave propagation, it may be of interest to explore the influence of space-time modulation of the coupled beams' elastic properties or the time modulation of the connection compliance on the overall dispersion relation structure and directional control of the energy flow. Furthermore, combination of coupled beams and discrete resonators may be considered as this setup may enable further tuning of the band gap structure as well as the formation of band gaps in lower frequencies. Another intriguing route for future investigations is controlling the transitions between different propagation/attenuation zones in the band structure by tuning the design parameters. The coefficients of the dispersion relation, presented in Appendix **??**, may be used to describe the different propagation characteristics of the system with rigid connections on the invariant's plane $J_1 - J_2$ [89]. A mapping from the invariant plane to the physical parameter plane could then be used to visualize the transition between propagation domains as the parameters are varied. A similar study could be carried out for general systems with dispersion relations that are of fourth order in $\cos qL$.

2.5 Conclusions

In this work, We investigated the dynamics and dispersion properties of flexural elements that are periodically coupled in parallel using rigid or compliant connections. our main conclusions are summarized as follows:

- For rigid connections between the two elements, a high contrast between the phase speeds affects

the band structure of the system significantly. In particular, for the first band gap, high (low) mass ratios and low (high) stiffness ratios result in lower (higher) edge frequencies and narrower (wider) band gaps.

- Unlike the conventional configuration, in which beam elements of different material/geometric properties are connected in series, leading to BS-type band gaps, the proposed configuration benefits from both BS and LR mechanisms.

- The connection compliance may be used to modify the system's band structure by opening/closing gaps. Tuning the stiffness parameters may lower some band gap edge frequencies, increase their width, intensify the attenuation strength or change the nature of the attenuation mechanisms.

- Stacking flexural elements at different periodicity lengths may modify the band structure by closing/opening band gaps.

Chapter 3

Dispersion properties and dynamics of ladder-like meta-chains

The content of this chapter has been published in Extreme Mechanics Letters [90]

3.1 Introduction

Periodic structures have been widely used to control the propagation of acoustic and elastic waves [1]. Engineering the architecture of these systems alters their dispersion properties and leads to the formation of band gaps. Periodic structures may be classified in two groups: Phononic Crystals (PCs) and Metamaterials. While phononic structures mainly owe their characteristics to Bragg scattering (BS) and interference effects, metamaterials draw their strength from local resonances (LR). Several realizations of each class have been suggested as possible waveguides, filters and other devices aimed at controlling the propagation of waves [91, 92, 93, 94, 53, 19, 20]. More recently, unconventional designs have been proposed to combine features of the two categories [40, 41, 43] or explain how PCs may show metamaterial attributes under special circumstances [95, 96].

Recent work on periodic entanglement of elements placed in parallel has shown that this class of systems possesses interesting dynamic properties [97, 14, 93, 42, 69]. For example, Chen and Elbanna studied wave propagation in bars that are periodically coupled along their length. The results showed that for certain set of parameters, the system possesses extreme attenuation zones and may be used as a mechanical switch [93]. Beli et al. used the interaction between the transverse and rotational modes of a resonator chain consisting of beam elements to widen the band gap of the original system, in which resonators were not interconnected [42]. A similar configuration to [47] for flexural beam elements was studied by the authors of the present work. Results of the study revealed that several BS and LR band gaps form and static tuning of the connection stiffness can change the nature of attenuation mechanisms [69].

One-dimensional spring-mass systems serve as simplified models for studying various physical phe-

nomenon at different scales [98, 60, 58, 99, 100]. They are also frequently used in the design of wave-control devices [101, 53, 102, 103, 104, 105, 60]. In the context of periodic systems, several works have investigated the wave propagation properties of one-dimensional phononic and resonant spring-mass lattices [106]. In this work, we set out to determine the dispersion characteristics of ladder-like meta-chains, consisting of monoatomic chains that are connected in parallel. We will investigate two configurations. One is a configuration where each mass in one chain is connected to its corresponding mass in the other chain (full coupling). The other, consists of chains that are periodically coupled only at certain locations (partial coupling). Properties of the fully-coupled configuration in the long wavelength limit have been recently shown to allow for the propagation of elastic waves with nonconventional topology [48, 49, 50].

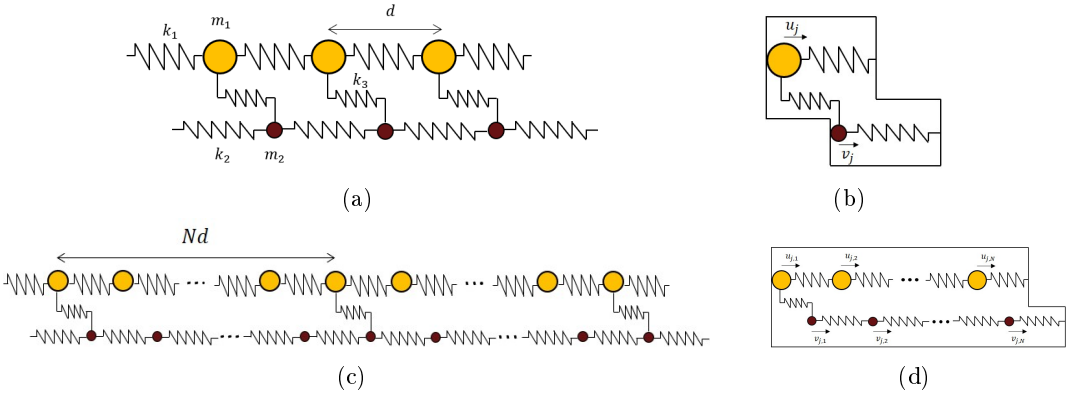

Figure 3.1: Configuration of the meta-chain and j^{th} unit cell for the fully-coupled (a)-(b) and partially-coupled (c)-(d) systems.

This chapter is organized as follows: in section 3.2, we develop the mathematical expressions for the dispersion relations of both coupling configurations. Section 3.3 highlights the prominent dispersion characteristics of the proposed configurations using illustrative examples and the analytical expressions derived. In section 3.4, we propose two simple filtering devices that leverage the dispersion characteristics of coupled chains and demonstrate numerically their performance under impact and harmonic loading.

3.2 Mathematical formulation of the band structure

Fully-Coupled Chains In this configuration, two classical monoatomic chains with different mass and spring stiffnesses are fully connected along their length (Fig. 3.1a). The interatomic distance in both chains is defined as d. Each unit cell consists of two masses m_1 and m_2 that interact through

a spring of stiffness k_3 (Fig. 3.1b). Within each chain, masses are connected through springs of stiffness k_1 and k_2. Representative frequencies of the two chains are introduced as $\omega_1 = \sqrt{k_1/m_1}$ and $\omega_2 = \sqrt{k_2/m_2}$. The equations of motion for the j^{th} unit cell may be written as follows:

$$m_1\ddot{u}_j + k_1(2u_j - u_{j-1} - u_{j+1}) + k_3(u_j - v_j) = 0 \tag{3.1a}$$

$$m_2\ddot{v}_j + k_2(2v_j - v_{j-1} - v_{j+1}) + k_3(v_j - u_j) = 0 \tag{3.1b}$$

where, u and v represent the displacements of m_1 and m_2. Solutions in the form of harmonic plane waves are sought.

$$u_j(t) = \hat{u}\left(k(\omega)\right) e^{i(kjd-\omega t)} \tag{3.2a}$$

$$v_j(t) = \hat{v}\left(k(\omega)\right) e^{i(kjd-\omega t)} \tag{3.2b}$$

Here, ω is the temporal frequency of the harmonic motion and k is the wave number. Eq. (3.2) is also a representation of the Floquet-Bloch theorem, which governs the propagation of plane waves in periodic structures. We introduce the following non-dimensional parameters:

$$\alpha = \frac{m_2}{m_1} \quad , \quad \beta = \frac{k_2}{k_1} \quad , \quad \gamma = \frac{k_3}{k_1} \tag{3.3}$$

Hereafter, the chain whose properties are used for normalization is referred to as the "reference chain". Substituting Eq. (3.2) in Eq. (3.1) and rewriting the results using the non-dimensional parameters introduced above, gives the following dispersion relation in terms of the non-dimensional wave number $\mu = kd$ and frequency $\Omega = \omega/\omega_1$:

$$\hat{u}\left(2 + \gamma - \Omega^2 - \left(e^{-ika} + e^{ika}\right)\right) - \gamma\hat{v} = 0 \tag{3.4a}$$

$$-\gamma\hat{u} + \left(2\beta + \gamma - \alpha\Omega^2 - \beta\left(e^{-ika} + e^{ika}\right)\right) = 0 \tag{3.4b}$$

In matrix form, the equations may be written as

$$\begin{bmatrix} 2(1-\cos ka) + \gamma - \Omega^2 & -\gamma \\ -\gamma & 2\beta(1-\cos ka) + \gamma - \alpha\Omega^2 \end{bmatrix} \begin{Bmatrix} \hat{u} \\ \hat{v} \end{Bmatrix} = 0 \tag{3.5}$$

For nontrivial solutions, we set the determinant of the coefficient matrix to zero. This gives the dispersion relation in the following quadratic form:

$$\cos^2\mu + \frac{I_1}{2}\cos\mu + \frac{I_2 - 2}{4} = 0 \tag{3.6}$$

I_1 and I_2 are the invariant coefficients of the dispersion relation [89] and may be written as follows

$$I_1 = \frac{1}{\beta}\left[(\alpha+\beta)\Omega^2 - (4\beta+\gamma+\beta\gamma)\right] \tag{3.7a}$$

$$I_2 = 2 + \frac{1}{\beta}\left[\alpha\Omega^4 - (2\alpha+2\beta+\gamma+\alpha\gamma)\Omega^2 + (4\beta+2\gamma+2\beta\gamma)\right] \tag{3.7b}$$

Provided that $\beta \neq 0$, the solution may be written as

$$(\cos\mu)_{1,2} = \frac{1}{4}\left(-I_1 \pm \sqrt{8 + I_1^2 - 4I_2}\right) \tag{3.8}$$

An alternative approach to deriving the dispersion relation based on the dispersion relation of each constituent is presented in Appendix A.

It is worth to note that for $\beta = 0$, the dispersion relation reduces to the one for a 1-D monoatomic lattice with internal resonators and when α goes to infinity, the dispersion relation of a grounded monoatomic chain is recovered. In the limit of large γ values, the system behaves as one chain with a mass and stiffness equal to the sum of the two original chains; whereas, the limit of small γ values represents the collapse of the system into two separate chains.

Partially-Coupled Chains In this configuration, the two chains are coupled every $N > 1$ masses (Fig. 3.1c). This configuration could also be thought of as connecting the supercells of two monoatomic chains. Therefore, a single unit cell consists of $2N$ masses in total (Fig. 3.1d). We determine the dispersion relation for an arbitrary N here by considering two cases: one is where the two chains are coupled every other mass ($N = 2$) and the other is for the general case of $N > 2$.

For $N > 2$, the equations of motion for unit cell j are written as follows. For the left-most masses in the unit cell:

$$m_1\ddot{u}_{j,1} + k_1(2u_{j,1} - u_{j-1,N} - u_{j,2}) + k_3(u_{j,1} - v_{j,1}) = 0 \tag{3.9a}$$

$$m_2\ddot{v}_{j,1} + k_2(2v_{j,1} - v_{j-1,N} - v_{j,2}) + k_3(v_{j,1} - u_{j,1}) = 0 \tag{3.9b}$$

Here, the first subscript for u and v denotes the unit cell number while the second denotes the mass

number within each chain. For the interior masses in the unit cell:

$$m_1\ddot{u}_{j,n} + k_1(2u_{j,n} - u_{j,n-1} - u_{j,n+1}) = 0 \tag{3.10a}$$

$$m_2\ddot{v}_{j,n} + k_2(2v_{j,n} - v_{j,n-1} - v_{j,n+1}) = 0 \tag{3.10b}$$

with n ranging from 2 to $N-1$. For the rightmost masses in the unit cell:

$$m_1\ddot{u}_{j,N} + k_1(2u_{j,N} - u_{j,N-1} - u_{j+1,1}) = 0 \tag{3.11a}$$

$$m_2\ddot{v}_{j,N} + k_2(2v_{j,N} - v_{j,N-1} - v_{j+1,1}) = 0 \tag{3.11b}$$

We note that for the case of $N = 2$, no interior masses exist so only equations (3.9) and (3.11) are required. For both cases, we assume harmonic plane-wave solutions with the following form

$$u_{j,n}(t) = U_n e^{iks(j,n)d} e^{-i\omega t} \tag{3.12a}$$

$$v_{j,n}(t) = V_n e^{iks(j,n)d} e^{-i\omega t} \tag{3.12b}$$

where, $s(j,n) = (j-1)N + n$ is a function that determines the position of each mass in the chain. Substituting Eq. (3.12) in the equations of motion for each case gives the corresponding dispersion relation.

$$\cos^2\mu + \frac{J_1}{2}\cos\mu + \frac{J_2 - 2}{4} = 0 \tag{3.13}$$

Here, $\mu = kNd$ is the non-dimensional wave number. The invariant coefficients J_1 and J_2 may be expressed in closed form for two cases:

Case 1: N=2 In this case, we may write the closed form of J_1 and J_2 as:

$$\begin{aligned} J_1 = \frac{1}{\beta^2}\big(&-(\alpha^2+\beta^2)\Omega^4 \\ &+(4\alpha\beta+\alpha\gamma+\beta^2\gamma+4\beta^2)\Omega^2 \\ &-(2\beta\gamma+2\beta^2\gamma+4\beta^2)\big) \end{aligned} \tag{3.14}$$

$$\begin{aligned} J_2 = \frac{1}{\beta^2}\big(&\alpha^2\Omega^8-(4\alpha\beta+\alpha\gamma+\alpha^2\gamma+4\alpha^2)\Omega^6 \\ &+(16\alpha\beta+4\alpha\gamma+2\beta\gamma+2\alpha^2\gamma+2\alpha^2+2\beta^2+4\alpha\beta\gamma)\Omega^4 \\ &-(8\alpha\beta+2\alpha\gamma+8\beta\gamma+2\beta^2\gamma+8\beta^2+8\alpha\beta\gamma)\Omega^2 \\ &+4\beta\gamma+4\beta^2\gamma+6\beta^2\big) \end{aligned} \tag{3.15}$$

Case 2: N>2 Upon substituting the plane-wave solutions, we may write the equations of motion of the unit cell in terms of the non-dimensional parameters introduced. For the leftmost masses in the unit cell:

$$(2+\gamma-\Omega^2)U_1 - U_2 - e^{-i\mu}U_N - \gamma V_1 = 0, \tag{3.16a}$$

$$(2\beta+\gamma-\alpha\Omega^2)V_1 - \beta V_2 - \beta e^{-i\mu}V_N - \gamma U_1 = 0 \tag{3.16b}$$

For the interior masses:

$$(2-\Omega^2)U_n - (U_{n-1}+U_{n+1}) = 0 \tag{3.17a}$$

$$(2\beta-\alpha\Omega^2)V_n - \beta(V_{n-1}+V_{n+1}) = 0 \tag{3.17b}$$

For the rightmost masses:

$$(2-\Omega^2)U_N - U_{N-1} - e^{i\mu}U_1 = 0 \tag{3.18a}$$

$$(2\beta-\alpha\Omega^2)V_N - \beta V_{N-1} - \beta e^{i\mu}V_1 = 0 \tag{3.18b}$$

Here, $\mu = kNd$. We look for a general dispersion relation formula for a unit cell with a total of $2N$ masses. Seeking non-trivial solutions require that the determinant of the coefficient matrix be zero.

This matrix may be partitioned as follows:

$$A = \left[\begin{array}{c|c} A_{LL} & A_{LI} \\ \hline A_{IL} & A_{II} \end{array}\right] \tag{3.19}$$

In this partitioning, A_{LL} corresponds to the degrees of freedom (DOFs) on the left boundary and does not change as N increases. A_{II} corresponds to the interior DOFs. $A_{IL} = A_{LI}^*$, where the superscript * indicates complex-conjugate.

$$A_{LL} = \begin{bmatrix} 2+\gamma-\Omega^2 & -\gamma \\ -\gamma & 2\beta+\gamma-\alpha\Omega^2 \end{bmatrix}_{2\times 2} \tag{3.20a}$$

$$A_{LI} = \begin{bmatrix} -1 & 0 & ... & 0 & -e^{-i\mu} & 0 & 0 & ... & 0 & 0 \\ 0 & 0 & ... & 0 & 0 & -\beta & 0 & ... & 0 & -\beta e^{-i\mu} \end{bmatrix}_{2\times(2N-2)} \tag{3.20b}$$

$$A_{II} = \left[\begin{array}{c|c} A_{II}^{(1)} & 0 \\ \hline 0 & A_{II}^{(2)} \end{array}\right]_{(2N-2)\times(2N-2)} \tag{3.20c}$$

where,

$$A_{II}^{(1)} = \begin{bmatrix} 2-\Omega^2 & -1 & & 0 \\ -1 & \ddots & \ddots & \\ & \ddots & \ddots & -1 \\ 0 & & -1 & 2-\Omega^2 \end{bmatrix} \quad A_{II}^{(2)} = \begin{bmatrix} 2\beta-\alpha\Omega^2 & -\beta & & 0 \\ -\beta & \ddots & \ddots & \\ & \ddots & \ddots & -\beta \\ 0 & & -\beta & 2\beta-\alpha\Omega^2 \end{bmatrix} \tag{3.21}$$

Using Schur's identity, $|A| = 0$ may be written as $|A_{LL} - A_{LI}A_{II}^{-1}A_{IL}||A_{II}| = 0$ provided that A_{II} is invertible, $|A_{II}| \neq 0$. Thus, $|A_{LL} - A_{LI}A_{II}^{-1}A_{IL}|$ has to be zero.

$$A_{II}^{-1} = \left[\begin{array}{c|c} {A_{II}^{(1)}}^{-1} & 0 \\ \hline 0 & {A_{II}^{(2)}}^{-1} \end{array}\right] \tag{3.22}$$

$$T = A_{LI}A_{II}^{-1}A_{IL} = \begin{bmatrix} T_{11} & 0 \\ 0 & T_{22} \end{bmatrix}_{2\times 2} \tag{3.23}$$

We may write the elements of this matrix as follows:

$$T_{11} = [A_{II}^{(1)^{-1}}]_{1,1} + [A_{II}^{(1)^{-1}}]_{N-1,N-1} + [A_{II}^{(1)^{-1}}]_{N-1,1}e^{-i\mu} + [A_{II}^{(1)^{-1}}]_{1,N-1}e^{i\mu} \tag{3.24a}$$

$$T_{22} = \beta^2 \left([A_{II}^{(2)^{-1}}]_{1,1} + [A_{II}^{(2)^{-1}}]_{N-1,N-1} + [A_{II}^{(2)^{-1}}]_{N-1,1}e^{-i\mu} + [A_{II}^{(2)^{-1}}]_{1,N-1}e^{i\mu} \right) \tag{3.24b}$$

Since $A_{II}^{(1)}$ and $A_{II}^{(2)}$ are both Toeplitz tridiagonal matrices,

$$[A_{II}^{(p)^{-1}}]_{1,1} = [A_{II}^{(p)^{-1}}]_{N-1,N-1} \tag{3.25a}$$

$$[A_{II}^{(p)^{-1}}]_{1,N-1} = [A_{II}^{(p)^{-1}}]_{N-1,1} \tag{3.25b}$$

where $p = 1, 2$.

We use these equalities to simplify the elements of T:

$$T_{11} = 2[A_{II}^{(1)^{-1}}]_{1,1} + [A_{II}^{(1)^{-1}}]_{N-1,1} \left(e^{-i\mu} + e^{i\mu} \right) \tag{3.26a}$$

$$T_{22} = \beta^2 \left(2[A_{II}^{(2)^{-1}}]_{1,1} + [A_{II}^{(2)^{-1}}]_{N-1,1} \left(e^{-i\mu} + e^{i\mu} \right) \right) \tag{3.26b}$$

Therefore, determining $[A_{II}^{(p)^{-1}}]_{1,1}$, $[A_{II}^{(p)^{-1}}]_{1,N-1}$ with $p = 1, 2$ will give us the dispersion relation.

According to [107], inverse of a symmetric tridiagonal matrix $T = \begin{bmatrix} a & b & & 0 \\ b & \ddots & \ddots & \\ & \ddots & \ddots & b \\ 0 & & b & a \end{bmatrix}_{n \times n}$ may be written as

$$(T^{-1})_{ij} = \begin{cases} (-1)^{i+j} \frac{1}{b} \frac{U_{i-1}(a/2b) U_{n-j}(a/2b)}{U_n(a/2b)}, & \text{if } i \leq j \\ (-1)^{i+j} \frac{1}{b} \frac{U_{j-1}(a/2b) U_{n-i}(a/2b)}{U_n(a/2b)}, & \text{if } i > j \end{cases} \tag{3.27}$$

where, $U_n, n \geq 0$ are Chebyshev polynomials of the second kind satisfying the recurrence relation: $U_{n+1}(x) = 2xU_n(x) - U_{n-1}(x), \quad n \geq 1$ with $U_0 = 1$ and $U_1 = 2x$. These functions can also be written as

$$\begin{cases} U_n(x) = \frac{\sin(n+1)\theta}{\sin\theta} & for \quad \cos\theta = x \quad , \quad |x| < 1 \\ U_n(x) = \frac{\sinh(n+1)\theta}{\sinh\theta} & for \quad \cosh\theta = x \quad , \quad |x| > 1 \end{cases} \tag{3.28}$$

Using the Chebyshev functions introduced above, we may write the elements of the inverse matrix as

follows:

$$[A_{II}^{(1)^{-1}}]_{1,1} = -\frac{U_{N-2}(x_1)}{U_{N-1}(x_1)} \qquad [A_{II}^{(1)^{-1}}]_{1,N-1} = (-1)^{N+1}\frac{1}{U_{N-1}(x_1)} \tag{3.29a}$$

$$[A_{II}^{(2)^{-1}}]_{1,1} = -\frac{1}{\beta}\frac{U_{N-2}(x_2)}{U_{N-1}(x_2)} \qquad [A_{II}^{(2)^{-1}}]_{1,N-1} = (-1)^{N+1}\frac{1}{\beta}\frac{1}{U_{N-1}(x_2)} \tag{3.29b}$$

Here, $x_1 = \Omega^2/2 - 1$, $x_2 = \alpha\Omega^2/2\beta - 1$. Therefore, for any arbitrary $N \geq 3$, the dispersion relation may be written in the following form:

$$(e^{-2i\mu} + e^{2i\mu}) + J_1(e^{-i\mu} + e^{i\mu}) + J_2 = 0 \tag{3.30}$$

or alternatively,

$$\cos^2\mu + \frac{J_1}{2}\cos\mu + \frac{J_2 - 2}{4} = 0 \tag{3.31}$$

To facilitate the notation, $[A_{II}^{(1)^{-1}}]_{1,1}$ and $[A_{II}^{(1)^{-1}}]_{1,N-1}$ have been replaced by A_1 and A_2. Similarly, $[A_{II}^{(2)^{-1}}]_{1,1}$ and $[A_{II}^{(2)^{-1}}]_{1,N-1}$ have been replaced with B_1 and B_2 for a more compact notation. Then, The invariant coefficients J_1 and J_2 may be expressed in closed form as follows.

$$J_1 = \frac{-1}{\beta^2 A_2 B_2}\left[A_2\left(2\beta + \gamma - \alpha\Omega^2\right) + \beta^2 B_2\left(2 + \gamma - \Omega^2\right) - 2\beta^2\left(A_1 B_2 + A_2 B_1\right)\right] \tag{3.32a}$$

$$J_2 = 2 + \frac{1}{\beta^2 A_2 B_2}\left[\Big(\left(2 + \gamma - \Omega^2\right) - 2A_1\Big)\Big(\left(2\beta + \gamma - \alpha\Omega^2\right) - 2\beta^2 B_1\Big) - \gamma^2\right] \tag{3.32b}$$

Provided that $A_2 B_2 \neq 0$, the solution may be written in a similar manner as Equation (3.8)

$$(\cos\mu)_{1,2} = \frac{1}{4}\left(-J_1 \pm \sqrt{8 + J_1^2 - 4J_2}\right) \tag{3.33}$$

When N approaches infinity, three distinct regions are identified in the band structure of the system. We introduce the variables $\omega_{min} = \min(\omega_1, \omega_2)$ and $\omega_{max} = \max(\omega_1, \omega_2)$ to facilitate the discussion that follows. Depending on the relative properties of the two chains,

1. for $\omega < 2\omega_{min}$, the dispersion relation remains quadratic in $\cos\mu$.

2. for $\omega \in [2\omega_{min}, 2\omega_{max}]$, one of A_2 or B_2 goes to zero and the dispersion relation becomes linear in $\cos\mu$.

3. for $\omega > 2\omega_{max}$, both A_2 and B_2 go to zero making the dispersion relation independent of μ.

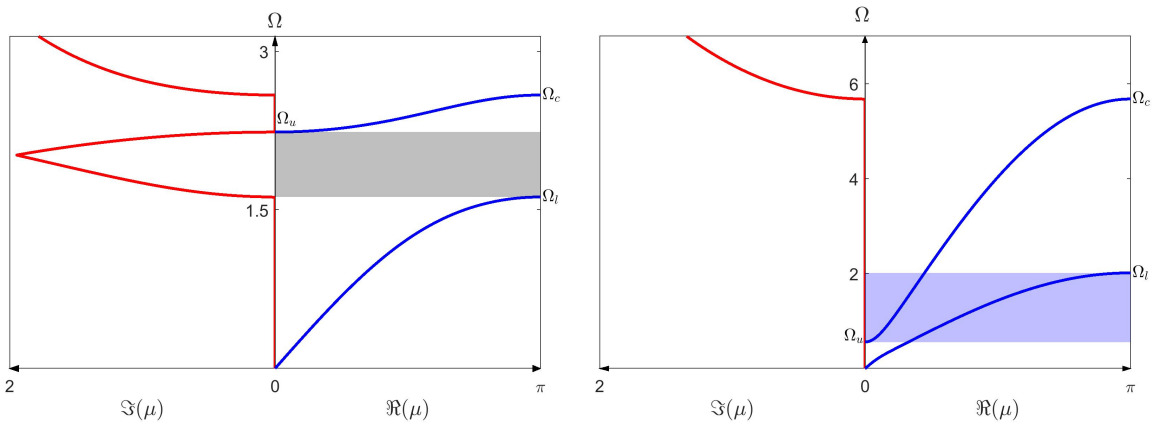

(a) (b)

Figure 3.2: Band structure of the fully-coupled system for two cases. (a) $\alpha = 0.25, \beta = 0.02$ and $\gamma = 1$ leading to band gap formation and (b) $\alpha = 0.25, \beta = 2$ and $\gamma = 0.0625$ leading to double-speed wave propagation. Here, α and β are the mass and stiffness ratio between the two chains and γ is the connector stiffness ratio. The blue and red curves show the real and imaginary parts of μ, respectively. The normalized frequency values Ω_l, Ω_u and Ω_c indicated on the figures were obtained using Eq. (3.34).

We note that the bounding values $2\omega_1$ and $2\omega_2$ that mark frequencies at which the dispersive nature of the system undergoes significant changes, indicate the cut-off frequencies of each individual monoatomic chain.

3.3 Dispersion Properties of Example Meta-Chains

In this section, we use the dispersion relations obtained in the previous part along with illustrative examples to discuss the dispersive properties of meta-chains with full and partial coupling. In-house MATLAB® codes are used for all numerical simulations in this section and the one that follows.

3.3.1 Fully-Coupled Chains

In this example, the band structure properties of a fully-coupled system are examined. First, we set problem parameters to $\alpha = 0.25, \beta = 0.02$ and $\gamma = 1$. Fig. 3.2a shows that the band structure of the system consists of an acoustic branch and an optical branch, with a band gap forming in between. Since group velocity on the optical branch is positive, the system's behavior is similar to that of a 1-D Acoustic Metamaterial - i.e. the conventional monoatomic chain with spring-mass resonators. This is expected if we notice that the fully-coupled configuration could also be interpreted as a periodic 1-D chain with interconnected internal resonators. The band gap's lower and upper edge frequencies as

well as the cut-off frequency are determined from Equations (3.7) and (3.8) as follows:

$$\Omega_l = \sqrt{\frac{1}{2}\left(\delta_1 - \sqrt{\delta_2}\right)} \qquad \Omega_u = \Omega_R\sqrt{1+\alpha} \qquad \Omega_c = \sqrt{\frac{1}{2}\left(\delta_1 + \sqrt{\delta_2}\right)} \tag{3.34}$$

with

$$\delta_1 = \left[4 + \Omega_R^2(1+\alpha)\right] + 4\Omega_2^2 \tag{3.35a}$$

$$\delta_2 = \delta_1^2 - 16\left[4\Omega_2^2 + \Omega_R^2(1+\alpha\Omega_2^2)\right] \tag{3.35b}$$

Here, $\Omega_2 = \omega_2/\omega_1$, $\Omega_R = \omega_r/\omega_1$ and $\omega_r = \sqrt{k_3/m_2}$. Using the analogy with the 1-D AM, the variable

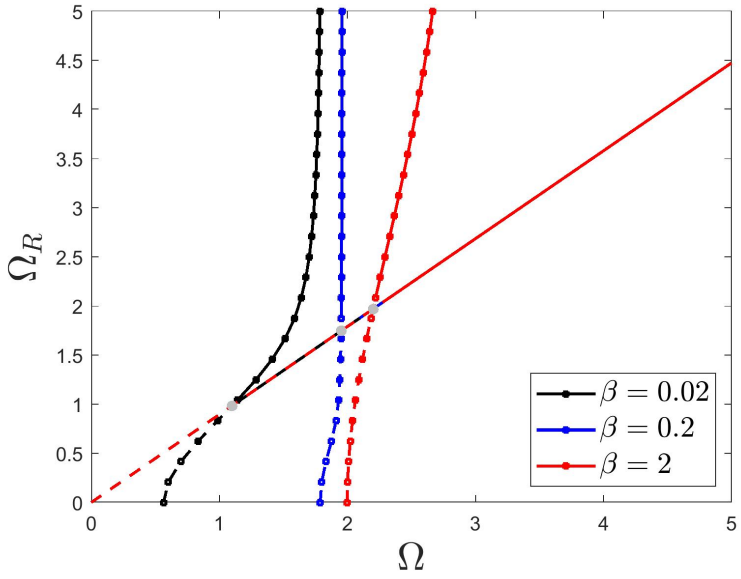

Figure 3.3: Evolution of the band gap edge frequencies with the normalized resonance frequency Ω_R when $\alpha = 0.25$. Different colors correspond to different values of the stiffness ratio β. The curves with markers show the lower edge while the solid curve shows the upper edge of the band gap, which overlaps for different β values. Dashed lines show regions where Ω_u lies below Ω_l, leading to double-speed wave propagation.

Ω_R may be interpreted as the normalized resonance frequency of the resonators had they not been connected to form a secondary chain. Ω_l and Ω_u are the lower and upper edge frequencies of the first band gap and Ω_c is the cut-off frequency beyond which the system has a complete stop band. It's interesting to note that the upper edge frequency in this case is the same as that of the 1-D AM [1]. We may, thus, conclude that connecting the resonators (and consequently the variable β) doesn't affect the upper edge frequency.

Double-speed wave propagation The analytical expressions in Eq. (3.34) reveal another interesting property of the system. Comparing the expressions for the lower and upper edge frequencies shows that a critical value $\Omega_R^{cr} = \sqrt{\frac{4\beta/\alpha}{\beta/\alpha+\alpha}}$ exists at which the behavior of the system undergoes a dramatic change. Specifically, for $\Omega_R < \Omega_R^{cr}$, Ω_u will be smaller than Ω_l. In this case, the band gap will close and instead, a region with double-speed wave propagation appears. In other words, if $\Omega_R > \Omega_R^{cr}$, the frequency region $[\Omega_l, \Omega_u]$ is a band gap while if $\Omega_R < \Omega_R^{cr}$, the system supports two propagation waves of different phase speeds in the frequency region $[\Omega_u, \Omega_l]$. This second case is shown in Fig. 3.2b for parameters $\alpha = 0.25, \beta = 2$ and $\gamma = 0.0625$. This phenomenon is not observed in 1-D AMs since their dispersion relation is linear in $\cos\mu$. In this case, the dispersion relation, which is quadratic in $\cos\mu$, allows for two independent propagating waves.

Next, we keep α constant and investigate how the variation of parameters Ω_R and β affects the band gap edge frequencies. Fig. 3.3 shows the evolution of the edge frequencies with Ω_R for sample β values. The upper edge frequency of the band gap is independent of β and varies linearly with Ω_R, as shown in Eq. (3.34). However, the lower edge frequency of the band gap tends to increase with larger β values. The region with the dashed lines shows parameter ranges where the upper edge frequency falls below the lower edge frequency. These parameter ranges correspond to regions of double-speed wave propagation in the system. The gray circles with coordinates $[\Omega_R^{cr}\sqrt{1+\alpha}, \Omega_R^{cr}]$ on the figure show critical points at which the switch in behavior occurs.

3.3.2 Partially-Coupled

In this section, we highlight the fundamental dispersion characteristics of the partially-coupled configuration in two main sets of examples. In the first set, we show how characteristic waves interact to form the band structure of the system and show the effect of skipping masses in the formation of new band gaps. In the second part, we explain how fine-tuning the parameters of the system can lead to the formation of flat bands in the frequency spectra of the system.

Wave interactions and band gap formation We consider a configuration with one skipped mass ($N = 2$) and set problem parameters to $\alpha = 5, \beta = 0.1$ and $\gamma = 1$. As Eq. (3.13) shows, two characteristic waves with non-dimensional wave numbers μ_1 and μ_2 exist. Figures 3.4a and 3.4b show the evolution of phase constants (real part of the non-dimentional wave number pair) and attenuation constants (imaginary part of the non-dimensional wave number pair), respectively. The former dominates the characteristics of propagating waves while the latter determines the attenuation properties of the

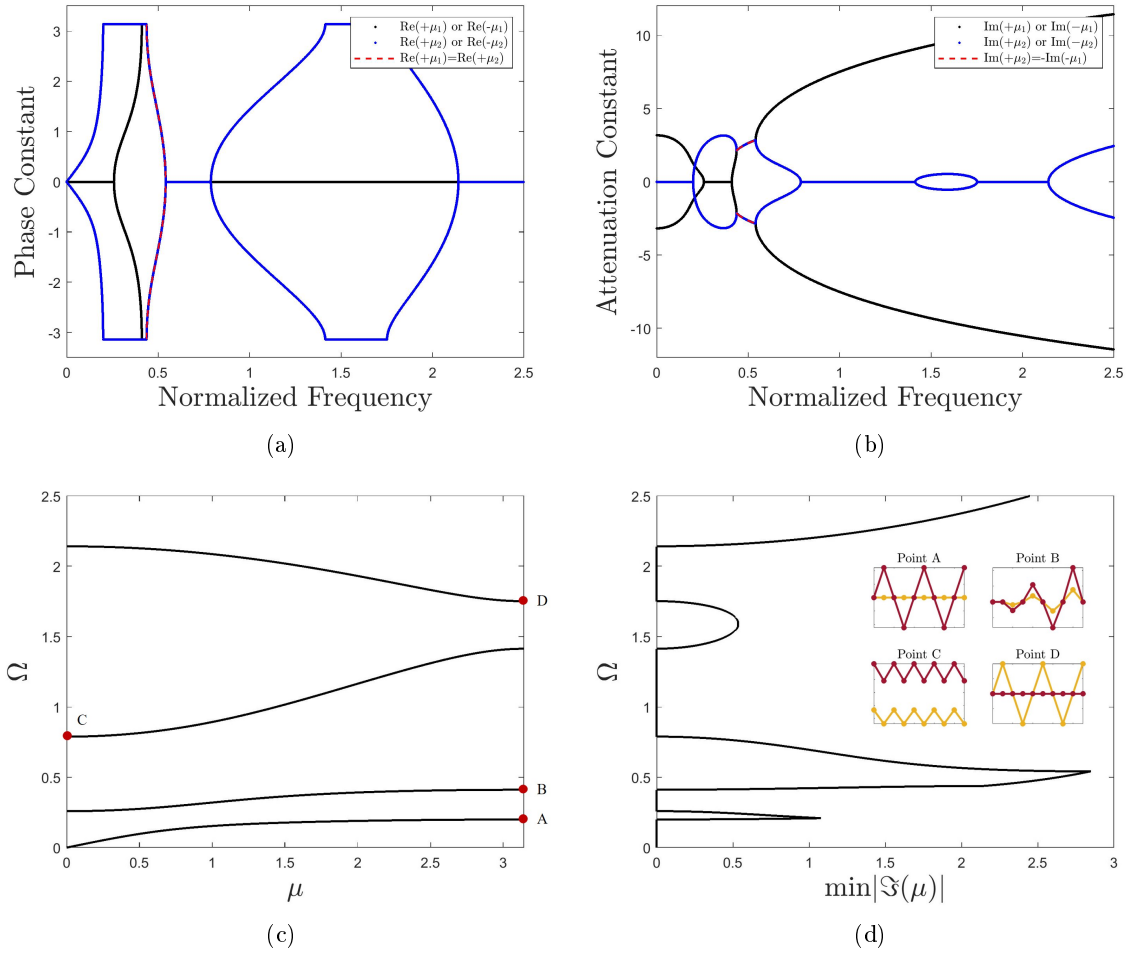

Figure 3.4: Complex and simplified band structure of the meta-chain with one skipped mass. Here, the mass ratio $\alpha = 5$, stiffness ratio $\beta = 0.1$ and connector stiffness ratio $\gamma = 1$. (a) Real part of the non-dimensional wave number pair dominating the characteristics of propagating waves. (b) Imaginary part of the non-dimensional wave number pair, governing the attenuation properties. (c) Dispersion curves. (d) Minimum absolute value of attenuation constants. Insert shows Bloch modes of the system over five unit cells at points A, B, C, and D.

system. The dashed red curves mark the regions where one wave number is the complex-conjugate of the other. The figures show that the two waves strongly interact to form several band gaps. The simplified band structure of the system is shown in Figure 3.4c-3.4d. Unlike the fully-coupled case, where the system resembled an AM, the partially-coupled case shows features of both BS and LR mechanisms in its frequency spectra. The insert in this figure shows Bloch modes of the system at selected band gap edge locations. Figures 3.5a-3.5b show the dispersion curves for two and three skipped masses. Changing the frequency with which the two chains are connected, alters the band structure of the system, leading to the formation of new gaps and elimination of others. We also note the presence of several negative group velocity bands in the band structure of the system. From a design standpoint,

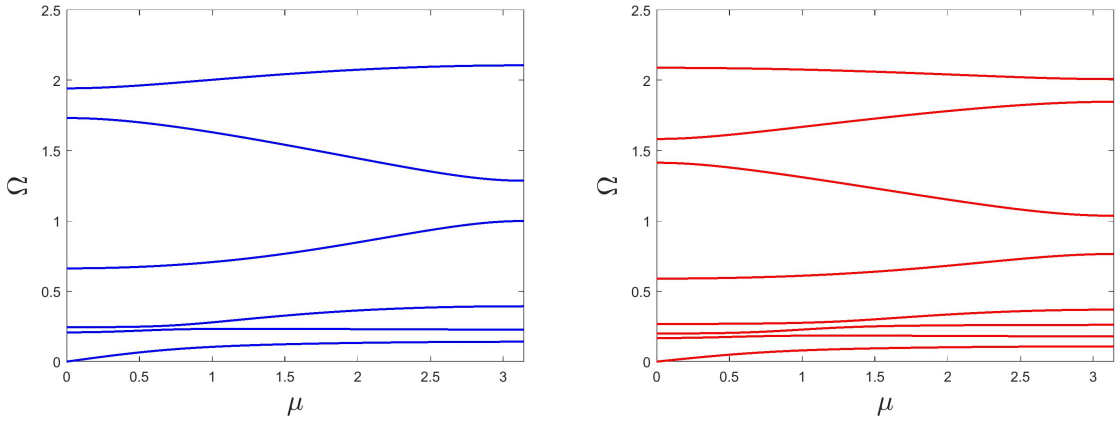

Figure 3.5: Dispersion curves for partially-coupled system with different number of skipped masses. Remaining problem parameters are the same as the case for $N = 2$. (a) $N = 3$ and (b) $N = 4$. Increasing the number of skipped masses leads to the formation of new band gaps and elimination of others.

it is of interest to study the effect of connection stiffness on edge frequencies as well as the attenuation strength within the band gaps. Fig. 3.6 shows contours of the minimum attenuation strength for different values of N. These contours show that attenuation is strongest close to the line $\Omega = \Omega_R$, as is the case in locally-resonant systems. The figure also suggests that for the most prominent band gaps in the system, edge frequencies increase with increasing Ω_R values. The figures show that at special values of Ω_R, lower and upper band gap edges nearly coincide. These points are marked with white circles. This suggests that the proposed system has near-zero group velocity bands for certain set of parameters. This phenomenon will be explored in more detail next.

Emergence of flat bands Zero group velocity dispersion bands (flat bands) have recently received a lot of attention in the context of optical and acoustic waveguides [108, 109]. These bands are usually associated with the existance of degenerate modes in the system and have a wide range of applications in sensing, telecommunications and storage devices [110, 111]. Here, we show how fine-tuning the proposed system leads to the formation of flat bands with near-zero group velocity.

Informed by the results obtained in the previous part, we set problem parameters α and β as before but change the connection stiffness ratio γ such that the variable Ω_R is 1.4, 0.98 and 0.74 for one, two, and three skipped masses, respectively. Figures 3.7a-3.7c show the dispersion curves for the three cases. Flat bands appear in the band structure of the system.

The set of parameters that bring these points into existence correspond to the overlapping of the

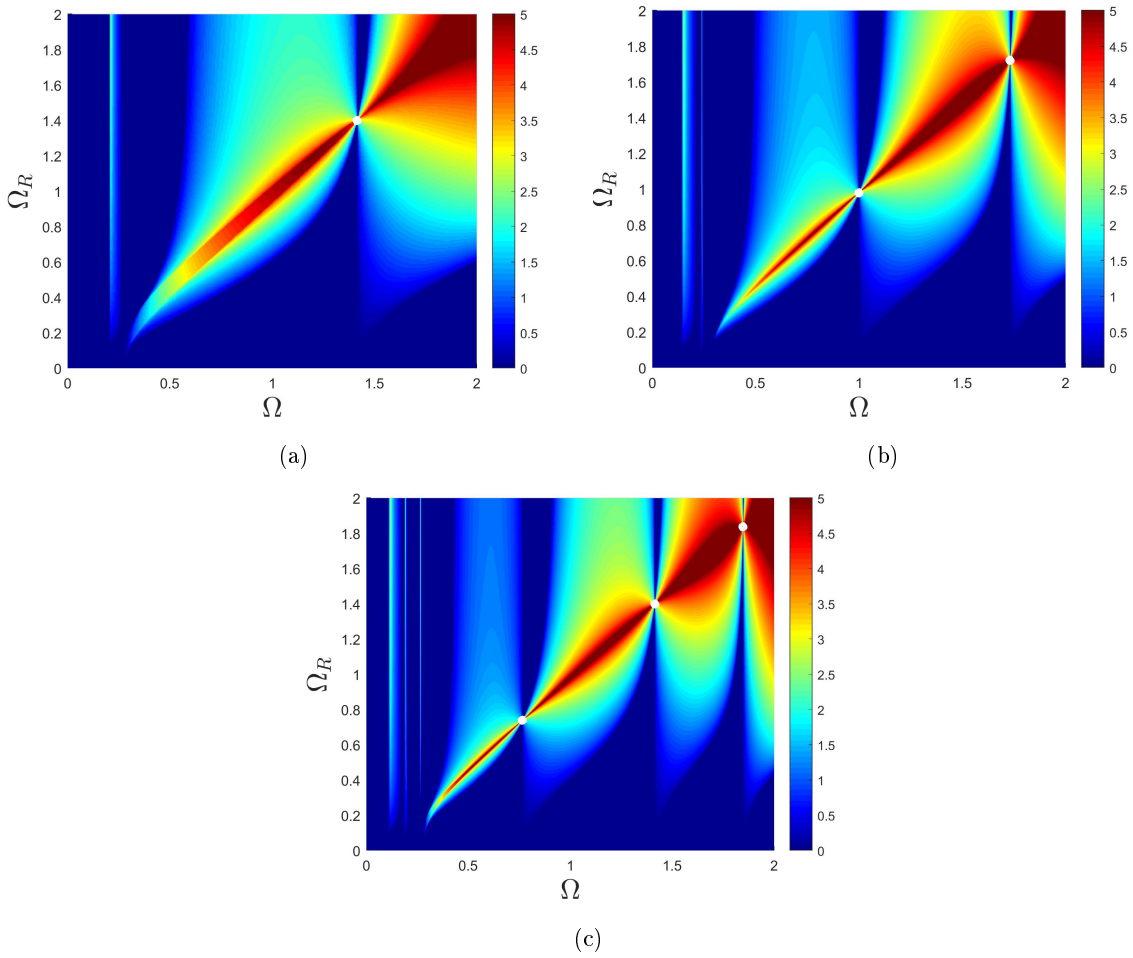

Figure 3.6: Contours of minimum attenuation strength for the partially-coupled system. (a) $N = 2$, (b) $N = 3$ and (c) $N = 4$. The bright nodes where the width of the attenuation zones vanish (1 node in (a), 2 nodes in (b), and 3 nodes in (c)) correspond to frequency combinations at which flat bands emerge. Color bar range is set equal for all cases to facilitate comparison.

resonance frequency of the mass directly attached to the reference chain, $\sqrt{\frac{\gamma+2\beta}{\alpha}}$, and the natural frequencies of the reference chain's interior unit cell masses $\Omega^* = \sqrt{2(1+\cos\frac{j\pi}{N})}$ with j ranging from 1 to $N-1$. The latter expression corresponds to the natural frequencies of a chain with $N-1$ masses and same properties as the reference chain. This may be understood better if we notice that the degenerate modes on flat bands all correspond to motions of the unit cell where the leftmost mass in the reference chain is at rest while motion in the second chain is confined to the mass directly attached to the reference chain (Figure 3.7d). Therefore, tuning the connection parameter γ to $\alpha{\Omega^*}^2 - 2\beta$, results in the appearance of flat bands and localized modes. As β increases, the resonance condition is satisfied only by reducing γ. Therefore, if β is greater than $\frac{\alpha}{2}{\Omega^*}^2$, for the resonance condition to be satisfied, γ has to be negative, which is not physical. In general, for very low values of γ, the

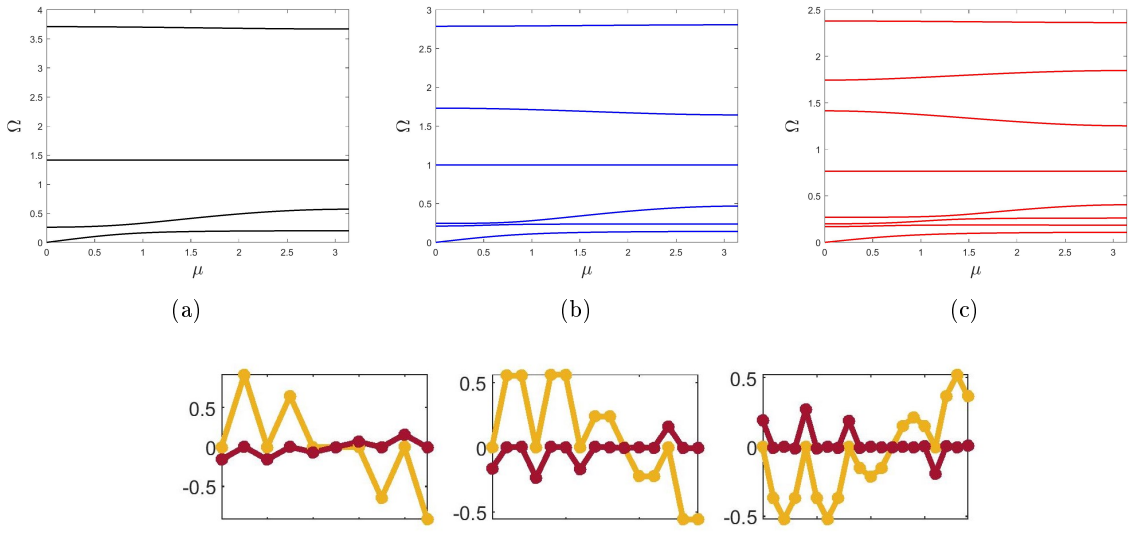

Figure 3.7: Emergence of flat bands in the band structure of the partially-coupled system. (a) $N = 2$ and $\Omega_R = 1.4$ and (b) $N = 3$ and $\Omega_R = 0.98$, and (c) $N = 4$ and $\Omega_R = 0.74$. (d) Flat band Modes at $\mu = \pi/4$ over five unit cells of each configuration. Reference and secondary chains are represented in yellow and dark red, respectively.

coupling between the two chains becomes weak and the band structure of the system tends towards that obtained by the individual supercell analysis of the two monoatomic chains with a periodicity length $R = Nd$ [106].

3.4 Example Devices

In this section, we will design two spring-mass devices based on the proposed meta-chain configurations. The first example shows how a fully-coupled configuration may be exploited for designing a band-pass filter. In the second example, we show that using a combination of partially-coupled unit cells with varying periodicity widens the frequency region over which attenuation is achieved, similar to a rainbow trapping effect.

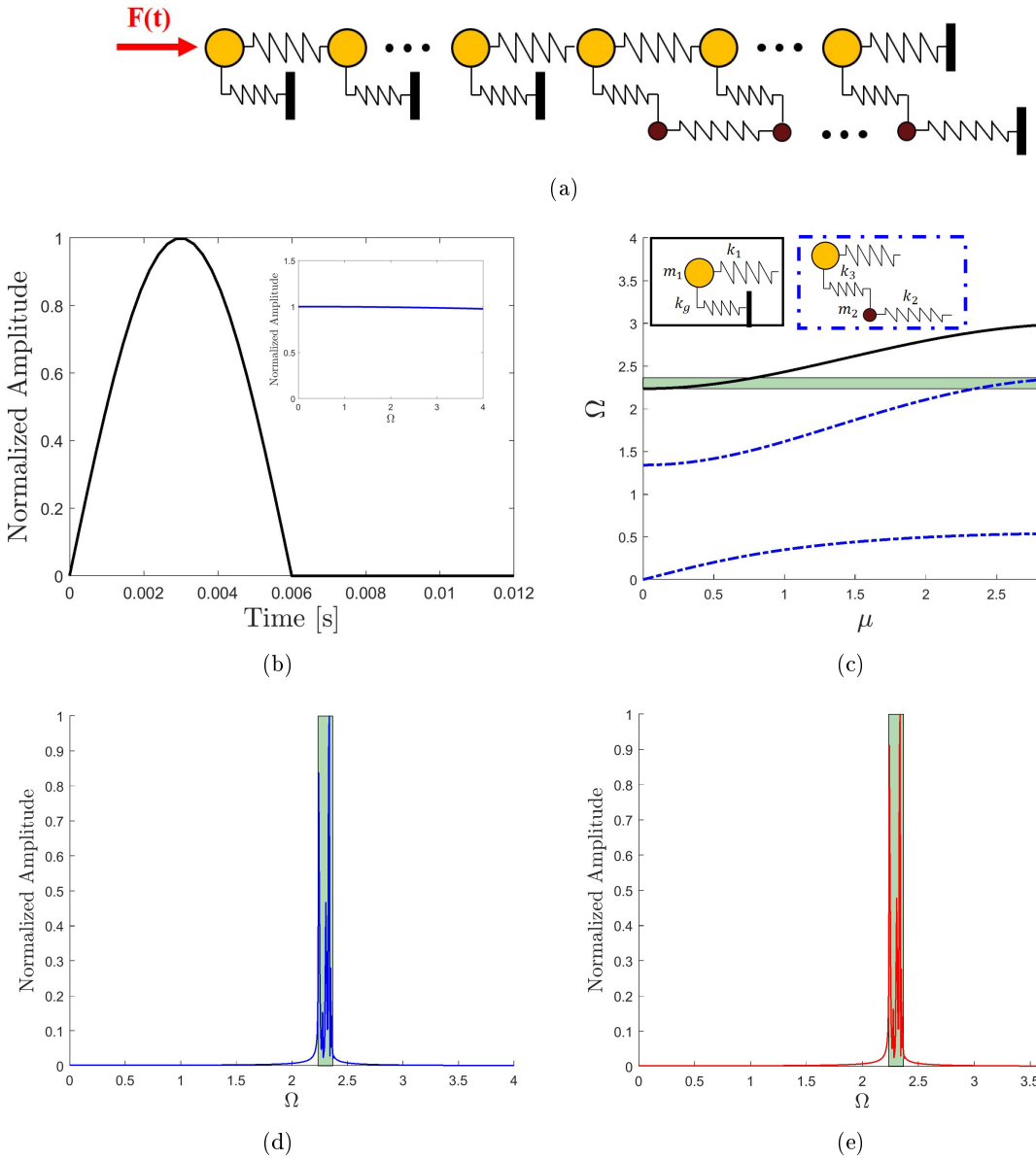

Figure 3.8: An example of a narrow-band pass filter device. (a) Schematic of the device which consists of a grounded chain connected in series to a fully coupled chain. (b) Broadband input signal. The insert shows the normalized spectral amplitude of the input over the frequency region of interest. (c) Dispersion curves for unit cells of the grounded chain (black) and fully-coupled meta-chain (blue). The shaded green band represents the range of frequencies that are allowed to pass as a result of this design. (d)-(e) Normalized spectral amplitude of the output at observation points for the reference and the secondary chain, respectively. The observation points are located at the 20th unit cell of the fully-coupled meta-chain.

3.4.1 Band-Pass Filter

Numerous designs for wave-filtering devices have been proposed in the literature [53, 103, 104]. Here, We design a band-pass filter using a combination of a grounded chain and a fully-coupled meta-chain

(Fig. 3.8a). The former may also be realized using the fully-coupled configuration with a large α value. We examine the response of the system under a broadband impact load (Fig. 3.8b). First, we carry out a unit cell analysis of the two configurations assuming both systems to be infinitely periodic. We choose the physical parameters such that the pass bands of the two chains overlap only in a narrow frequency region. Fig. 3.8c shows the dispersion curves of the considered unit cells and the green region marks the designed pass-band region where both the grounded and fully coupled chains simultaneously propagate waves. A non-dimensional parameter $\gamma_g = k_g/k_1$ is defined and set to 5 where k_g is the grounding stiffness. We set the other parameters associated with the meta-chain to $\alpha = 5, \beta = 0.1$ and $\gamma = 1.5$. The reference chain has the same properties as the grounded chain. The normalized frequency Ω is defined as before. In order to show how such a device performs, we set up a numerical model of a finite prototype consisting of a grounded chain connected to a fully-coupled meta-chain. Each subsystem consists of 25 unit cells. The reference chain has mass $m_1 = 0.056$ [kg] and spring constant $k_1 = 100$ [N m^{-1}]. All other non-dimensional parameters are as mentioned above. The half-sine loading $F(t)$ resembles an impulse and is applied at the left end of the device. We run a time-history simulation for 25 seconds and use Fourier Transform to identify the frequency content of response at the 20^{th} unit cell of the meta-chain. Figures 3.8d-3.8e show that the frequency content of the response is confined in a narrow-band pass region, suggesting that the device has successfully depleted the output of other frequencies. The grounding stiffness and/or the physical parameters affecting the cutoff frequency Ω_c of the meta-chain may be changed to control the operating frequency region of the device.

3.4.2 Low-frequency rainbow-trap filter

In Section 3.3.2, we showed that skipping different number of masses in the partially-coupled configuration changes the band structure of the system and the location of band gaps. Here, this effect is leveraged to design a filtering device consisting of unit cells with two, three and four skipped masses. We show that the overlap of band gaps for the carefully-designed subsystems broadens the attenuation region, similar to a rainbow trapping effect [16, 112].

We consider a partially-coupled meta-chain consisting of a total number of 240 masses (120 masses per chain) with system parameters $\alpha = 5$, $\beta = 0.1$ and $\Omega_R = 0.75$. The mass (m_1) and stiffness (k_1) of the reference chain are 0.056 [kg] and 100 [N m^{-1}]. First, we consider three initial periodic configurations of this system with two (40 unit cells), three (30 unit cells) and four skipped masses (24 unit cells). We refer to these configurations as Type 1, Type 2 and Type 3, respectively. Fig. 3.9a shows sample

dispersion curves and undamped frequency response functions (FRFs) for Type 1 configuration. For all the setups considered here, we apply equal harmonic forces on the leftmost masses of both chains and compute the Frequency Response Functions (FRFs) for masses on the other end of the chains using standard techniques. Fig. 3.9b shows the overlaid FRF plots in the low-frequency region and the overlap of band gaps for the three configurations.

Next, we consider a graded configuration with the same number of masses but with the meta-chain consisting of ten unit cells of each type. The FRF of this composite configuration is compared to that of the individual constituent coupled chains. The numerical simulations assume a modal damping of 0.5%. Figure 3.9c shows how a major attenuation region forms in the response spectra of the new system. The band gap formed is wider than the ones for each type shown in 3.9b, suggesting that changing the connection frequency between the two chains may be used as a means to design devices with different wave-filtering properties.

We note that unlike the rainbow-trapping mechanism where absorbers of varying resonance frequencies are used to widen the band gap, the physical parameters of the system do not vary in our proposed configuration. Rather, it is the change in the topology of the system (varying connection locations) that results in the broadening of the attenuation zones. This is a key in our modular design approach where building blocks of distinct dynamic properties may be stitched together to realize more synergistic effects.

3.5 Conclusions and future work

Previous work on systems consisting of elements coupled in parallel has shown that they possess novel dispersion properties, including strong attenuation zones and interaction between BS and LR mechanisms [47, 69]. In this work, we proposed two one-dimensional spring-mass configurations consisting of coupled monoatomic chains. We showed that wave propagation in the fully-coupled system has a dual nature depending on system parameters, with the behavior of the system switching between that of an acoustic metamaterial (AM) and a structure that allows for the simultaneous propagation of two characteristic waves. Wave propagation in the partially-coupled system showed even more complex behavior, including several BS and LR band gaps, emergence of flat bands and negative group velocity bands. By combining coupled chains with different modularities, we were able to realize several devices with interesting dynamic properties including narrow-band pass filtering and broad low frequency band gap. The main conclusions of this work may be summarized as follows.

For the fully-coupled system:

- If $\Omega_R = \omega_r/\omega_1 > \sqrt{\frac{4\beta/\alpha}{\beta/\alpha+\alpha}}$, the behavior of the system is similar to that of a 1-D lattice with internal resonators: the band structure consists of an acoustic and an optical band and the band gap has features of a local resonance mechanism.

- If $\Omega_R = \omega_r/\omega_1 < \sqrt{\frac{4\beta/\alpha}{\beta/\alpha+\alpha}}$, no band gaps form. Instead, a double-speed wave propagation zone emerges. In this frequency range, the meta-chain supports the propagation of two characteristic waves unlike what is observed in conventional 1-D mass-spring configurations.

For the partially-coupled system:

- Complex band structure of the system shows that the characteristic waves strongly interact to form the band structure. Several band gaps with BS and LR features form in the frequency spectra.

- Changing the frequency with which the chains are connected affects the band structure significantly and leads to the formation of new gaps and elimination of others. This behavior may be leveraged to realize a broad range of dynamic behaviors with small changes in the system's configuration.

- Fine-tuning the parameters leads to degeneracy and the emergence of flat (near-zero group velocity) bands at frequencies we are able to predict analytically. The formation of these bands is due to the overlapping resonances within the unit cell.

As we noted in section 3.3.2, several negative group velocity bands appear in the band structure of the partially-coupled configuration. As the presence of such bands is a prerequisite for designing systems with negative refractive properties [106], a future extension of this work may include investigating 2D counterparts of the present system to achieve wave focusing. We also showed that changes in connection stiffness may lead to significant changes in the band structure. Therefore, studying similar systems where the connection stiffness is modulated in space/time would be another interesting extension to this study. With the advent of nonlinear metamaterials, several works have recently shown that nonlinearity and asymmetry in systems of similar configurations lead to unusual properties such as localization and nonreciprocity [113, 114]. Hence, investigating the effects of nonlinearity (in individual chains and/or connection springs) on wave propagation properties of the proposed systems may be of interest in the future.

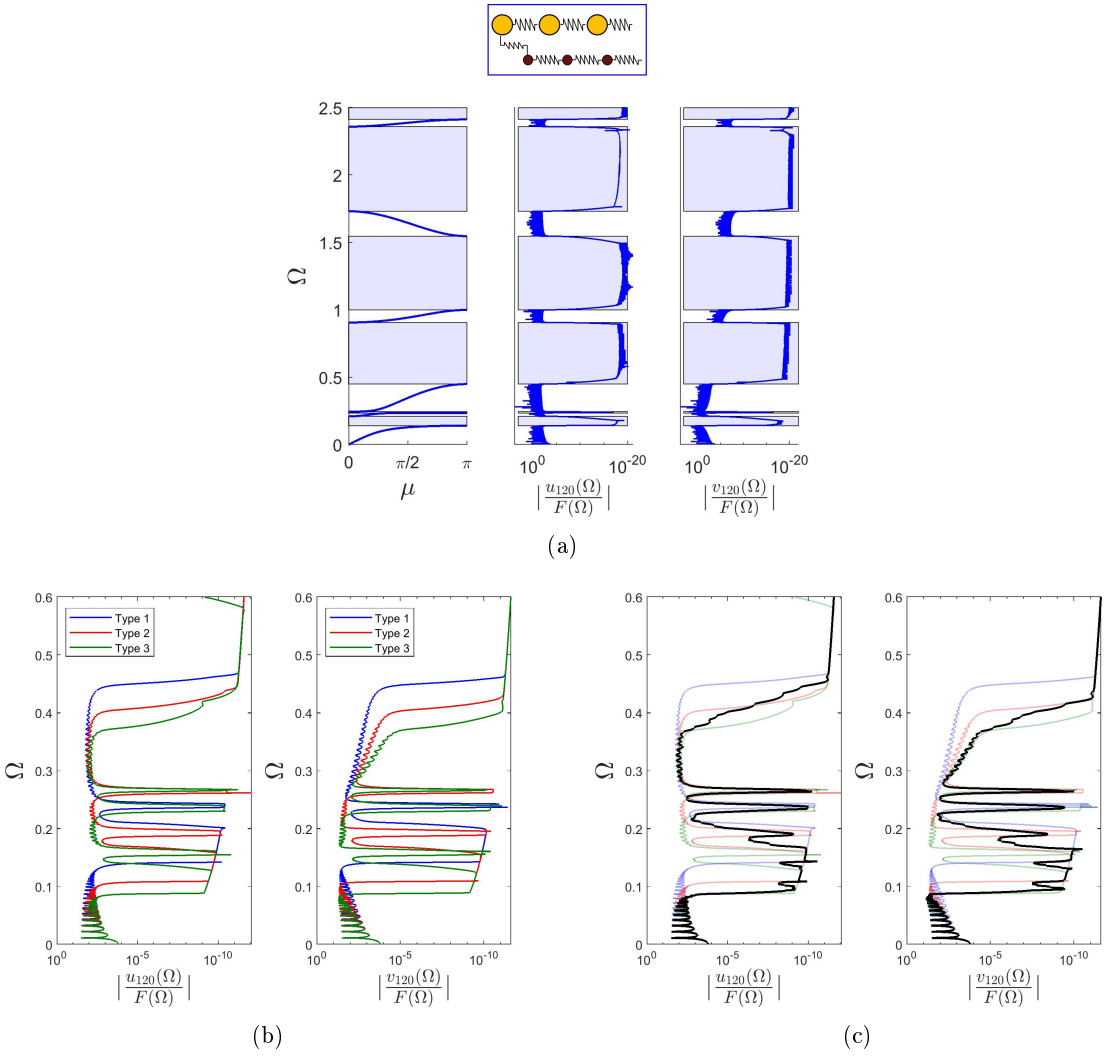

Figure 3.9: An example of the rainbow-trap device. (a) Sample unit-cell configuration, dispersion curves and undamped FRF for Type 1 meta-chain with two skipped masses per unit cell. (b) overlaid FRFs of Type 1, 2 and 3 meta-chains with 0.5% damping. The band gaps overlap for the three systems. (c) FRF for the graded configuration (black) shows band gap widening. In all cases, Observation points are located at the right-most masses of the two chains, u_{120} and v_{120}.

Chapter 4

Amplitude-dependent dispersion of Rayleigh waves via nonlinear locally-resonant metamaterials

4.1 Introduction

Rayleigh waves are a type of surface waves that propagate close to the surface of solids. They cause particles to move in an elliptical motion, the amplitude of which decreases with depth. The study of Rayleigh waves is of importance across many areas of science and engineering, from site characterization [115, 116], and non-destructive testing over different length scales [117, 118] to seismic protection of the built environment [119, 120].

In earthquake engineering, Rayleigh waves are considered the most destructive type of seismic waves; responsible for most damage to the built environment. Currently, the most common strategy for seismic protection is using traditional seismic isolation systems [121]. However, these systems produce significant horizontal displacements under large earthquakes [122]. Moreover, man-induced seismicity has become a major issue in regions where structures were not originally designed for earthquakes [123]. Therefore, there's a need for novel strategies to protect critical urban areas against earthquakes.

Metamaterials, first introduced in electromagnetics, are engineered structures designed to filter, modulate or bend waves. It is known that waves in certain frequency ranges cannot propagate in these systems due to the existence of band gaps in their frequency spectra. Over the recent years, researchers have successfully transferred these concepts to the fields of geophysics and earthquake engineering in order to remotely shield structures [34, 119, 16, 124] from Rayleigh waves. Both phononic systems and metamaterial designs have been proposed. Some solutions have also aimed at bending or redirecting waves to protect structures. However, most research in this area has focused on linear elastic meta-structures, whose dispersion characteristics are fixed once the design is finalized.

More recently, several works have shown that embedding nonlinearity in the design of metamaterials offers enhanced control over wave transmission by making the response of the structure passively

tunable, by localizing the response or broadening the operational frequency range. Figure 4.1 shows a schematic of how harnessing nonlinearity may realize unprecedented control over surface waves.

In this chapter, we propose a preliminary framework to analyze the interaction of Rayleigh waves with a periodic array of nonlinear resonators. First, The classical problem of a half-space with free surface boundary conditions is revisited for reference. Next, a half-space with linear resonators distributed on its surface is investigated. We build upon the work of [18] by using similar problem parameters for the case of a homogeneous half-space and a half-space with linear resonators. In the end, an approximate framework is presented for studying the interaction of Rayleigh waves with Duffing-type oscillators distributed at the surface.

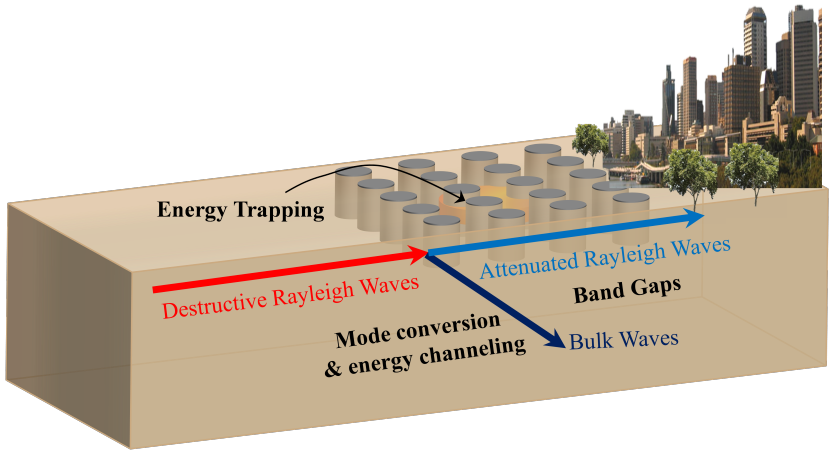

Figure 4.1: Schematic of nonlinear meta-structures and the potential mechanisms involved for controlling seismic waves.

4.2 Homogeneous half-space

The configuration of the problem is shown in Figure 4.2a. We start by writing the equations of motion. In what follows, u and v denote displacement of particles in the x and y directions, respectively.

$$(\lambda+2\mu)\left[\frac{\partial^2 u}{\partial x^2}+\frac{\partial^2 v}{\partial x\partial y}\right]-\mu\left[\frac{\partial^2 v}{\partial x\partial y}-\frac{\partial^2 u}{\partial y^2}\right]=\rho\frac{\partial^2 u}{\partial t^2}\,, \tag{4.1a}$$

$$(\lambda+2\mu)\left[\frac{\partial^2 v}{\partial y^2}+\frac{\partial^2 u}{\partial x\partial y}\right]-\mu\left[\frac{\partial^2 u}{\partial x\partial y}-\frac{\partial^2 v}{\partial x^2}\right]=\rho\frac{\partial^2 v}{\partial t^2}\,. \tag{4.1b}$$

where λ and μ are the Lamé constants and ρ is the density. The above equation may also be written in the following form:

$$(\lambda+2\mu)\nabla(\nabla.\boldsymbol{U})-\mu\nabla\times\nabla\times\boldsymbol{U}=\rho\ddot{\boldsymbol{U}} \tag{4.2}$$

where $\boldsymbol{U} = \{u, v\}'$ and ∇ is the gradient operator. Next, we introduce the Helmholtz decomposition for the displacement vector $\mathbf{U}$.

$$\mathbf{U} = \nabla\Phi + \nabla \times \boldsymbol{\Psi} \tag{4.3}$$

where, Φ and $\boldsymbol{\Psi}$ are scalar and vector potentials, respectively. Plugging (4.3) in (4.2) and having in mind that the vector identities $\nabla \times (\nabla\Phi)$ and $\nabla.(\nabla \times \boldsymbol{\Psi})$ vanish, we get two uncoupled equations as follows:

$$\frac{\partial^2 \Phi}{\partial t^2} = c_p^2 \nabla^2 \Phi \,, \tag{4.4a}$$

$$\frac{\partial^2 \Psi_z}{\partial t^2} = c_s^2 \nabla^2 \Psi_z \,. \tag{4.4b}$$

where $c_p = \sqrt{(\lambda + 2\mu)/\rho}$ and $c_s = \sqrt{\mu/\rho}$ are the longitudinal and shear wave speeds.Considering

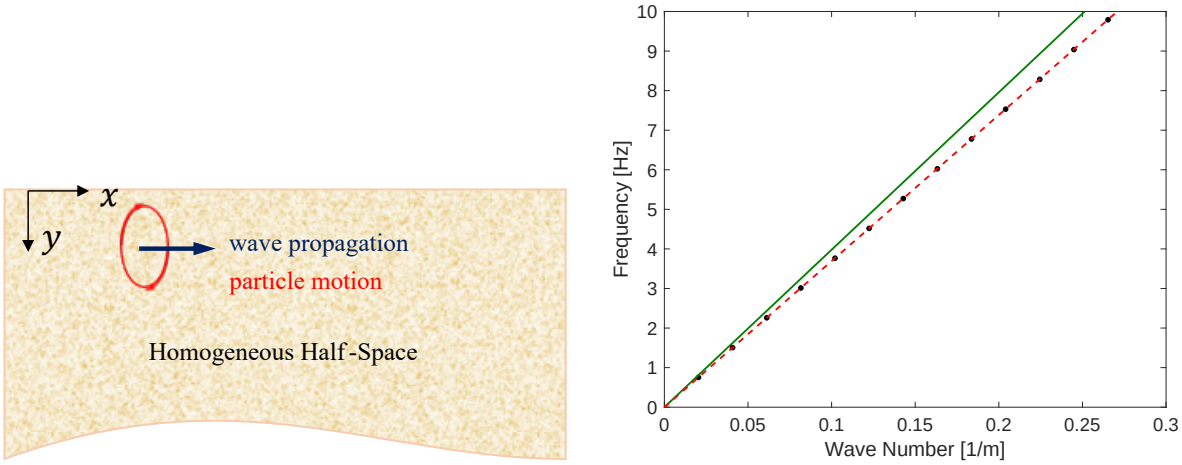

(a) (b)

Figure 4.2: Classic problem of the propagation of Rayleigh waves in a homogeneous half-space with free-surface boundary conditions: (a) problem configuration. (b) dispersion plot.

wave propagating in the positive x diection, solutions to (4.4) may be written as:

$$\Phi(x, y, t) = f(y) e^{i(kx - \omega t)} \,, \tag{4.5a}$$

$$\Psi_z(x, y, t) = g(y) e^{i(kx - \omega t)} \,. \tag{4.5b}$$

Substituting (4.5) in (4.4) yields ordinary differential equations for the functions f and g. Solving these gives:

$$f(y) = Ae^{\kappa_\alpha y} + Ce^{-\kappa_\alpha y}\,, \tag{4.6a}$$

$$g(y) = Be^{\kappa_\beta y} + De^{-\kappa_\beta y}\,. \tag{4.6b}$$

Here, $\kappa_\alpha = \sqrt{k^2 - (\omega/c_p)^2}$ and $\kappa_\beta = \sqrt{k^2 - (\omega/c_s)^2}$.

We note that for surface wave solutions to exist, both $k^2 - (\omega/c_p)^2$ and $k^2 - (\omega/c_s)^2$ must be positive (otherwise the solutions will be oscillatory in y, which is a property characteristic of bulk waves not surface waves). This constraint trasnlates to requiring that $\frac{\omega}{k}$, i.e. the Rayleigh wave speed, be less than both c_p and c_s. We also note that the second term on the RHS of (4.6) indicates waves that grow in amplitude with depth, which is unphysical. Therefore, C and D must be set to zero. The final solutions for the potentials, therefore, may be written as:

$$\Phi(x, y, t) = Ae^{-\kappa_\alpha y + i(kx - \omega t)}\,, \tag{4.7a}$$

$$\Psi_z(x, y, t) = Be^{-\kappa_\beta y + i(kx - \omega t)}\,. \tag{4.7b}$$

Here, we include the expressions for the stress components in terms of A and B for future reference.

$$\tau_{xy} = -2i\mu k\kappa_\alpha Ae^{-\kappa_\alpha y + i(kx-\omega t)} + \mu(k^2 + \kappa_\beta^2)Be^{-\kappa_\beta y + i(kx-\omega t)}\,, \tag{4.8a}$$

$$\begin{aligned}\sigma_{yy} = &\left[(\lambda + 2\mu)(\kappa_\alpha^2 - k^2) + 2\mu k^2\right] Ae^{-\kappa_\alpha y + i(kx-\omega t)} \\ &+ 2i\mu k\kappa_\beta Be^{-\kappa_\beta y + i(kx-\omega t)}\end{aligned} \tag{4.8b}$$

In order to obtain the dispersion relation, we need to impose the boundary conditions $\tau_{xy}(x, 0, t) = 0$ and $\sigma_{yy}(x, 0, t) = 0$ next.

$$\tau_{xy}|_{y=0} = \left[\mu\left(\frac{\partial v}{\partial x} + \frac{\partial u}{\partial y}\right)\right]_{y=0} = 0\,, \tag{4.9a}$$

$$\sigma_{yy}|_{y=0} = \left[(\lambda + 2\mu)\frac{\partial v}{\partial y} + \lambda\frac{\partial u}{\partial x}\right]_{y=0} = 0\,. \tag{4.9b}$$

Knowing that $u = \frac{\partial \Phi}{\partial x} + \frac{\partial \Psi_z}{\partial y}$ and $v = \frac{\partial \Phi}{\partial y} - \frac{\partial \Psi_z}{\partial x}$ and rewriting the Lamé constants in terms of c_p and

c_s, the above equations can be written in terms of the unknowns A and B:

$$2ik\kappa_\alpha A - (k^2 + \kappa_\beta^2)B = 0\,, \tag{4.10a}$$

$$\left[(c_p^2 - 2c_s^2)k^2 - c_p^2\kappa_\alpha^2\right] A - 2ic_s^2 k\kappa_\beta B = 0\,. \tag{4.10b}$$

In matrix form,

$$\begin{bmatrix} 2ik\kappa_\alpha & -(k^2+\kappa_\beta^2) \\ k^2+k_\beta^2 & 2ik\kappa_\beta \end{bmatrix} \begin{Bmatrix} A \\ B \end{Bmatrix} = 0 \tag{4.11}$$

For nontrivial solutions to exist, we require the determinant of the coefficient matrix to be zero. This would give the dispersion relation.

$$\left[2 - \frac{\omega^2}{k^2 c_s^2}\right]^2 - 4\sqrt{1 - \frac{\omega^2}{k^2 c_p^2}}\sqrt{1 - \frac{\omega^2}{k^2 c_s^2}} = 0 \tag{4.12}$$

Figure 2 shows the dispersion relation plotted for a soil with density $\rho = 1600$ kg/m^3, longitudinal wave speed $c_p = 468$ m/s and shear wave speed $c_s = 250$ m/s [18]. The black dots are solutions obtained from solving the eigenvalue problem presented above. The slope of the green line indicates the shear wave speed, c_s. The slope of the red dashed line indicates the Rayleigh wave speed reported in [18] (232m/s). The results agree well as expected.

4.3 Homogeneous half-space with linear resonators

The configuration of the problem is shown in Fig. 4.3a. In the limit of long wavelengths (in comparison to the spacing between resonators and resonator dimensions), the problem could be treated as one with uniform normal stress boundary conditions at the surface. Therefore, the derivation from the previous section holds up to Equation (4.7).

Considering an effective medium approach [125], the equation of motion for a single oscillator can be written as:

$$m\ddot{w}_r + k_1 w_r = -m\ddot{v}_{y,0} \tag{4.13}$$

where, w_r is the relative displacement of the oscillator and $v_{y,0}$ indicates the displacement of the substrate at the surface $y = 0$. We assume a traveling wave solution for the oscillator of the form

$w_r = W_r e^{i(kx-\omega t)}$. Considering $v_{y,0} = V_0 e^{i(kx-\omega t)}$ and substituting in 4.13 gives

$$W_r = -\frac{\omega^2}{\omega_r^2 - \omega^2} V_0 \tag{4.14}$$

Here, $\omega_r = \sqrt{k_1/m}$ is the resonance frequency of the oscillator and ω is the excitation frequency. Considering $v_{y,0} = V_0 e^{i(kx-\omega t)}$ and $f_s = F_s e^{i(kx-\omega t)}$, the spring force may then be written as

$$F_s = m\omega^2 \left(\frac{\omega_r^2}{\omega_r^2 - \omega^2} \right) V_0 \tag{4.15}$$

Therefore, the uniform stress $\sigma_{yy}(x, 0, t) = -f_s/a = \sigma_0 V_0$, where a is the tributary area of each resonator and the negative sign accounts for the fact that the unit normal to surface is in the opposite direction of $+y$. Considering that $V_0 = -(\kappa_\alpha A + ikB)$, the counterpart of (4.11) may be written as

$$\begin{bmatrix} 2ik\kappa_\alpha & -(k^2 + \kappa_\beta^2) \\ (k^2 + k_\beta^2) + \frac{\sigma_0 \kappa_\alpha}{\mu} & 2ik\kappa_\beta + i\frac{\sigma_0 k}{\mu} \end{bmatrix} \begin{Bmatrix} A \\ B \end{Bmatrix} = 0 \tag{4.16}$$

Setting the determinant of the coefficient matrix to zero yields the following dispersion relation:

$$\left[2 - \frac{\omega^2}{k^2 c_s^2} \right]^2 - 4\sqrt{1 - \frac{\omega^2}{k^2 c_p^2}} \sqrt{1 - \frac{\omega^2}{k^2 c_s^2}} = \frac{-\sigma_0 \omega^2}{\rho c_s^4 k^3} \sqrt{1 - \frac{\omega^2}{k^2 c_p^2}} \tag{4.17}$$

Fig. 4.3b shows the dispersion plot for the exact same problem as the previous sections but with uniformly-distributed resonators of mass $m = 10500$ kg and stiffness $k_1 = 2.4416$ MN/m. The plot clearly shows that a band gap has opened starting at the resonance frequency of the resonators ($f_r = 2.43$ Hz). The figure also shows that the new hybrid Rayleigh waves have a speed c_{RH} that is slightly greater than the Rayleigh wave speed in the medium with free-surface boundary condition. The upper edge of the band gap is marked where the line of slope c_{RH} meets the curve corresponding to the shear wave. This is consistent with the fact that modes with velocities higher than c_s cannot exist as surface wave solutions. Therefore, the system has served as an effective means for filtering Rayleigh waves in a targeted frequency region.

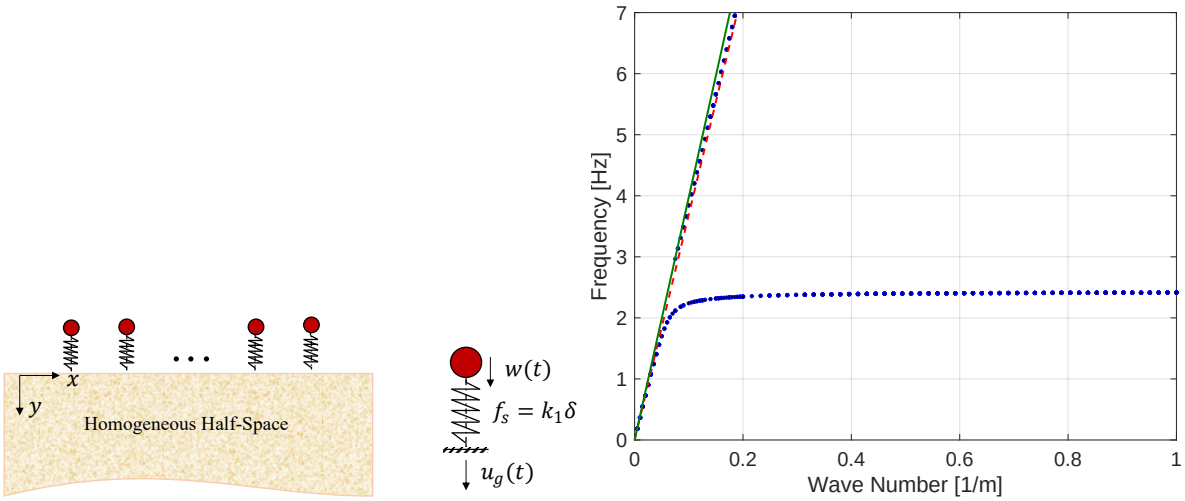

(a) (b)

Figure 4.3: Half-space with linear resonators at surface.: (a) problem configuration. (b) dispersion plot.

4.4 Homogeneous half-space with nonlinear Duffing resonators

In this section, we extend the analysis presented in the previous sections to the case where the oscillators have Duffing-type nonlinearity. Same as the previous section, we use an effective medium approach. In the presence of nonlinearities, higher harmonics may generate and waves can interact. Here, we only consider the effect of self-action on dispersion curves and do not consider wave-wave interactions, i.e. the wave is assumed to be isochromatic. We rewrite Equation (4.1) here fore reference.

$$(\lambda+2\mu)\frac{\partial^2 u}{\partial x^2}+(\lambda+\mu)\frac{\partial^2 v}{\partial x\partial y}+\mu\frac{\partial^2 u}{\partial y^2}=\rho\frac{\partial^2 u}{\partial t^2}\,, \tag{4.18a}$$

$$(\lambda+2\mu)\frac{\partial^2 v}{\partial y^2}+(\lambda+\mu)\frac{\partial^2 u}{\partial x\partial y}+\mu\frac{\partial^2 v}{\partial x^2}=\rho\frac{\partial^2 v}{\partial t^2}\,. \tag{4.18b}$$

subjected to the following boundary conditions:

$$\tau_{xy}|_{y=0}=\left[\mu\left(\frac{\partial v}{\partial x}+\frac{\partial u}{\partial y}\right)\right]_{y=0}=0\,, \tag{4.19a}$$

$$\sigma_{yy}|_{y=0}=\left[(\lambda+2\mu)\frac{\partial v}{\partial y}+\mu\frac{\partial u}{\partial x}\right]_{y=0}=\sigma\,. \tag{4.19b}$$

We introduce the potentials Φ, Ψ such that

$$u = \frac{\partial \Phi}{\partial x} + \frac{\partial \Psi}{\partial y}\,, \tag{4.20a}$$

$$v = \frac{\partial \Phi}{\partial y} - \frac{\partial \Psi}{\partial x}\,, \tag{4.20b}$$

so that Equation (4.18)may be rewritten as

$$\frac{\partial^2 \Phi}{\partial t^2} = c_p^2 \nabla^2 \Phi\,, \tag{4.21a}$$

$$\frac{\partial^2 \Psi}{\partial t^2} = c_s^2 \nabla^2 \Phi\,. \tag{4.21b}$$

Therefore, functions f and g may be written in the following form

$$\Phi = f(y) e^{\mathrm{i}(kx - \omega t)} + \mathrm{cc}\,, \tag{4.22}$$

$$\Psi = g(y) e^{\mathrm{i}(kx - \omega t)} + \mathrm{cc}\,, \tag{4.23}$$

where cc stands for complex-conjugate. Up to this point, everything has been handled in a similar manner to the linear case. Substituting Equation (4.22) in (4.21) gives

$$\Phi = A e^{-\kappa_\alpha y + \mathrm{i}(kx - \omega t)} + \mathrm{cc}\,, \tag{4.24a}$$

$$\Psi = B e^{-\kappa_\beta \mathrm{i}(kx - \omega t)} + \mathrm{cc}\,, \tag{4.24b}$$

We write the equation of motion for the oscillator as follows

$$m\ddot{w}_r + k_1 w_r + k_3 w_r^3 = -m\ddot{v}_{y,0} \tag{4.25}$$

where, k_1 and k_3 are the linear and nonlinear stiffness coefficients and $v_{y,0}$ indicates displacement of the substrate at surface $y = 0$. Using the effective medium approach, we assume a traveling wave solution for the oscillator of the form $w_r = W_r e^{i(kx - \omega t)} + \mathrm{cc}$. Thus,

$$\begin{aligned} f_s &= \mathrm{k}_1 \left[W_r e^{\mathrm{i}(kx - \omega t)} + \mathrm{cc} \right] + \mathrm{k}_3 \left[W_r e^{\mathrm{i}(kx - \omega t)} + \mathrm{cc} \right]^3 \\ &= W_r \left[\mathrm{k}_1 + 3\mathrm{k}_3 |W_r|^2 \right] e^{\mathrm{i}(kx - \omega t)} + \mathrm{cc} + H.H.T\,, \end{aligned} \tag{4.26}$$

where $H.H.T$ stands for "Higher Harmonic Terms", which are to be ignored. Similar to the previous section, σ may be written as f_s/a.

Hence, the equation of motion of the oscillator yields

$$-m\omega^2 W_r + \mathrm{k}_1 W_r + 3\mathrm{k}_3 |W_r|^2 W_r = m\omega^2 V_0 \,, \tag{4.27}$$

where, relating this to the displacement field in the continuum, $v|_{y=0} = V_0 e^{\mathrm{i}(kx-\omega t)} + \mathrm{cc}$. On the other hand, from the continuum viewpoint:

$$V_0 = -\kappa_\alpha A - \mathrm{i}kB \,, \tag{4.28}$$

hence,

$$(-m\omega^2 + \mathrm{k}_1 + 3\mathrm{k}_3 |W_r|^2) W_r = m\omega^2 V_0 \tag{4.29}$$

and,

$$\begin{aligned} W_r &= \frac{m\omega^2}{(-m\omega^2 + \mathrm{k}_1 + 3\mathrm{k}_3 |W_r|^2)} V_0 \\ &= \frac{\omega^2}{(-\omega^2 + \omega_r^2 (1 + 3\alpha |W_r|^2))} V_0 \end{aligned} \tag{4.30}$$

where, $\alpha = k_3/k_1$. Considering $f_s = F_s e^{i(kx-\omega t)}$, the magnitude of the spring force F_s can be written as follows:

$$F_s = m\omega^2 \left[\frac{\omega_r^2 (1 + 3\alpha |W_r|^2)}{\omega_r^2 (1 + 3\alpha |W_r|^2) - \omega^2} \right] V_0 \tag{4.31}$$

Setting α equal to zero gives the expression derived for the linear case. The term $3\alpha |W_r|^2$ is a first order correction to the linear case, accounting for the nonlinear force-displacement relationship of the spring.

The uniform stress $\sigma_{yy}(x, 0, t) = -f_s/a = \sigma_0 V_0$, where a is the tributary area of each resonator and the negative sign accounts for the fact that the unit normal to surface is in the opposite direction of $+y$. Furthermore, it should be noted that the uniform stress is now amplitude-dependent, which means that the amplitude of the motion affects the overall behavior of the system. This is characteristic of nonlinear systems in general.

Now, we impose the boundary conditions. For the shear stress we have

$$-2\mathrm{i}\kappa_\alpha k A + (\kappa_\beta + k^2) B = 0 \,, \tag{4.32}$$

and for the normal stress we get

$$[(\lambda + 2\mu)\kappa_\alpha^2 - \lambda k^2]A + 2\mathrm{i}\mu\kappa_\beta kB = \sigma_0(\kappa_\alpha A + ikB)\,, \tag{4.33}$$

The dispersion relation may be obtained similar to the previous section using Equation (4.17) by replacing the definition of σ_0 with the new amplitude-dependent one.

Figures 4.4c and 4.4d show sample dispersion plots for $\alpha = 0.25$ (hardening) and $\alpha = -0.25$ (softening). In both cases, $|W_r|$ is set to unity. All other problem parameters are the same as previous sections. The figure shows that nonlinearity can shift the band gap location to lower/higher frequencies in the case of softening/hardening nonlinearity.

4.5 Discussion and conclusions

In this chapter, we presented a theoretical framework for obtaining the dispersion relation of a half-space with a periodic array of Duffing resonators on its surface using the harmonic balance method, and showed that nonlinear local resonances lead to amplitude-dependent dispersion for Rayleigh waves. The derivation is based on two fundamental assumptions:

- the wavelength of propagating waves is much larger than the characteristic lengths of the problem, such as resonator dimensions and the periodicity length. This ensures the validity of using an effective medium approach.

- free-propagating waves in the system are mono-chromatic. This neglects the generation of higher harmonics in the system, and accounts only for nonlinear self-action, by which a wave self-adjusts its frequency.

Our findings show that the shift in dispersion branches and consequently band gap locations are closely tied to nonlinear local resonance shifts. That is, for hardening resonators whose resonance frequency increases with an increase in the steady-state amplitude, dispersion branches shift to higher frequencies for larger amplitudes. The reverse is true when nonlinearity is softening. Increasing the nonlinearity coefficient has a similar effect to that of the amplitude as well. On another note, for hardening (softening) resonators, the band gap width increases (decreases) with an increase in amplitude.

We note that these are preliminary analytical results which should be verified using numerical simula-

tions. There are challenges associated with this. For example, radiation damping in such simulations could contribute to energy loss which will affect the nonlinear resonance frequency shift of the oscillators.

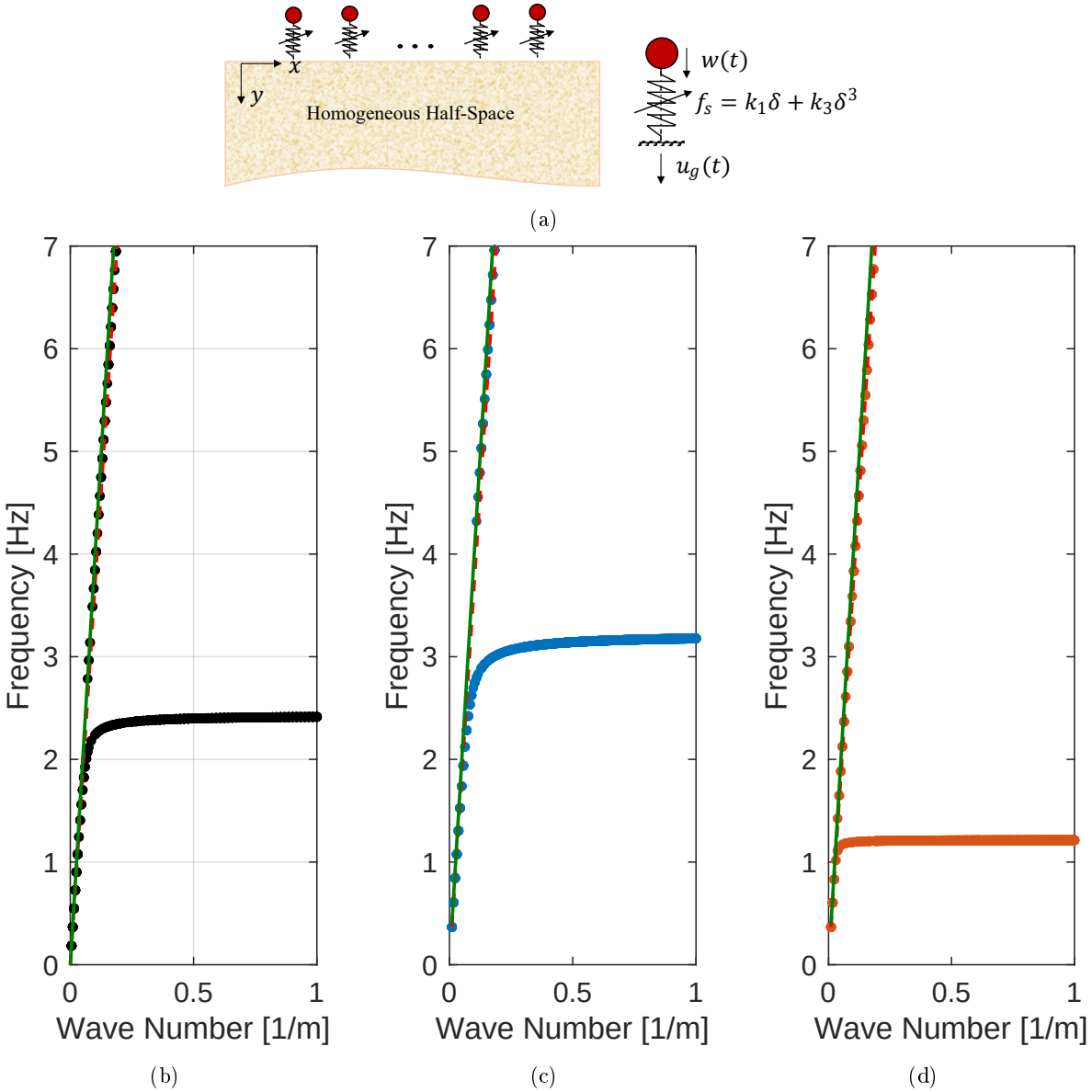

Figure 4.4: Dispersion curves for (a) half-space with an array of linear resonators, (b) half-space with an array hardening Duffing oscillators with $\alpha = 0.25$, and (c) half-space with an array softening Duffing oscillators with $\alpha = -0.25$.

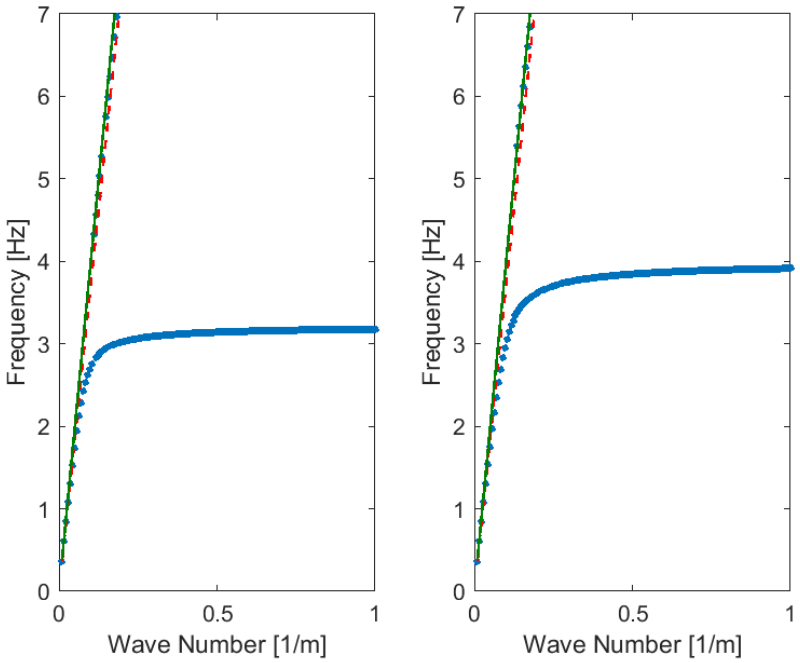

Figure 4.5: Amplitude-dependent dispersion for Rayleigh waves. Dispersion curves for the half-space with an array of hardening Duffing oscillators with $\alpha = 0.25$ and $|W_r| = 1$ (left panel) and $|W_r| = 1.5$ (right panel).

Chapter 5

Experimental evidence of amplitude-dependent dispersion for surface acoustic waves

5.1 Introduction

Controlling surface acoustic waves has broad applications in science and engineering. At the micro and nano scales, these waves are of interest in the design of radiofrequency filters for wireless telecommunication systems [126, 35] as well as biosensors for medical diagnostics [127]. At larger scales, the study of these waves is essential for protecting the built environment from the damaging effects of seismic waves [120, 128, 26]. The advent of metamaterials has realized unique engineering solutions for manipulating these waves over broad frequency spectrums. For example, phononic crystals in the form of architectured surface layers have been used to design SAW filters, space-saving reflective gratings and waveguides [129, 130]. Periodic arrangement of local resonators has also been used to achieve subwavelength wave filtering and waveguiding [131, 132] as well as high-resolution imaging [133, 37].

Once fabricated, metamaterials for SAW control are only bound to operate at a specific frequency range. Recently, preliminary efforts have been undertaken to increase the versatility of these systems by making their response tunable [134, 135], or even non-reciprocal [136]. Most previous work on SAW tunability has focused on using external stimuli, such as thermal, magnetic and electrical fields for tuning the wave-control capabilities of these systems [134, 135, 137]. On the other hand, the design of self-tunable SAW devices, which can *passively adapt* to the loading conditions without the need for external tuning stimuli, has not received much attention. Incorporating nonlinearity in the design of metamaterials will provide an opportunity to explore amplitude-dependent tuning.

Nonlinear metamaterials offer enhanced control over wave transmission compared to their linear counterparts. Several exotic features have already been demonstrated in these systems, including self-tunability [53, 138], nonreciprocity [60, 139, 140, 141, 59], energy tunneling and localization [142, 143] and, more recently, the emergence of subharmonic bandgaps [67, 68]. Theoretical frameworks have been developed for determining the dispersive properties of nonlinear phononic lattices/crystals

[144, 145, 146, 147], and nonlinear elastic continua with linear local resonators [148]. The effects of nonlinear local resonators, on the other hand, have been mostly studied in the context of discrete systems [149, 150, 151]. Limited works exist on wave propagation in systems consisting of an array of nonlinear resonators embedded in linear elastic continua [61]. A notable exception is represented by works on the interaction of SAWs with contact-based resonators [125, 152, 153, 154]. It must be noted, however, that these studies are based on the assumption that the amplitude of the propagating waves is small and that the nonlinear stiffness can be linearized.

Amplitude-dependent resonance is a well-documented phenomenon in nonlinear dynamics [155]. Several works have documented this effect for Hertzian contact resonators [156, 157]. A notable study on a cylindrical rod in contact with a bead provides experimental proof that the nonlinear properties of the contact lead to amplitude-dependent resonance shifts [158]. A notable experimental work had previously demonstrated how resonance shifts in a one-dimensional chain of beads connected with nonlinear springs are intimately related to shifts in dispersion curves for the overall system [159]. In a most recent study, nonlinearity-induced resonance frequency tuning was achieved in a nanostrip phononic metasurface (NPM) through the power-dependent coupling of adjacent nanostrips [160]. However, experimental investigations of nonlinear dispersion shifts for SAWs have largely remained unexplored.

In this work, we leverage the experimental setup in [135] and exploit the nonlinear dynamics of an array of contact resonators to achieve amplitude-dependent dispersive properties for plate edge waves. Our table-top experimental setup consists of a thin plate decorated with an array of bead-magnet resonators along its edge. We exploit the similarity between dispersion properties of edge waves in plates and surface waves propagating in a semi-infinite medium [161, 162] to demonstrate how nonlinear resonant inclusions may be used to achieve amplitude-dependent dispersive properties for SAWs. These findings may inform the design of passive-adaptive metamaterials for controlling surface acoustic waves at different scales. Among other applications, these findings are bound to be particularly consequential in the context of seismic wave attenuation; in fact, the large wave amplitude associated with seismic events are bound to excite the nonlinear characteristics of any metamaterial-inspired barrier.

The chapter is organized as follows: in section 5.2, we describe the main experimental setup and its constituents. In section 5.3, we unravel the physics behind the interaction of SAWs with nonlinear bead-magnet resonators in three stages: first, we study the nonlinear dynamics of a single bead-magnet resonator on a rigid substrate theoretically and experimentally; then we focus our attention on the nonlinear resonance properties of a single bead-magnet resonator on a compliant substrate. We will

provide experimental evidence of higher harmonic generation as well as a more well-rounded numerical study on the nonlinear properties of the contact resonators. In the last part of this section, we provide numerical and experimental proof of amplitude-dependent dispersion for SAWs by closely studying the behavior of the overall experimental setup as well as the resonators in the linear and nonlinear regimes. We conclude by discussing the findings, and limitations of the current approach, and we make recommendations for the betterment of future studies.

5.2 A compact experimental setup

The theoretical predictions from the previous section suggest that using nonlinear resonators may be an effective way to achieve amplitude-dependent dispersion for surface waves. In this section, we leverage the experimental setup in [135] and exploit the inherent nonlinear properties of contact resonances to achieve amplitude-dependent dispersive properties for plate edge waves. Our compact table-top experimental setup is shown in Figure 5.2. It consists of an acrylic plate of dimensions $608 \times 912 \times 8$ mm ($H \times W \times t$), Young's modulus $E = 5.5$ GPa, Poisson ratio $\nu = 0.35$, and density $\rho = 1190$ kg m^{-3}. The plate is clamped to an optical table at the bottom along the longer edge. A set of 41 disk magnets (K&J magnetics DH101; NdFeB, Grade N42) are glued at equal distances of $d = 15$ mm on its top edge. The magnets have a diameter of $D_m = 2.5$ mm and a thickness of $t_m = 0.8$ mm. Steel beads (McMaster-Carr 9642K49) with radius $r_b = 4.8$ mm and mass $m_b = 3.5$ g are placed on top of each magnet. The bead-magnet assemblies will serve as nonlinear mechanical oscillators. A vibration exciter (HBK Type 4810) is glued to the plate at a distance of $l_s = 168$ mm from the first bead. A signal generator (Agilent 33220A) and power amplifier (HBK Type 2718) are used to drive the shaker and excite vertically-polarized edge waves along the edge of the plate. A laser doppler vibrometer (LDV, Polytec OFV-5000) is mounted on a linear stage and a motor is used to measure the vertical velocity component at observation points consecutively. Two sets of observation points were chosen to record the response of the plate's edge as well as the resonators. The distance between adjacent observation points in each set is 15 mm. Measurement data is acquired using an oscilloscope (Tektronix DPO3034).

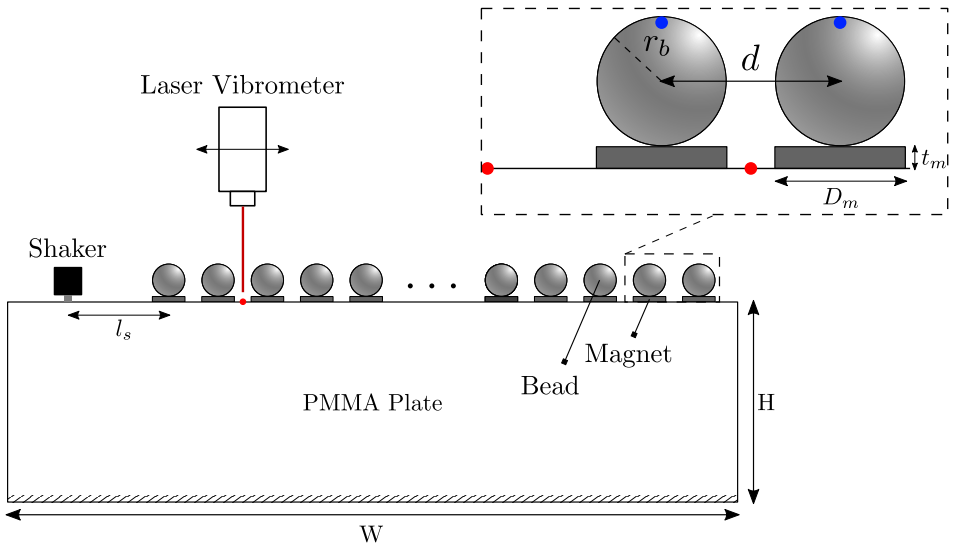

Figure 5.1: Schematics of the table-top experimental setup showing the dimensions of the elements as well as the location of observation points on plate's edge (red) and resonators (blue).

We use the analytical dispersion relation for thin semi-infinite plates with free stress boundary conditions [161, 162] to predict the phase velocity c_R of edge waves in a pristine plate:

$$\left(2-\frac{c_R^2}{c_T^2}\right)^2-4\sqrt{\left(1-\frac{c_R^2}{c_T^2}\right)\left(1-\frac{c_R^2}{v_P^2}\right)}=0 \tag{5.1}$$

where $v_p=\left[E/\rho(1-\nu^2)\right]^{1/2}$ is the velocity of dilational waves in a thin plate and $c_T=[E/2\rho(1+\nu)]^{1/2}$ is the shear wave speed. We note that this equation is similar to the one describing the dispersion relation of Rayleigh waves in a half-space (Equation (4.12)). Using this equation, we make a theoretical prediction of $c_R=1205\ \mathrm{m\,s^{-1}}$ for the phase velocity of edge waves propagating on a pristine plate.

In what follows, we first explain the theoretical and numerical frameworks used to study the system under consideration as well as its individual components. Next, we present the results and discuss them in detail.

5.3 SAW - nonlinear contact-resonance interaction

We start by studying the nonlinear dynamics of a single bead-magnet resonator on a rigid substrate analytically. After characterizing the bead-magnet as a spring-mass oscillator, we use ABAQUS to model the dynamics of a single bead-magnet as well as an array of bead-magnets on a thin plate. This theoretical/numerical framework will help us predict and interpret the experimental results.

5.3.1 Nonlinear Dynamics of a single resonator on a rigid substrate

Theroretical framework

The configuration is shown in Figure 5.2. We consider the bead as a rigid body of mass m_b. The contact between the bead and magnet may be modeled by using normal and shear springs [152, 135]. Here, we only consider normal contact resonance and neglect the resonance induced by the horizontal movement of the bead. We use the Hertzian contact law to determine the properties of the normal spring. Following Hertz's theory of contact [163], the contact force F_c between a sphere of radius r_b and a planar surface may be written as

$$F_c = \frac{4}{3} E^* r_b^{1/2} \delta^{3/2} \tag{5.2}$$

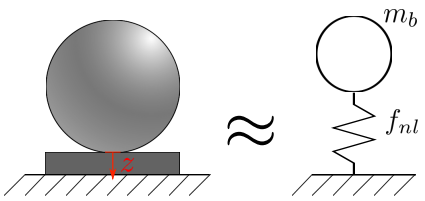

Figure 5.2: Idealization of the bead-magnet resonator as a nonlinear mass-spring oscillator.

where, $E^* = \left[(1-\nu_m^2)/E_m + (1-\nu_b^2)/E_b\right]^{-1}$. E_m and ν_m are the modulus and Poisson's ratio of the magnetic disk, respectively. Similarly, E_b and ν_b indicate the modulus and Poisson's ratio of the steel bead. δ is the relative normal contact displacement between the two surfaces in contact.

The equation of motion for the oscillator may be written as

$$m_b \ddot{z} + c\dot{z} + kz^{3/2} = F(t) + F_m \tag{5.3}$$

Here, c denotes the damping constant and $k = \frac{4}{3} E^* r_b^{1/2}$. We note that the variable z measures the displacement of the bead from the top face of the magnet. F_m is the magnetic force and $F(t)$ is the load applied directly to the bead. We assume loading to be harmonic and of the form $F(t) = F_0 \cos \omega t$.

Introducing the variable $q = \frac{3(z-\delta_s)}{2\delta_s}$, we rewrite the previous equation as follows

$$\frac{2}{3} m_b \delta_s \ddot{q} + \frac{2}{3} c\delta_s \dot{q} + k\delta_s^{3/2} \left[1 + \frac{2}{3} q\right]^{3/2} = F_0 \cos \omega t + F_m \quad , \quad q \leq -3/2 \tag{5.4}$$

The condition $q \leq -3/2$ guarantees that loss of contact does not occur. Dividing both sides by $\frac{2}{3}m_b\delta_s$ gives

$$\ddot{q} + \frac{c}{m_b}\dot{q} + \frac{3k}{2m_b}\delta_s^{1/2}\left[1 + \frac{2}{3}q\right]^{3/2} = \frac{3}{2m_b\delta_s}\left(F_0\cos\omega t + F_m\right) \tag{5.5}$$

We define $\Omega = \left[\frac{3k}{2m_b}\delta_s^{1/2}\right]^{1/2}$ and set $c = 2\mu m_b\Omega$. Ω is, in fact, the natural frequency of the oscillator and μ is the damping coefficient. We also introduce the non-dimensional time variable $\tau = \Omega t$. Rewriting the equation in terms of these new variables yields

$$\frac{d^2q}{d\tau^2} + 2\mu\frac{dq}{d\tau} + \left[1 + \frac{2}{3}q\right]^{3/2} = 1 + \frac{F_0}{F_m}\cos\frac{\omega}{\Omega}\tau \tag{5.6}$$

Now, we introduce the following dimensionless groups:

$$r = \frac{\omega}{\Omega} \quad , \quad \mu = \frac{c}{2m_b\Omega} \quad , \quad \kappa = \frac{F_0}{F_m} \tag{5.7}$$

Using Taylor series, we may expand the nonlinear term and rewrite the previous equation.

$$\frac{d^2q}{d\tau^2} + 2\mu\frac{dq}{d\tau} + q + \frac{1}{6}q^2 - \frac{1}{54}q^3 = \kappa\cos r\tau \tag{5.8}$$

For now, we consider the system to be undamped ($\mu = 0$). In this case, the only dimensionless groups governing the dynamics of the system are the parameters r and κ. In what follows, we briefly discuss the influence of these parameters on the dynamics.

κ shows the magnitude of excitation with respect to the magnetic force while r is a characteristic frequency of the problem that represents the ratio of inertial forces to the nonlinear elastic forces. Therefore, for $r \ll 1$, the problem is quasi-static while for $r \approx 1$ and $r \gg 1$, the problem must be treated as a standard or high-frequency dynamic system. This parameter increases as the excitation frequency and bead's mass increase. However, stiffening the contact or strengthening the magnet decreases this parameter.

It is well known that nonlinearity can lead to primary, subharmonic and superharmonic resonances based on the excitation intensity and frequency content. For now, we focus our attention to the case of "Primary Resonances". The equation needs to be rescaled such that the nonlinearity, damping and the forcing appear at the same scale. Note that this is intuitively consistent with the definition of a

primary resonance condition in which a small excitation leads to a large-amplitude response. We set:

$$q = \epsilon\hat{q} \quad , \quad \mu = \epsilon^2\hat{\mu} \quad , \quad \kappa = \epsilon^3\hat{\kappa} \tag{5.9}$$

Here, $\hat{q}$, $\hat{\mu}$ and $\hat{k}$ are all $\mathcal{O}(1)$ variables. We further assume that the energy source is ideal (the excited system has no effect on it). ϵ is a small-scale parameter that represents the order of the motion amplitude ($|\epsilon| \ll 1$). Without loss of generality, the equation of motion may be rewritten in the following form:

$$\frac{d^2\hat{q}}{d\tau^2} + 2\epsilon^2\hat{\mu}\frac{d\hat{q}}{d\tau} + \omega_0^2\hat{q} + \epsilon\alpha_2\hat{q}^2 + \epsilon^2\alpha_3\hat{q}^3 = \epsilon^2\hat{\kappa}\cos r\tau \tag{5.10}$$

For the specific problem at hand, $\omega_0 = 1$, $\alpha_2 = 1/6$ and $\alpha_3 = -1/54$. For studying primary resonances, we further assume that $r = \omega_0 + \epsilon^2\sigma$, where σ is the detuning parameter. The following variables representing slow and fast time scales are then introduced:

$$T_0 = \tau \quad , \quad T_1 = \epsilon\tau \quad , \quad T_2 = \epsilon^2\tau \tag{5.11}$$

A uniform expansion for $\hat{q}$ is considered as follows:

$$\hat{q}(T_0, T_1, T_2) = \hat{q}_0 + \epsilon\hat{q}_1 + \epsilon^2\hat{q}_2 + \mathcal{O}(\epsilon^3) \tag{5.12}$$

Substituting equations 5.11 and 5.12 in the equation of motion gives the following ordered set of equations:

$$\mathcal{O}(\epsilon^0) : D_0^2\hat{q}_0 + \omega_0^2\hat{q}_0 = 0 \tag{5.13a}$$

$$\mathcal{O}(\epsilon^1) : D_0^2\hat{q}_1 + \omega_0^2\hat{q}_1 = -2D_0D_1\hat{q}_0 - \alpha_2\hat{q}_0^2 \tag{5.13b}$$

$$\begin{aligned}\mathcal{O}(\epsilon^2) : D_0^2\hat{q}_2 + \omega_0^2\hat{q}_2 = &- \left(D_1^2 + 2D_0D_2 + 2\hat{\mu}D_0\right)\hat{q}_0 \\ &- 2D_0D_1\hat{q}_1 - 2\alpha_2\hat{q}_0\hat{q}_1 \\ &- \alpha_3\hat{q}_0^3 + \hat{\kappa}\cos\left(\omega_0T_0 + \sigma T_2\right)\end{aligned} \tag{5.13c}$$

where, $D_i = d/dT_i$. Solving the zeroth order equation yields

$$\hat{q}_0(T_0, T_1, T_2) = A(T_1, T_2)e^{i\omega_0T_0} + c.c. \tag{5.14}$$

Here, A is a complex function of the fast time scale variables and $c.c.$ indicates complex-conjugate.

Using this equation, equation (5.13b) may be rewritten as

$$\begin{aligned} D_0^2\hat{q}_1 + \omega_0^2\hat{q}_1 = &-2i\omega_0 D T_1 A e^{i\omega_0 T_0} \\ &- \alpha_2\left[A^2 e^{2i\omega_0 T_0} + |A|^2\right] + c.c. \end{aligned} \tag{5.15}$$

The only secular term on the right hand side is DT_1A. Setting this term to zero gives $A = A(T_2)$, which means the amplitude A is independent of the time scale T_1. Thus, equation (5.15) may be rewritten as

$$D_0^2\hat{q}_1 + \omega_0^2\hat{q}_1 = -\alpha_2\left[A^2 e^{2i\omega_0 T_0} + 2|A|^2 + \bar{A}^2 e^{-2i\omega_0 T_0}\right] \tag{5.16}$$

Here, $(\bar{.})$ indicates complex-conjugate. Solving this equation gives the solution for $\hat{q}_1$.

$$\hat{q}_1 = \frac{\alpha_2}{\omega_0^2}\left[\frac{1}{3}A^2 e^{2i\omega_0 T_0} + \frac{1}{3}\bar{A}^2 e^{-2i\omega_0 T_0} - 2|A|^2\right] \tag{5.17}$$

A similar procedure may be repeated for equation (5.13c). Setting the secular terms on the right hand side to zero would give

$$\begin{aligned} 2i\omega_0 D T_2 A = &-2i\omega_0\hat{\mu}A - 2\left(\frac{\alpha_2}{\omega_0}\right)^2\left[-2|A|^2 A + \frac{1}{3}|A|^2 A\right] \\ &- 3\alpha_3|A|^3 + \frac{1}{2}\hat{\kappa}e^{i\sigma T_2} \end{aligned} \tag{5.18}$$

Substituting the polar representation of $A = \frac{1}{2}a(T_2)e^{i\beta(T_2)}$ in the above equation gives the so-called modulation equations for a and β.

$$\omega_0 a' = -\omega_0\hat{\mu}a - \frac{1}{2}\hat{\kappa}\sin(\sigma T_2 - \beta) \tag{5.19a}$$

$$-a\beta'\omega_0 = \frac{1}{2}\hat{\kappa}\cos(\sigma T_2 - \beta) - \frac{1}{8}a^3\left[3\alpha_3 - \frac{10}{3}\left(\frac{\alpha_2}{\omega_0}\right)^2\right] \tag{5.19b}$$

Here, a and β are real variables denoting the amplitude and phase, respectively. Furthermore, $(.)'$ denotes differentiation with respect to the variable T_2. We introduce $\gamma = \sigma T_2 - \beta$. The autonomous counterpart of the above may be written as

$$a' = -\hat{\mu}a + \frac{\hat{\kappa}}{2\omega_0}\sin\gamma \tag{5.20a}$$

$$a\gamma' = a\sigma - \frac{9\alpha_3\omega_0^2 - 10\alpha_2^2}{24\omega_0^3}a^3 + \frac{\hat{\kappa}}{2\omega_0}\cos\gamma \tag{5.20b}$$

These equations give information about the evolution of the solution to steady-state and may be used to identify the domains of attraction. The frequency response function may be found by considering the steady-state solution ($a' = 0$ and $\gamma' = 0$):

$$a^2 \left\{ \hat{\mu}^2 + \left[\sigma - \frac{9\alpha_3\omega_0^2 - 10\alpha_2^2}{24\omega_0^3} a^2 \right]^2 \right\} = \frac{\hat{\kappa}^2}{4\omega_0^2} \tag{5.21}$$

Furthermore, for steady-state response, to the second order approximation we have

$$\hat{q} = a\cos(r\tau - \gamma) + \frac{1}{2}\epsilon\frac{\alpha_2 a^2}{\omega_0^2}\left[-1 + \frac{1}{3}\cos(2r\tau - 2\gamma)\right] + \mathcal{O}(\epsilon^{\in}) \tag{5.22}$$

The frequency-response function given by equation (5.21) is similar to that of a Duffing oscillator with a nonlinear coefficient $\alpha = \alpha_3 - \frac{10\alpha_2^2}{9\omega_0^2}$. For the specific problem at hand, $\alpha_3 = -1/54$ and $\alpha_2 = 1/6$. Therefore, $\alpha < 0$. Thus, the nonlinearity has a softening effect and bends the frequency-response curves to lower frequencies.

Experimental framework

To test the nonlinear resonance characteristics of the bead-magnet assembly, we attach the disk magnet to the surface of a piezoelectric transducer (Panametrics-NDT V1011) using an all-purpose Krazy glue. Once the glue has set, we place the bead on top of the magnet (see Figure 5.3b). Due to the importance of the contact surface in these experiments, we thoroughly clean the surface of the magnet as well as the steel bead before they get in contact. A Stanford SR 860 analyzer is used for the excitation in a sine sweep mode from five to eight kHz. We start at an amplitude of 8 mV and repeat the test by increasing the excitation amplitude at 8 mV intervals. Figure 5.3d shows the frequency-response plots of the bead-magnet resonator. The black and red curves show results for sweep-up and sweep-down tests, respectively.

At low excitation amplitudes, the bead-magnet assembly is expected to behave as a linear oscillator. Thus, the frequency-response curves from up and down sweeps coincide. The underlying linear natural frequency of the oscillator is approximately 7 kHz. The quality factor Q and damping ratio μ of the linear resonator may be determined using the half-power method.

$$Q = \frac{f_r}{f_2 - f_1} \tag{5.23a}$$

$$\mu \approx \frac{1}{2Q} \tag{5.23b}$$

where f_r is the natural frequency and $f_{1,2}$ are frequencies corresponding to half-power points (Figure 5.3c). Using equation (5.23), we determine a quality factor and damping ratio of approximately 35 and 0.014, respectively.

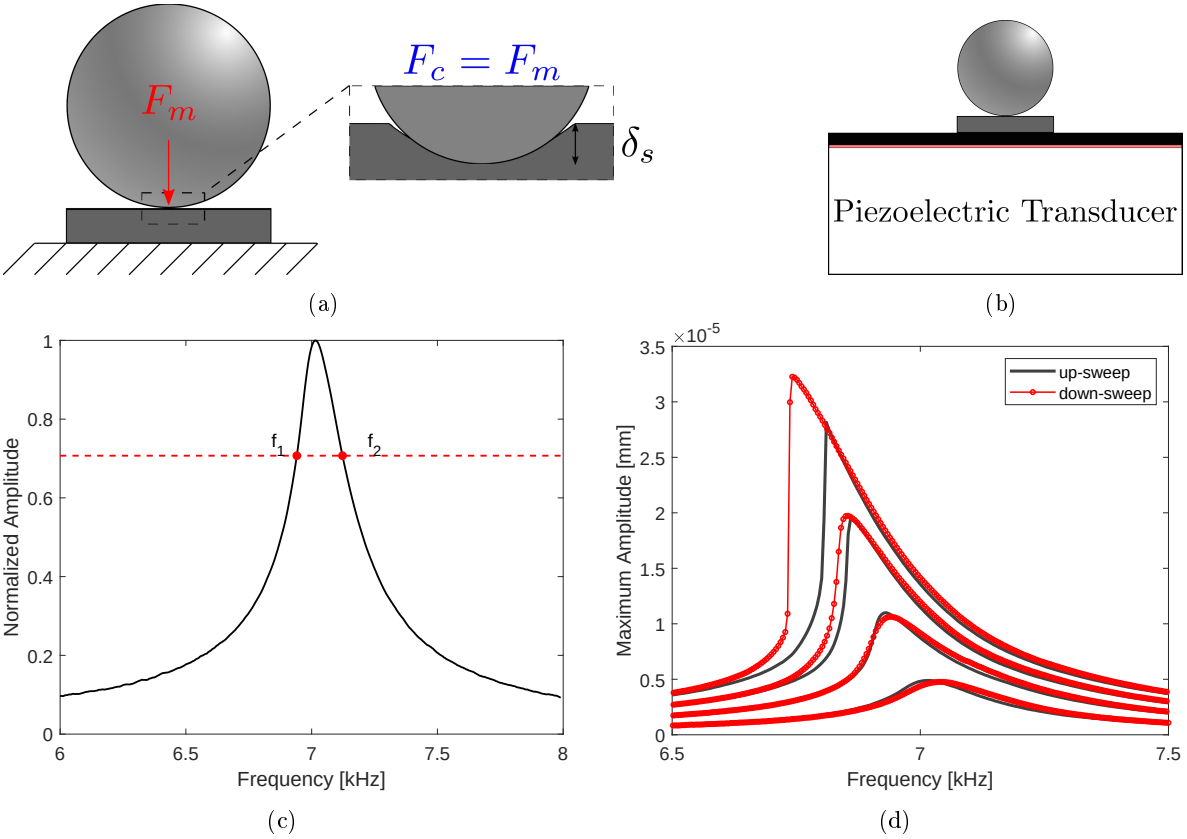

Figure 5.3: Single bead-magnet assembly on a rigid substrate. (a) Schematics of problem and the forces exerted on the bead. The insert shows the static overlap δ_s between the surfaces in contact at rest. F_c is the contact force. (b) Schematics of the experimental setup. (c) Normalized frequency-response curve of the bead-magnet oscillator at 8 mV. (d) Up-sweep (black) and down-sweep (red) frequency-response functions for the bead-magnet resonator at 8 mV-interval excitation amplitudes.

As the excitation amplitude is increased, nonlinearity bends the frequency-response away from the linear curve and shifts the locus of the peak amplitude to lower frequencies. This is consistent with the softening nonlinear response predicted in the previous section. Emergence of jumps in the frequency-response at an excitation amplitude of 32 mV is another indication of the inherent nonlinear properties of contact resonance.

It should be noted the analytical model presented in the previous section underestimates resonance frequency shifts observed in experimental results. This is due to the inadequacy of the Hertzian model in capturing the true nature of the contact. Merkel et al. studied various contact models - classical

Hertzian, JKR model with adhesion, a model including the roughness of the surfaces in contact, and a viscoelastic contact model - for modeling the nonlinear frequency-response of a bead in contact with an elastic rod. The results of their study reveals that the first three models are unable to capture the experimental behavior. They further show using the viscoelastic model can reproduce either the measured quality factor or the nonlinear resonance frequency shifts, but not both at the same time [158]. Here, we suffice to compare the theoretical and experimental results qualitatively; establishing that both show evidence of softening nonlinearity. Further studies on the dissipative nature of granular contact is required to capture the true behavior of the bead-magnet resonator.

5.3.2 Nonlinear dynamics of a single resonator on a compliant substrate

In the previous section, we showed that the bead-magnet assembly behaves as a nonlinear oscillator for sufficiently large excitation amplitudes. Here, we study the dynamics of a single bead-magnet oscillator on an acrylic plate. We present experimental evidence of higher harmonic generation and resonance frequency shifts in the contact resonator's response, and verify our experimental findings using numerical simulations.

The schematic of the experimental setup is similar to the one shown in Figure 5.2 with the difference that all bead-magnet resonators except the one closest to the shaker are removed. Linear resonance frequency of the oscillator is identified at roughly 5.3 kHz using a broadband excitation. This shows a shift of approximately 1.8 kHz in comparison to experimental results from the previous section. This resonance frequency shift can be attributed to substrate's compliance and its coupling to the rigid contact dynamics. Similar effect has been reported in previous work [135]. Based on the determined resonance frequency in the linear regime, we use a narrow-band slow (200 $\mathrm{Hz\,s^{-1}}$) sweep-down excitation from 6 kHz to 4 kHz to characterize the nonlinear response of the oscillator. Three different excitation amplitudes (10, 20, and 30 dB) were chosen by changing the gain on Brüel and Kjær amplifier.

Additionally, we resort to Finite Element simulations in ABAQUS [164] to model the problem and compare results with experiments. In order to do so, a 2D plane stress framework is used to model the Acrylic plate with material properties listed in section 5.2. The contact resonator is modeled using point masses along with nonlinear spring elements (see Figure 5.4). The springs only operate in the y

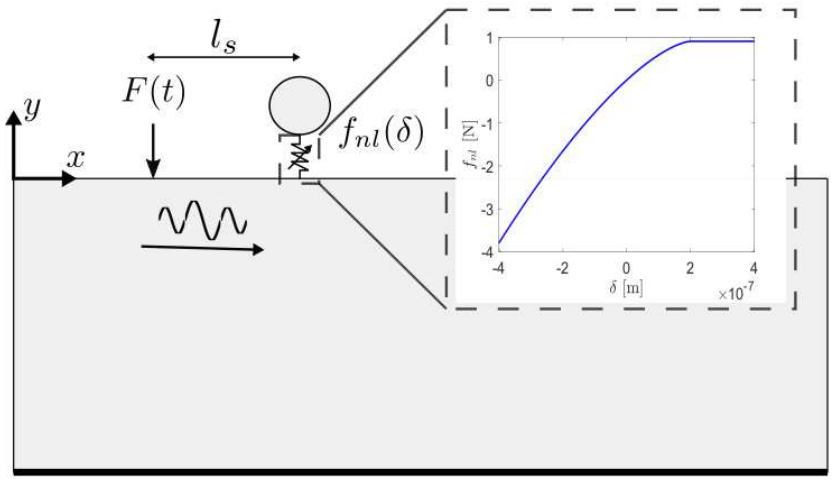

Figure 5.4: Schematic of the single bead-magnet resonator on plate in the ABAQUS models. The insert shows the nonlinear spring's force-displacement relationship.

direction. In order to model the nonlinear spring force f_{nl}, we use

$$f_{nl}(\delta) = -k(\delta_s - \delta)^{3/2}\mathcal{H} < \delta_s - \delta > + F_m \tag{5.24}$$

where $k = 4/3E^* r_b^{1/2}$ as before, δ is the change in spring's length (positive in tension and negative in compression) and $\mathcal{H}$ is the Heaviside function. The insert in Figure 5.4 shows the force-displacement relationship implemented in ABAQUS models. The shaker is modeled as a point force acting on the plate's edge. The force $F(t)$ is the same narrow-band slow (200 Hz s^{-1}) sweep-down excitation from 6 kHz to 4 kHz used in experiments. ABAQUS Explicit is used to carry out time-domain simulations. The amplitude of this force has been chosen such that the bead's maximum velocity is similar in the experimental and numerical setups. A fixed time step of 0.1 µs is used to guarantee stability. The plate is meshed with an approximate global size of 5 mm using free, advancing front algorithm. Linear quad-dominated plane-stress elements are used. We note that this average element size is sufficiently small to capture the smallest wavelength propagating in the system $\lambda_{min} = c_R/f_{max}$. Fixed boundary conditions are imposed along the plate's bottom edge. Furthermore, the point mass's motion is restricted such that it can only move in the y direction. We need to introduce a form of damping mechanism in the model to create a realistic situation in which an approximately steady-state response can be achieved, similar to the experimental setup. Due to lack of information on the damping properties of the plate as well as the uncertainties associated with the damping properties of the contact (see Section 5.3.1), we use a linear bulk viscosity parameter of 1.2 in ABAQUS to introduce artificial damping in the model. Bulk viscosity introduces damping associated with volumetric straining and

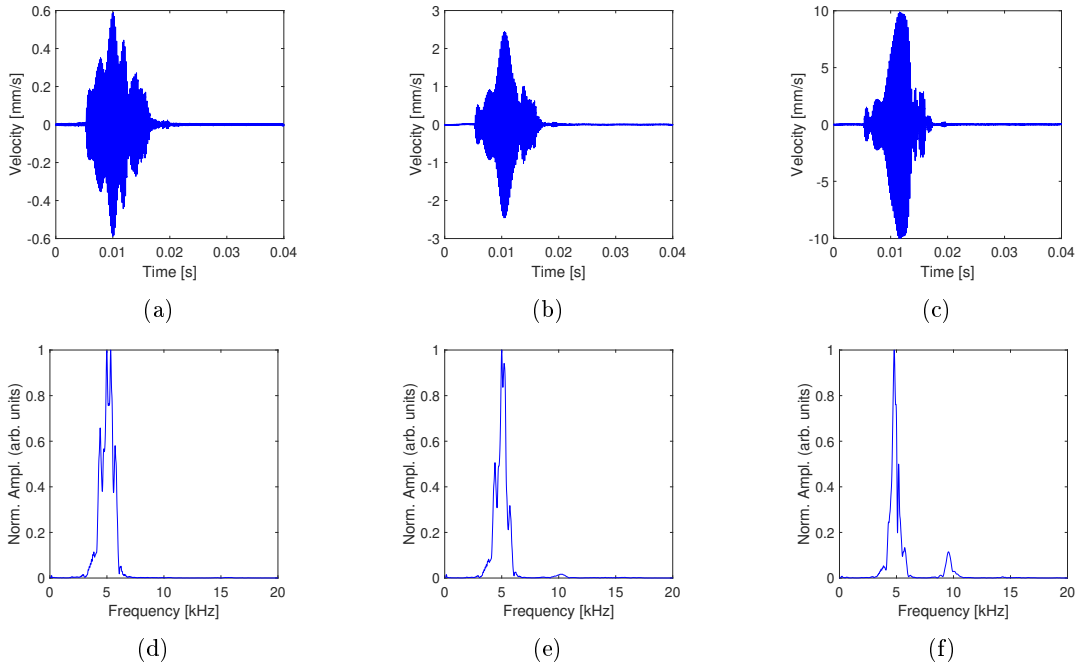

Figure 5.5: Experimental results for the single bead-magnet resonator on plate at increasing gain from left (10 dB) to right (30 dB): time history of the bead-magnet resonator (a)-(c); frequency spectrum of the response (d)-(f).

is purely a numerical effect. Consequently, it does not affect the material's constitutive model. Due to the existing discrepancies between damping properties of the experimental setup and that of the numerical simulation, we do not expect to have a one-on-one correspondence between results. Instead, we compare the experimental and numerical results qualitatively, that is: we seek to show that the resonator's response in both has indications of nonlinear resonance.

Figure 5.5 shows the time history as well as frequency spectrum for the bead's response at 10, 20 and 30 dB gains, from left to right, respectively. A few observations can be made. First, we note that the excitation's frequency range includes multiple resonance frequencies of the overall system and does not sweep over the resonance frequency of the oscillator in an isolated manner. Since the contact resonator response is coupled to that of the acrylic substrate, we observe multiple peaks in the oscillator's frequency spectrum at all levels of gain. Second, increasing the excitation amplitude leads to the generation of higher harmonics at twice the resonance frequency. This is consistent with our theoretical prediction for the bead's nonlinear response in the previous section. Lastly, the resonance frequency of the oscillator shifts from 5.3 kHz to 4.8 kHz as gain is increased.

Another interesting feature can be observed in the results by comparing time history plots. At lower gains, the rise and fall of amplitude at resonance is symmetric in shape. However, at 30 dB, the

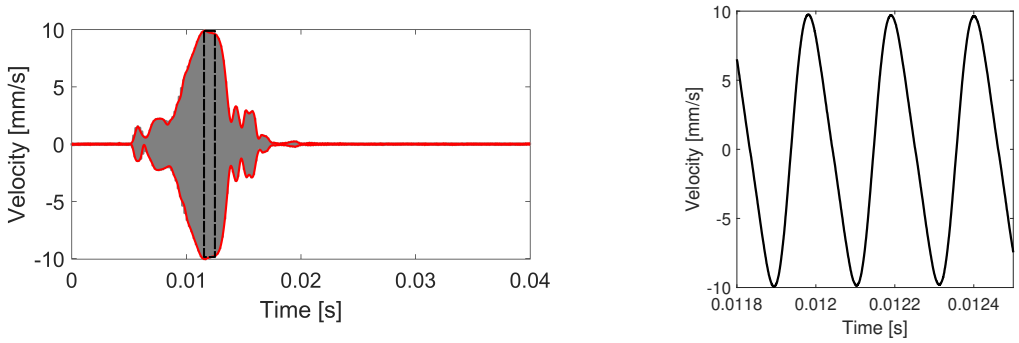

(a) (b)

Figure 5.6: Sweep down response of the contact resonator at 30 dB gain. The left panel shows the response of the bead as well as the response envelope. The right panel shows the monochromatic steady-state response right before loss of stability.

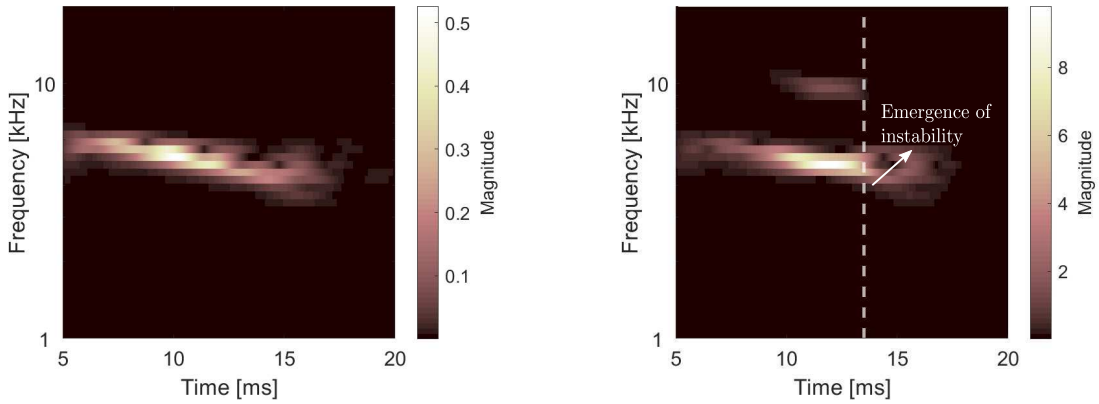

(a) (b)

Figure 5.7: Continuous wavelet transform of the bead's experimental response for (a) 10 dB and (b) 30 dB gain.

descent from resonance is abrupt, suggesting a plausible loss of stability common to nonlinear resonance phenomenon. In order to get a better understanding, we a take a closer look at the bead's dynamics at 30 dB gain. Figure 5.6a shows the time history plot at 30 dB. The red curve marks the response envelope. The amplitude and phase of the response prior to the onset of instability can be determined by looking at a time window where the response is monochromatic. This is shown in Figure 5.6b.

The emergence of instability and the so-called jump phenomenon is a definitive indication of the nonlinear nature of contact resonance. We analyze the response further in the time-frequency domain. Figure 5.6b shows the scalogram of the response using continuous wavelet transforms. Comparing the response at 10 and 30 dB clearly confirms the presence of second harmonics in the nonlinear regime. The onset of instability can be identified around 13 seconds in Figure 5.7b. Next, we present the

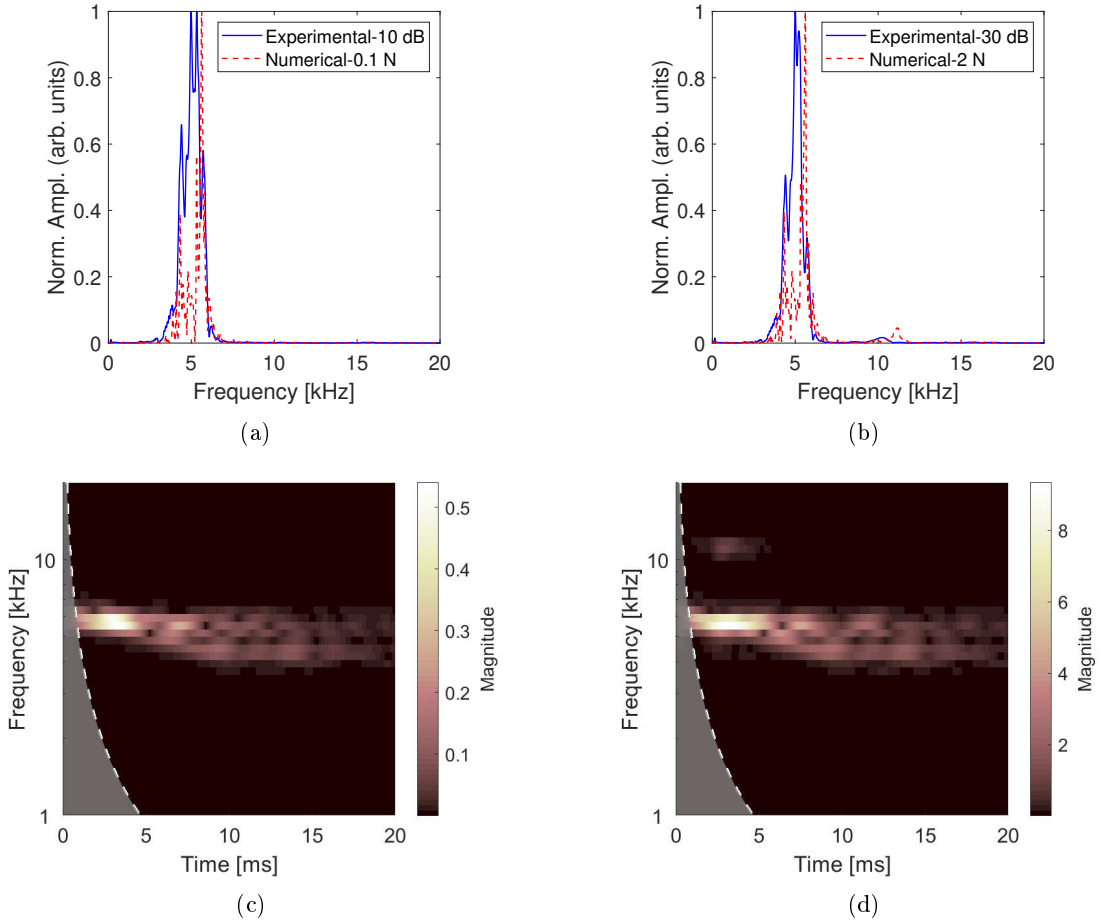

Figure 5.8: Numerical results for the bead's response: frequency spectrum at (a) 0.1 N and (b) 2 N forcing amplitudes; continuous wavelet transform of the response for (c) 0.1 N and (d) 2 N forcing amplitudes.

numerical results. As mentioned previously, the amplitude of force $F(t)$ has been chosen such that the bead's maximum velocity is similar in the experimental and numerical setups for the three different levels of gain. Figures 5.8a and 5.8b show the numerical frequency spectrum of bead's response overlaid on corresponding experimental results. When the force amplitude is small (0.1 N), numerical results show a resonance frequency of 5.6 kHz, which is slightly higher than that recorded in experiments (5.3 kHz). We conjecture that this is due to variations in contact stiffness at the time of experiments. In other words, k is calculated assuming perfect surfaces in Hertzian contact. However, these surfaces are not perfect and may degrade during experiment, leading to variations in resonance frequency. At high amplitudes (2 N), generation of second harmonic is evident in the numerical results. We note that in the numerical models, resonance frequency shifts from 5.62 kHz at 0.1 N to 5.6 kHz at 2 N. This shift (20 Hz) is significantly smaller than what we have in experiments (500 Hz). This observation is another indication that modeling contact using Hertzian law underestimates resonance shifts. Based on this

observation, we expect amplitude-dependent dispersion shift to be greater in experiments compared to numerical simulations.

Figures 5.8c and 5.8d show continuous wavelet transforms for the bead's response at 0.1 and 2 N. The presence of second harmonic at 2 N is a clear indication of the nonlinear nature of resonance. We also note that in the case of numerical simulations, transients persist for a longer duration before they completely disappear. This is due to the difference in damping characteristics of the experimental setup compared to the numerical model.

5.3.3 Plate with an array of bead-magnet resonators

The experimental setup is as shown in Figure 5.2. Two primary modes of excitation are utilized in this experiment: a wide-band sweep at low amplitudes that captures the linear response of the system, and a narrow-band slow sweep at higher amplitudes that is used to investigate the nonlinear characteristics of the system. Low-amplitude response is measured by using a wide-band fast (590 $\mathrm{Hz\,s^{-1}}$) sweep-up excitation. Dispersion reconstruction in the linear regime is carried out for the

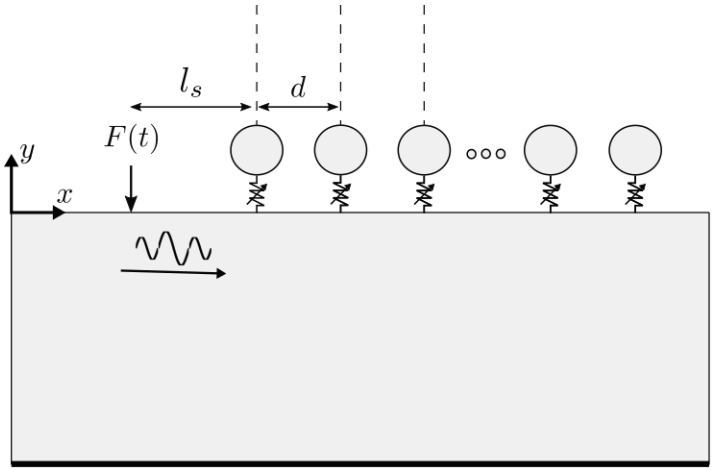

Figure 5.9: Schematics of the ABAQUS model, representing the experimental setup. The beads and magnets are modeled as discrete point masses, and nonlinear spring elements are used to model the contact stiffness.

pristine plate, plate with magnets as well as plate with bead-magnet resonators using this excitation. Due to evidence of softening nonlinearity in the response of the oscillator, the nonlinear system response is best characterized using a narrow-band slow (200 $\mathrm{Hz\,s^{-1}}$) sweep-down excitation from 6 kHz to 4 kHz.

Numerical simulations in ABAQUS are set up as explained in the previous section. Schematics of the

model is shown in Figure 5.9. Nonlinear springs are modeled as before. The plate is meshed with an approximate global size of 5 mm using free, advancing front algorithm. Linear quad-dominated plane-stress elements are used. The chosen mesh size guarantees to sufficiently discretize both the smallest wavelength λ_{min} and the smallest characteristic length of the system $d = 15$ mm. Linear bulk viscosity is used to introduce artificial damping in the system as before. As the case for single resonator on the plate, we will suffice to comparing the experimental and numerical results qualitatively; more specifically, we seek to corroborate that both show evidence of amplitude-dependent dispersion properties. Next, we present and discuss the experimental and numerical results for dispersion analysis.

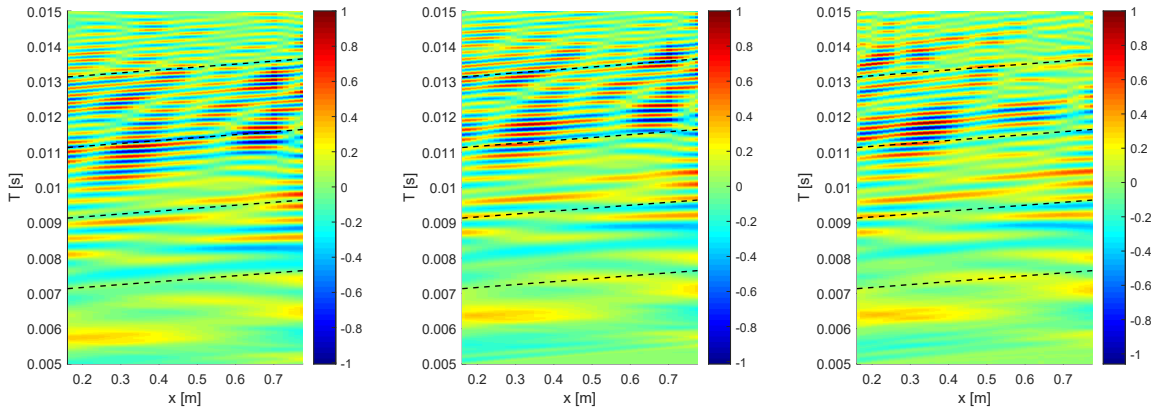

(a) (b) (c)

Figure 5.10: Spatio-temporal evolution of response for the (a) pristine plate, (b) plate with an array of magnets and (c) plate with an array of bead-magnet resonators. Slope of black dashed lines show theoretical prediction for wave speed in pristine plate.

As mentioned in section 5.2, we experimentally investigated the interaction of surface waves with the array of bead-magnet resonators by recording the vertical velocity at 42 stations along the edge of the plate. In order to reconstruct the dispersion curves experimentally, the recorded time-history response of the stations is postprocessed using 2D Fourier transforms. In the ABAQUS models, we define observation points at the same location as in the experimental setup. The response at these stations will be recorded throughout the simulation. This set of data collectively represents the spatio-temporal evolution of the response as the wave propagates through the system. In a similar manner as before, 2D Fourier transforms are used to postprocess the data.

In the linear regime, we reconstruct and numerically verify the dispersion for the pristine plate, plate with an array of magnets, and finally plate with an array of bead-magnet resonators. Reconstructing the dispersion curves for the pristine plate characterizes the original system, and helps us validate the theoretical wave speed predicted in 5.2. The second case will corroborate our assumption that

adding the magnets on their own does not introduce dispersive features in the system. Eventually, reconstructing dispersion for the third case will help us understand how surface acoustic waves interact with the bead-magnet resonators in the linear regime.

Figure 5.10 shows the spatio-temporal evolution of response on the plate's egde in experiments for the pristine plate, plate with an array of bead magnets and plate decorated with an array of bead-magnet resonators. Slope of the black dashed lines show the wave speed we predicted for edge waves in Section 5.2. For the first two cases, the wave travels along the edge of the plate with constant speed. However, for the third case, the figure shows that the wave is attenuated as it travels along the plate's edge as time progresses. Taking a closer look at the response in the wave-number frequency domain will help us analyze dispersion properties of each case.

Figure 5.11a shows the experimental dispersion curve for the pristine plate in a gray-scale contour. The broadband chirp generated by the shaker travels along the plate's edge dispersionless, as expected. The red dashed curve shows the dispersion line predicted by ABAQUS simulations. We note that numerical dispersion curves were originally in the form of contour plots as well. However, for visualization purposes, we only track the location of the maxima and use a smoothing spline to obtain the best fit for the data. This will allow for direct comparison between numerical and experimental results since both datasets can be overlaid. Figure 5.11a shows excellent agreement between experimental measurements and numerical simulations. We should note that the slope of the dispersion line also matches the theoretical prediction of $c_R = 1205\ \mathrm{m\,s^{-1}}$ in section 5.2.

Figure 5.11b shows the dispersion curve for the plate with an array of 41 magnets placed on the plate's edge. The magnets do not introduce any dispersive effects due to the their negligible mass (≈ 0.03 g).

Figure 5.11c shows the dispersion curves for the plate with an array of bead-magnet resonators. Placing the contact resonators on the plate's edge leads to hybridization between the traveling wave and the resonance modes. The slow-propagating flat branch observed in the dispersion plot is a result of SAW interaction with vertical resonances of the bead-magnet resonators. Similar phenomenon has been observed in microscale dynamics [152]. The frequencies where branches flatten indicate the resonance frequency of the beads. We observe a significant shift in resonance frequency compared to our measurements for the single bead on rigid substrate (from 7 kHz to nearly 5.6 kHz). This resonance shift, which is observed in the linear regime, could be associated with the coupling between the contact resonators and the compliant substrate. This effect is captured very well in the ABAQUS numerical model as it can be seen from the figure. The figure also shows that the experimental contour seems to

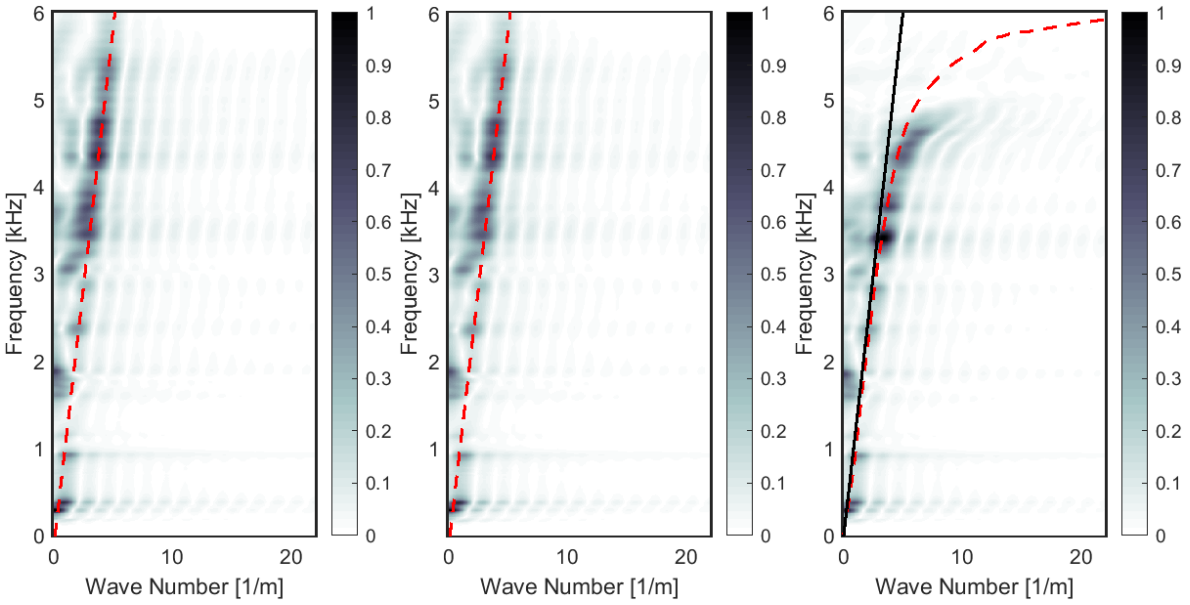

Figure 5.11: Dispersion reconstruction in the linear regime for (a) the pristine plate, (b) the plate with an array of magnets, and (c) the plate with an array of bead-magnet resonators. The contour shows the experimental reconstruction while the red dashed curves show numerical results from ABAQUS.

flatten at a lower frequency compared to numerical results. We conjecture that the chirp is too fast to capture the dispersion branch precisely in the experiments. We will show, later in this section, that using a slower chirp resolves this discrepancy.

In order to investigate the behavior of system in the nonlinear regime, we use the slow narrow-band chirp. Three different excitation amplitudes were chosen by changing the gain on Brüel and Kjær amplifier. Similar to the previous case, the response of the plate is measured at designated observation points along the edge. In order to quantify confidence in the experimental results, three sets of measurements were done at each amplitude, leading to nine sets of data in total. It is worth to note that after each measurement, all beads were removed and placed on magnets again. This was done to ensure that the results were not significantly affected by the uncertainties associated with the bead-magnet contact surface. Furthermore, the order in which the nine experiments were done was completely random. For each set of measurements at constant amplitude, recorded spatio-temporal data on plate's edge was postprocessed using 2D Fourier transforms. The average of Fourier amplitudes was then used to visualize the system's dispersion.

Figure 5.12 shows the reconstructed dispersion for the structure at three different excitation amplitudes. The gray-scale contour shows the full 2D visualization of response in the wave number-frequency

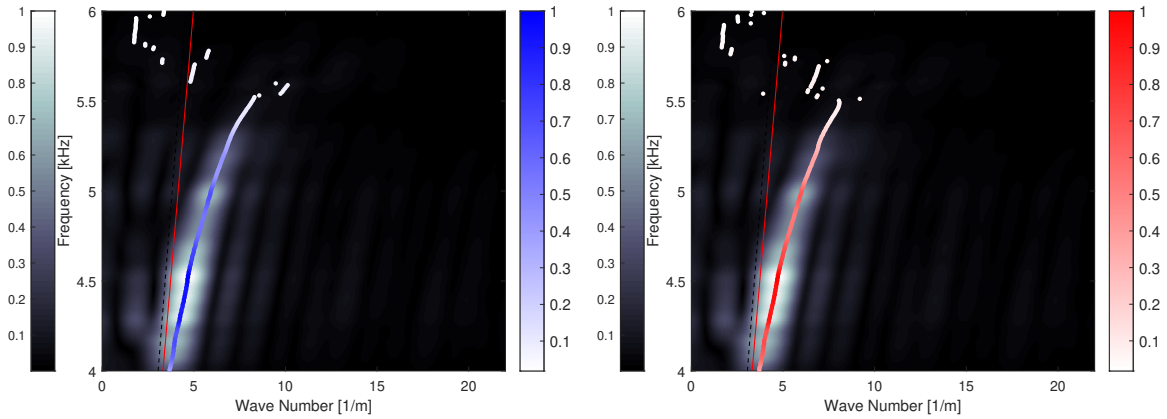

(a)

(b)

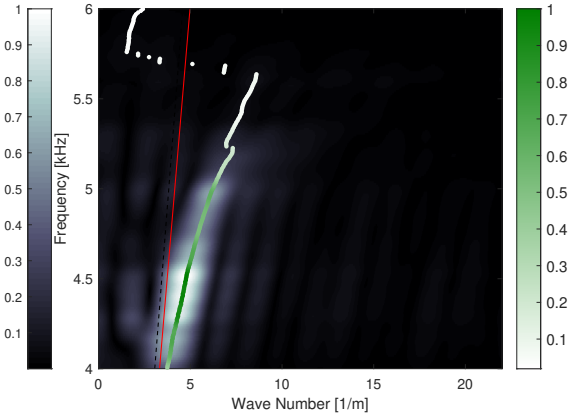

(c)

Figure 5.12: Dispersion reconstruction from experiments at (a) 10 dB, (b) 20 dB, and (c) 30 dB. Background contour shows the intensity of response in the frequency domain. Circles track the location of contour's maxima at each frequency. The color of each point indicates the peak's amplitude in the frequency spectrum.

domain, with white showing the highest intensity. The red line marks the dispersionless SAW propagation in the pristine plate while the slope of the dashed black line represents the shear wave speed. At each discrete frequency value, we identify the wave-number with maximum Fourier amplitude. This gives the overlaid scattered plots in blue, red and green. In addition, the color of circles at each point indicates the intensity of the Fourier amplitude, with white having the lowest intensity. This approach will prove itself crucial later for comparing the dispersion branches at different amplitudes. It also helps discard data points of little relevance. For example, we can see that in all figures, some points lie outside the sound cone, which is not physical. However, the intensity at these data points is extremely low. Therefore, we can safely ignore them. Another instance of anomaly is the apparent discontinuity of the dispersion branch around 5.2 kHz in Figure 5.12c. Like the previous case, the intensity of the

data points beyond the discontinuity is near zero. Therefore, we may ignore them for all practical purposes.

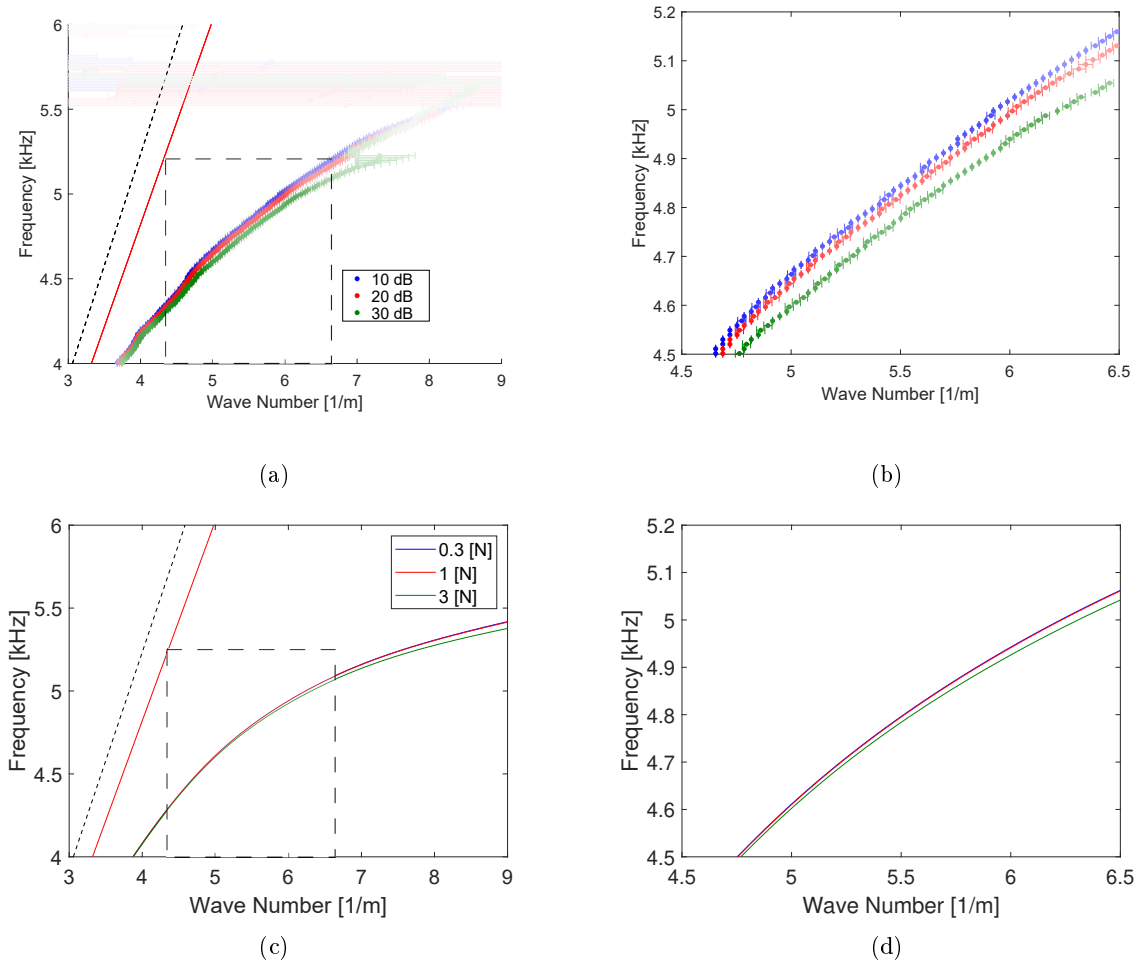

Figure 5.13: Dispersion reconstruction in a limited frequency region for varying excitation amplitudes. Numerical dispersion from ABAQUS simulations for the linear system (blue), the nonlinear system with unit point force (red), and nonlinear system with twice the forcing of the previous case (green).

Figure 5.13a shows the dispersion branches reconstructed at the three different amplitudes overlaid. The scattered plots in the previous case are now shown in the form of error-bar plots; that is, at each data point, the horizontal bars show the standard deviation for the three sets of measurement. We can clearly see that in the regions where intensity is high, standard deviation is extremely small. On the contrary, as intensity approaches zero, the standard deviation becomes very large. This is another evidence that data points with low intensity may be ignored. Where standard deviation is low, the figure shows that increasing the excitation amplitude shifts the dispersion curve to lower frequencies. Figure 5.13b shows the dispersion branches in a more limited wave number-frequency region to highlight the amplitude-dependent dispersion shift.

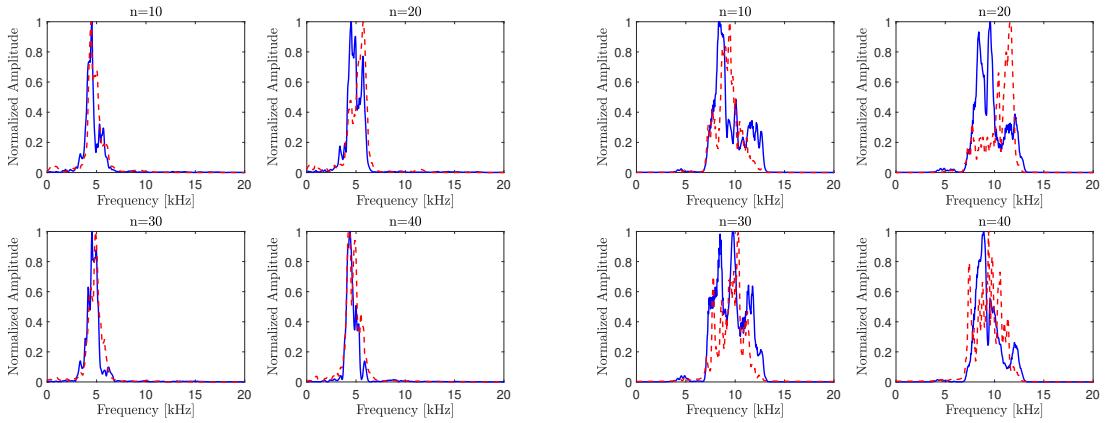

(a) (b)

Figure 5.14: Dynamics of select resonators interacting with the narrow-band chirp. (a) Normalized frequency spectrum of resonators for experiments at 30 dB (blue) and numerical models 3 N (red). n represents resonator number with 10 being closest to the shaker. (b) Similar to (a), after the application of the bandpass filter.

Numerical dispersion curves are obtained using the simulation setup described in the beginning of this section. Simulations are run for three different levels of forcing amplitude - 0.3, 1 and 3 N. These amplitudes were chosen such that maximum response amplitude reached in simulations and experiments are similar at the three different levels. In addition, since the experimental gains increase by a ratio of $\sqrt{10}$, a similar protocol was used for increasing the forcing amplitude in numerical simulations.

Figure 5.13c shows the numerical dispersion curves for the three different levels of amplitude mentioned. We note that these branches have been constructed in three steps: first, 2-D Fourier transforms were used on the spatio-temporal response of discrete points on the plate's edge to visualize dispersion in the frequency-wave number domain; next, at each frequency value, the wave number with highest Fourier amplitude is chosen to detect the dispersion branch; finally, a smoothing spline is fit to data points with maximum normalized Fourier amplitude greater than 0.15. Figure 5.13d shows the dispersion branches in a more limited wave number-frequency region to highlight the amplitude-dependent dispersion shift. We note that the shift observed in numerical results is less than that observed in experiments, as expected.

It would also be insightful to also study the dynamics of resonators. In the experimental setup, this was done by recording the velocity of each bead with the Laser Doppler Vibrometer at three different amplitude levels. In numerical simulations, we also recorded the time-history response of resonators for comparison. Results for select oscillators are shown in Figure 5.14. Figure 5.14a shows overlaid

frequency domain plots for the experimental and numerical response of the 10th, 20th, 30th and 40th bead at the highest excitation amplitude. Overall, there's a reasonable match between the two in terms of peak's locations. Although a seemingly larger discrepancy exists for the 20th resonator, the peak for numerical results lies at the location of a less pronounced peak in experimental data. However, unlike the case of a single resonator on plate, the nonlinear features are much smaller in magnitude and more difficult to detect. Therefore, we use a band-pass filter limited to the range of [8,12] kHz to reveal the nonlinear nature of the response. Figure 5.14b shows the frequency response of the resonators after the application of this band-pass filter. Similar to the previous case, multiple peaks appear in the frequency spectra. Discrepancy between peak locations are more pronounced than before since second harmonics are being considered. The emergence of higher harmonics and the similarity between experimental and numerical results corroborates the nonlinear nature of resonator dynamics.

5.4 Discussion

In this chapter, we adapted an experimental setup proposed in [135] to investigate the interaction of surface acoustic waves with nonlinear resonators. We exploited nonlinear properties of contact and used bead-magnet assemblies as nonlinear resonators. We started by investigating the nonlinear dynamics of an individual bead-magnet resonator. Using the Method of Multiple Scales, we predicted that the resonator has softening nonlinear characteristics - i.e. the resonance frequency decreases as the amplitude of motion increases. We, then, validated this claim with experiments. Next, the dynamics of a single resonator on an acrylic plate was considered. It was shown that the bead-magnet oscillator possessed all common traits of a nonlinear resonator, such as the existence of higher harmonics in the frequency spectra, the emergence of instabilities (so-called jump phenomenon), and resonance frequency shifts. We also used finite element simulations to verify our observations. Finally, in the last section, we focused our attention on studying dispersion properties of a plate with an array of bead-magnet resonators. The problem was investigated both experimentally and numerically. We started off by considering the system's dispersion properties in the linear regime, and showed that wave propagation in the pristine plate as well as plate with an array of magnets is, in fact, dispersionless. We also showed that the introduction of beads leads to hybridization between the traveling wave and resonance modes, resulting in the flattening of dispersion branch. Next, we investigated the variation of dispersive properties in the presence of nonlinearities, and showed, for the first time, experimental and numerical evidence of amplitude-dependent dispersion for surface waves.

As mentioned at the beginning of this chapter, the study of surface acoustic waves is essential in science. These waves find applications in different areas, from the design of radiofrequency filters and biosensors at small scales to the control of seismic waves at large scales. We showed that exploiting nonlinearity in the design of metamaterials is a promising avenue for passive-adaptive control of these waves. These findings may inform the design of tunable metamaterials for controlling surface acoustic waves at different scales. Among other applications, these findings are bound to be particularly consequential in the context of seismic wave attenuation; in fact, the large wave amplitude associated with seismic events are bound to excite the nonlinear characteristics of any metamaterial-inspired barrier.

The author would like to acknowledge limitations of the current work and make suggestions to improve the continuation of this work in future. Although we have established the nonlinear nature of contact resonances, it is essential to ensure that other elements involved in experiments are not contributing to dispersion shifts. One such element is the shaker. Characterizing the shaker's response in the frequency region of interest at different levels of gain would eliminate such concerns. One could also use the slow narrow-band chirp with different gains to reconstruct dispersion curves for the plate with an array of magnets in order to prove that the shift observed in the dispersion of plate with bead-magnet resonators is, indeed, due to the presence of beads and the nonlinear properties of contact. Another suggestion for increasing consistency among experiments, is to characterize the single bead-magnet nonlinear frequency response using the same input excitation utilized for reconstructing dispersion curves in the nonlinear regime. To increase consistency between experiments and simulations, it would have been ideal to characterize the damping properties of the plate. We also tried characterizing and installing a force sensor to determine the exact force applied on plate's edge by the shaker. However, due to the configuration of this experimental setup, dynamics of the force sensor was getting affected by plate's dynamics. This defeated the purpose of a force sensor. The author thinks finding an appropriate way to use a force sensor would greatly help with the validation of experiments through simulations. Finally, as we discussed in previous sections, Hertzian law does not represent the true nature of contact in this problem. Therefore, it would be of great value to investigate more suitable contact laws.

5.5 Conclusions and future work

We proposed a compact experimental setup to realize amplitude-dependent dispersion for surface waves. Conclusions of this chapter are summarized as follows:

- We used both theory and experiments to show that a bead-magnet contact resonator has softening

nonlinear properties and amplitude-dependent resonance frequency.

- A compliant substrate reduces the underlying resonance frequency of the bead-magnet oscillator. For sufficiently large amplitudes, we observe evidence for nonlinear resonance frequency shifts and generation of higher harmonics. A closer look also showed the emergence of instabilities and the so-called jump phenomenon, which is another characteristic of nonlinear systems.

- In general, the frequency shift observed in experiments is larger than that obtained from numerics. This is in line with the fact that Hertzian law underestimates resonance frequency shifts for such oscillators, and has direct consequences for the amount of shift we will observe for dispersion curves.

- We showed that wave propagation is dispersionless for the pristine plate and plate with an array of magnets. For the plate with an array of bead-magnet resonators, however, mode hybridizations in the linear regime lead to the flattening of branches around the resonance frequency of oscillators.

- We used a slow narrow-band chirp to investigate the system's dispersion properties and showed that as amplitude increases, the dispersion branch shifts towards lower frequencies. This offers experimental evidence for amplitude-dependent dispersion of surface waves for the first time.

- We showed that bead dynamics in this case is in general complicated and gets affected by the dynamics of the substrate. Using appropriate filters, we highlighted the generation of higher harmonics in the frequency spectra of resonators.

- As predicted in a previous item, the dispersion shifts predicted by numerical simulations are smaller than the ones observed in experiments since Hertzian law is used for modeling contact stiffness.

As we showed in the previous section, the dispersion shift achieved due to amplitude-dependence is limited. In future, it would be of interest to investigate the design of more versatile resonators that would realize more significant shifts due to variations in amplitude. We also showed how the presence of nonlinearities gives rise to the generation of higher harmonics, which may interact with the primary wave. It would also be interesting to study how this interaction may have additional consequences for wave propagation in the system. Due to huge implications that one-way propagation of surface waves could have in the design of telecommunication devices and mechanical diodes [136], another path to pursue is harnessing nonlinear effects to achieve surface-wave nonreciprocity. Additionally,

there are limited works on dispersion reconstruction for nonlinear metamaterials using chirp excitations. Investigating the effect of sweep-up and sweep-down excitations as well as the sweep rate on dispersion reconstruction for nonlinear systems would be an important step for future studies in this area. Another direction could focus on investigating the behavior of nonlinear metamaterials subject to transient inputs. These studies will be essential to the design of practical nonlinear metamaterials with applications for controlling transient wave phenomenon, such as earthquakes.

Chapter 6

Summary and future work

6.1 Summary

This dissertation aims to address the effects of modularity and nonlinearity in the design of metamaterials.

Chapters 2 and 3 were dedicated to the study of modular metamaterials. We started by a theoretical investigation of dispersion properties for a metamaterial beam that consists of flexural elements periodically coupled (entangled) along their length. We showed that the structure possesses multiple Bragg scattering and local resonance band gaps, and has unique wave-filtering properties unlike its constituents. We also showed how static tuning of connection properties can be used to alter the system's band structure. Next, entangled monoatomic chains were considered in two configurations. One is a configuration where each mass in one chain is connected to its corresponding mass in the other chain (full coupling). The other, consists of chains that are periodically coupled only at certain locations (partial coupling). We derived closed-form dispersion relations for both cases and discussed their eccentric dynamic properties, such as double-speed wave propagation zones, emergence of negative group velocity dispersion branches and flat bands. For each study, we used numerical simulations to verify our theoretical results, and present example devices targeted at wave propagation control using finite prototypes of each meta-structure.

In Chapters 4 and 5, we focused our attention on embedding nonlinearity in the design of metamaterials to control surface waves in a passive-adaptive manner. First, we presented an approximate theoretical framework for how Rayleigh waves interact with a periodic array of Duffing oscillators. Our analysis indicates that the presence of nonlinearities makes dispersion amplitude-dependent. We further showed that for hardening (softening) nonlinearities, dispersion branches shift towards higher (lower) frequencies as the amplitude of motion increases. In the light of this promising preliminary results, we attempted to realize the phenomenon in an experiment. In order to do this, we leveraged

a compact experimental setup consisting of a plate, serving as an elastic substrate, and bead-magnet assemblies, in lieu of nonlinear resonators. We studied the dynamics of the constituting elements of this structure in detail to present, for the first time, experimental evidence of amplitude-dependent dispersion for surface acoustic waves.

It is our hope that the findings of this two-part study will inform the design of more versatile metamaterials at different scales.

6.2 Future work

6.2.1 Smart Adaptive Metamaterials

Linear-elastic time-invariant systems, once engineered for certain topology and material properties, will have fixed dispersion characteristics. However, many application areas demand structural systems and materials that can adapt to external stimuli. Leveraging nonlinearity and time-modulation enables the design of such versatile systems. In the short run, the following research areas may be pursued:

- **Tunable and nonreciprocal wave control:** tunable and nonreciprocal wave control have broad applications; from amplitude-dependent wave-focusing devices for Non-Destructive Testing to redirecting mechanical shocks and vibrations.

- **Geo-inspired metamaterials:** Geophysical processes, such as friction and fracture of hard rocks and granular material, may be used to design devices that can enable solitary wave propagation, localization and in times chaotic behavior. This will have applications in areas such as energy focusing and directional propagation.

6.2.2 Metamaterials for controlling surface acoustic waves

Surface acoustic waves are acoustic waves traveling close to the surface of an elastic medium. Control and manipulation of these waves is of high interest in various areas of science and engineering. At scales of micrometers, these waves are essential for the design of biosensors and electronic filters while at the larger scales, they find application in earthquake engineering and geophysics. Some short-term research directions may include:

- **Control of SAWs in media with heterogeneity/nonlinearity:** this area would focus on how surface waves in heterogenous or nonlinear media would interact with metamaterials.

- **Control and manipulation of boundary waves:** manipulation of boundary waves at the interface of two materials are of interest in soils and layered composites.

- **Investigation of transient SAW control with mechanical metamaterials:** the transient response of metamaterials in the manipulation of surface waves needs to be investigated for earthquake engineering and impact applications.

Cross-collaborations with researchers in the field of Geotechnical engineering will enable the evaluation of these designs as seismic barriers and isolation systems at the foundation level of essential infrastructures.

On smaller scales, SAW devices are ubiquitous across disciplines; from MEMS and wireless sensors for structural health monitoring to delay devices and filters. Investigation of tunable and nonreciprocal wave control with SAW devices opens avenues for the design of smart sensing systems and the next generation of wireless networks. Metamaterials may be used to introduce a distribution of resonators at the surface of these devices in order to control and manipulate waves.

6.2.3 Data-Driven design of mechanical metamaterials

There is potential for applying machine learning and data-driven techniques to predict the dynamic properties of potential new designs and investigate functionality-driven design of metamaterials. Promising future directions in this area include:

- **Predicting the dynamic properties of mechanical metamaterials:** In the short run, it would be interesting to use machine learning to predict the band structure and dynamic properties of architected media. Currently, choosing the topology and material properties of new mechanical metamaterials relies largely on intuition, optimization and a trial and error procedure. The computational cost of determining the band structure of unit cells, which translates into solving multiple eigenvalue problems, grows significantly as wave number samples and the degrees of freedom increase. Using advanced data-driven techniques will help predict reliable band structures for complex 3-D designs by solving fewer eigenvalue problems. The computational power of machine learning will help sweeping huge design spaces much more efficiently.

- **Functionality-driven design of mechanical metamaterials:** This direction is in the spirit of NIST's Materials Genome Initiative (MGI), which has led to fast and cost-effective design solutions at nano and micro scales. There is an opportunity now to revolutionize the design of

mechanical metamaterials at scales relevant to structural and acoustic applications. The first step would rely on creating databases of different unit cell designs, characterizing potential features and labeling designs based on their efficacy for a desired functionality. These databases will be used to train machine learning models. The algorithm is then expected to asses a much larger set of potential designs in terms of a desired functionality. The best design may then be chosen using a search algorithm. This area will help us engineer systems that are structurally efficient and optimized for different purposes (shock absorption, energy harvesting, vibration suppression, etc.).

These advanced techniques will not only aid engineers in identifying important design features for specific applications but will also accelerate the otherwise computationally intensive search for adaptive and multifunctional structural designs.

Bibliography

[1] M. I. Hussein, M. J. Leamy, and M. Ruzzene, "Dynamics of phononic materials and structures: Historical origins, recent progress, and future outlook," *Applied Mechanics Reviews*, vol. 66, no. 4, 2014.

[2] Léon Brillouin, *Wave Propagation in Periodic Structures: Electric Filters and Crystal Lattices*. New York: McGraw-Hill Book Company, inc., 1st editio ed., 1946.

[3] S. Iijima, "Helical microtubules of graphitic carbon," *Nature*, vol. 354, no. 6348, pp. 56–58, 1991.

[4] K. S. Novoselov, A. K. Geim, S. V. Morozov, D. Jiang, Y. Zhang, S. V. Dubonos, I. V. Grigorieva, and A. A. Firsov, "Electric field effect in atomically thin carbon films.," *Science (New York, N.Y.)*, vol. 306, pp. 666–9, oct 2004.

[5] I. El-Kady, R. H. Olsson, and J. G. Fleming, "Phononic band-gap crystals for radio frequency communications," *Applied Physics Letters*, vol. 92, no. 23, 2008.

[6] J. F. V. Vincent, *Structural biomaterials*. Macmillan, 1982.

[7] L. J. Gibson, M. F. Ashby, and B. A. Harley, *Cellular materials in nature and medicine*.

[8] D. Yu, J. Wen, H. Zhao, Y. Liu, and X. Wen, "Vibration reduction by using the idea of phononic crystals in a pipe-conveying fluid," *Journal of Sound and Vibration*, 2008.

[9] M. Brun, G. F. Giaccu, A. B. Movchan, and N. V. Movchan, "Asymptotics of eigenfrequencies in the dynamic response of elongated multi-structures," *Proceedings of the Royal Society A: Mathematical, Physical and Engineering Sciences*, vol. 468, no. 2138, pp. 378–394, 2012.

[10] M. Brun, A. B. Movchan, and I. S. Jones, "Phononic Band Gap Systems in Structural Mechanics: Finite Slender Elastic Structures and Infinite Periodic Waveguides," *Journal of Vibration and Acoustics*, 2013.

[11] G. Carta, G. F. Giaccu, and M. Brun, "A phononic band gap model for long bridges. The 'Brabau' bridge case," *Engineering Structures*, vol. 140, pp. 66–76, jun 2017.

[12] A. L. Abrahamson, "The response of periodic structures to aero-acoustic pressures, with particular reference to aircraft skin-rib spar structures," 1973.

[13] D. J. Mead, "A general theory of harmonic wave propagation in linear periodic systems with multiple coupling," *Journal of Sound and Vibration*, vol. 27, pp. 235–260, mar 1973.

[14] Q. Chen and A. Elbanna, "Modulating Elastic Band Gap Structure in Layered Soft Composites Using Sacrificial Interfaces," *Journal of Applied Mechanics, Transactions ASME*, vol. 83, nov 2016.

[15] A. S. Phani, "Elastodynamics of Lattice Materials," in *Dynamics of Lattice Materials* (M. I. H. A. Srikantha Phani, ed.), ch. 3, p. 58, Wiley, 2017.

[16] S. Krödel, N. Thomé, and C. Daraio, "Wide band-gap seismic metastructures," *Extreme Mechanics Letters*, vol. 4, pp. 111–117, sep 2015.

[17] D. J. Colquitt, A. Colombi, R. V. Craster, P. Roux, and S. R. L. Guenneau, "Seismic metasurfaces: Sub-wavelength resonators and Rayleigh wave interaction," *Journal of the Mechanics and Physics of Solids*, vol. 99, pp. 379–393, feb 2017.

[18] A. Palermo, S. Krödel, K. Matlack, R. Zaccherini, V. Dertimanis, E. Chatzi, A. Marzani, and C. Daraio, "Large scale metasurfaces for seismic waves control," *The Journal of the Acoustical Society of America*, vol. 143, pp. 1713–1713, mar 2018.

[19] F. Casadei, T. Delpero, A. Bergamini, P. Ermanni, and M. Ruzzene, "Piezoelectric resonator arrays for tunable acoustic waveguides and metamaterials," *Journal of Applied Physics*, vol. 112, p. 064902, sep 2012.

[20] R. K. Pal and M. Ruzzene, "Edge waves in plates with resonators: an elastic analogue of the quantum valley Hall effect," *New Journal of Physics*, vol. 19, p. 025001, feb 2017.

[21] A. Darabi, A. Zareei, M.-R. Alam, and M. J. Leamy, "Broadband Bending of Flexural Waves: Acoustic Shapes and Patterns," *Scientific Reports*, vol. 8, p. 11219, dec 2018.

[22] S. Zhang, C. Xia, and N. Fang, "Broadband Acoustic Cloak for Ultrasound Waves," *Physical Review Letters*, vol. 106, p. 024301, jan 2011.

[23] A. Zareei and M.-R. Alam, "Broadband cloaking of flexural waves," *Physical Review E*, vol. 95, p. 063002, jun 2017.

[24] G. Ma and P. Sheng, "Acoustic metamaterials: From local resonances to broad horizons," 2016.

[25] M. I. Hussein, K. Hamza, G. M. Hulbert, and K. Saitou, "Optimal synthesis of 2D phononic crystals for broadband frequency isolation," *Waves in Random and Complex Media*, vol. 17, pp. 491–510, nov 2007.

[26] G. Aguzzi, A. Colombi, V. Dertimanis, and E. N. Chatzi, "Metamaterials for groundborne vibration absorption in pillars," tech. rep., ETH Zürich, 2020.

[27] R. Martínez-Sala, J. Sancho, J. V. Sánchez, V. Gómez, J. Llinares, and F. Meseguer, "Sound attenuation by sculpture," *Nature*, vol. 378, p. 241, nov 1995.

[28] H. Pichard, O. Richoux, and J.-P. Groby, "Experimental demonstrations in audible frequency range of band gap tunability and negative refraction in two-dimensional sonic crystal," *The Journal of the Acoustical Society of America*, vol. 132, pp. 2816–2822, oct 2012.

[29] A. Gueddida, Y. Pennec, S. Hemon, F. Lucklum, M. Vellekoop, N. Mukhin, R. Lucklum, B. Bonello, and B. Djafari Rouhani, "Numerical Analysis of a Tubular Phononic Crystal Sensor," in *Proceedings of IEEE Sensors*, vol. 2020-October, Institute of Electrical and Electronics Engineers Inc., oct 2020.

[30] Y. Pennec, Y. Jin, and B. Djafari-Rouhani, "Phononic and photonic crystals for sensing applications," *Advances in Applied Mechanics*, vol. 52, pp. 105–145, jan 2019.

[31] L. Feng, J. Chen, H. Huang, S. Huo, Z. Tan, X. Han, and G. Huang, "High-efficiency elastic wave rectifier in one-dimensional linear magnetoelastic phononic crystal slabs by an external magnetostatic field," *Physical Review Applied*, vol. 13, p. 064042, jun 2020.

[32] Y. Wang, B. Yousefzadeh, H. Chen, H. Nassar, G. Huang, and C. Daraio, "Observation of Nonreciprocal Wave Propagation in a Dynamic Phononic Lattice," *Physical Review Letters*, vol. 121, p. 194301, nov 2018.

[33] Z. Liu, X. Zhang, Y. Mao, Y. Y. Zhu, Z. Yang, C. T. Chan, and P. Sheng, "Locally resonant sonic materials," *Science (New York, N.Y.)*, vol. 289, pp. 1734–6, sep 2000.

[34] A. Colombi, D. Colquitt, P. Roux, S. Guenneau, and R. V. Craster, "A seismic metamaterial: The resonant metawedge," *Scientific Reports*, vol. 6, pp. 1–6, jun 2016.

[35] S. Benchabane and A. Reinhardt, "Elastic Metamaterials for Radiofrequency Applications," in *Fundamentals and Applications of Acoustic Metamaterials*, pp. 207–262, Wiley, aug 2019.

[36] N. Kaina, F. Lemoult, M. Fink, and G. Lerosey, "Negative refractive index and acoustic superlens from multiple scattering in single negative metamaterials," *Nature*, vol. 525, pp. 77–81, sep 2015.

[37] R. Fuentes-Domínguez, M. Yao, A. Colombi, P. Dryburgh, D. Pieris, A. Jackson-Crisp, D. Colquitt, A. Clare, R. J. Smith, and M. Clark, "Design of a resonant Luneburg lens for surface acoustic waves," *Ultrasonics*, vol. 111, p. 106306, mar 2021.

[38] R. Zhu, X. N. Liu, G. K. Hu, C. T. Sun, and G. L. Huang, "Negative refraction of elastic waves at the deep-subwavelength scale in a single-phase metamaterial," *Nature Communications*, vol. 5, pp. 1–8, nov 2014.

[39] S. Zhang, L. Yin, and N. Fang, "Focusing ultrasound with an acoustic metamaterial network," *Physical Review Letters*, vol. 102, may 2009.

[40] C. L. Bacquet, H. Al Ba'ba'a, M. J. Frazier, and M. Nouh, "Metadamping: Dissipation Emergence in Elastic Metamaterials," *Advances in Applied Mechanics*, vol. 51, pp. 115–164, jan 2018.

[41] G. Hu, L. Tang, R. Das, S. Gao, and H. Liu, "Acoustic metamaterials with coupled local resonators for broadband vibration suppression," *AIP Advances*, vol. 7, feb 2017.

[42] D. Beli, J. R. F. Arruda, and M. Ruzzene, "Wave propagation in elastic metamaterial beams and plates with interconnected resonators," *International Journal of Solids and Structures*, vol. 139-140, pp. 105–120, may 2018.

[43] D. DePauw, H. Al Ba'ba'a, and M. Nouh, "Metadamping and energy dissipation enhancement via hybrid phononic resonators," *Extreme Mechanics Letters*, vol. 18, pp. 36–44, jan 2018.

[44] G. Gupta, *Dynamics of Periodically Stiffened Structures Using a Wave Approach*. PhD thesis, University of Southampton (United Kingdom), 1971.

[45] J. Wang, C. M. Mak, and Y. Yun, "A methodology for direct identification of characteristic wavetypes in a finite periodic dual-layer structure with transverse connection," *Journal of Vibration and Control*, vol. 18, pp. 1406–1414, aug 2012.

[46] H. Xiuchang, J. Aihua, Z. Zhiyi, and H. Hongxing, "Design and optimization of periodic structure mechanical filter in suppression of foundation resonances," *Journal of Sound and Vibration*, vol. 330, pp. 4689–4712, sep 2011.

[47] Q. Chen and A. Elbanna, "Emergent wave phenomena in coupled elastic bars: From extreme attenuation to realization of elastodynamic switches," *Scientific Reports*, vol. 7, dec 2017.

[48] P. Deymier and K. Runge, "One-Dimensional Mass-Spring Chains Supporting Elastic Waves with Non-Conventional Topology," *Crystals*, vol. 6, p. 44, apr 2016.

[49] P. A. Deymier and K. Runge, "Non-separable states in a bipartite elastic system," *AIP Advances*, vol. 7, apr 2017.

[50] P. A. Deymier, K. Runge, P. Lucas, and J. O. Vasseur, "Spacetime representation of topological phononics," *New Journal of Physics*, vol. 20, may 2018.

[51] M. A. Hasan, L. Calderin, T. Lata, P. Lucas, K. Runge, and P. A. Deymier, "Directional elastic pseudospin and nonseparability of directional and spatial degrees of freedom in parallel arrays of coupled waveguides," *Applied Sciences (Switzerland)*, vol. 10, p. 3202, may 2020.

[52] C. Daraio, V. F. Nesterenko, E. B. Herbold, and S. Jin, "Tunability of solitary wave properties in one-dimensional strongly nonlinear phononic crystals," *Physical Review E - Statistical, Nonlinear, and Soft Matter Physics*, vol. 73, no. 2, 2006.

[53] R. K. Narisetti, M. J. Leamy, and M. Ruzzene, "A perturbation approach for predicting wave propagation in one-dimensional nonlinear periodic structures," *Journal of Vibration and Acoustics, Transactions of the ASME*, vol. 132, pp. 0310011–03100111, jun 2010.

[54] A. F. Vakakis, M. E. King, and A. J. Pearlstein, "Forced localization in a periodic chain of nonlinear oscillators," *International Journal of Non-Linear Mechanics*, vol. 29, no. 3, pp. 429–447, 1994.

[55] A. J. Sievers and S. Takeno, "Intrinsic localized modes in anharmonic crystals," *Physical Review Letters*, vol. 61, no. 8, pp. 970–973, 1988.

[56] A. Krasnok, M. Tymchenko, and A. Alù, "Nonlinear metasurfaces: a paradigm shift in nonlinear optics," jan 2018.

[57] X. Guo, V. E. Gusev, V. Tournat, B. Deng, and K. Bertoldi, "Frequency-doubling effect in acoustic reflection by a nonlinear, architected rotating-square metasurface," *Physical Review E*, vol. 99, may 2019.

[58] J. Bunyan, K. J. Moore, A. Mojahed, M. D. Fronk, M. Leamy, S. Tawfick, and A. F. Vakakis, "Acoustic nonreciprocity in a lattice incorporating nonlinearity, asymmetry, and internal scale hierarchy: Experimental study," *Physical Review E*, vol. 97, p. 52211, may 2018.

[59] M. D. Fronk, S. Tawfick, C. Daraio, S. Li, A. Vakakis, and M. J. Leamy, "Acoustic non-reciprocity in lattices with nonlinearity, internal hierarchy, and asymmetry: Computational study," *Journal of Vibration and Acoustics, Transactions of the ASME*, vol. 141, oct 2019.

[60] A. Mojahed, O. V. Gendelman, and A. F. Vakakis, "Breather arrest, localization, and acoustic non-reciprocity in dissipative nonlinear lattices," *The Journal of the Acoustical Society of America*, vol. 146, pp. 826–842, jul 2019.

[61] X. Fang, J. Wen, D. Yu, G. Huang, and J. Yin, "Wave propagation in a nonlinear acoustic metamaterial beam considering third harmonic generation," *New Journal of Physics*, vol. 20, p. 123028, dec 2018.

[62] A. Casalotti, S. El-Borgi, and W. Lacarbonara, "Metamaterial beam with embedded nonlinear vibration absorbers," *International Journal of Non-Linear Mechanics*, vol. 98, pp. 32–42, jan 2018.

[63] R. K. Narisetti, *Wave propagation in nonlinear periodic structures*. PhD thesis, Georegia Institute of Technology, 2010.

[64] K. L. Manktekow, *Dispersion analysis of nonlinear periodic structures*. PhD thesis, Georgia Institute of Technology, 2013.

[65] R. Khajehtourian and M. I. Hussein, "Dispersion characteristics of a nonlinear elastic metamaterial," *AIP Advances*, vol. 4, p. 124308, dec 2014.

[66] P. B. Silva, M. J. Leamy, M. G. D. Geers, and V. G. Kouznetsova *arXiv*.

[67] P. B. Silva, M. J. Leamy, M. G. Geers, and V. G. Kouznetsova, "Emergent subharmonic band gaps in nonlinear locally resonant metamaterials induced by autoparametric resonance," *Physical Review E*, vol. 99, p. 063003, jun 2019.

[68] V. Zega, P. B. Silva, M. G. Geers, and V. G. Kouznetsova, "Experimental proof of emergent subharmonic attenuation zones in a nonlinear locally resonant metamaterial," *Scientific Reports*, vol. 10, p. 12041, dec 2020.

[69] S. Hajarolasvadi and A. E. Elbanna, "Dynamics of metamaterial beams consisting of periodically-coupled parallel flexural elements: A theoretical study," *Journal of Physics D: Applied Physics*, vol. 52, p. 315101, may 2019.

[70] J. Miles, "Vibrations of Beams on Many Supports," *Proceedings of the American Society of Civil Engineers*, vol. 82, no. 1, pp. 1–9, 1956.

[71] E. E. Ungar, "Steady-State Responses of One-Dimensional Periodic Flexural Systems," *The Journal of the Acoustical Society of America*, vol. 39, no. March 1965, 1965.

[72] H. J. Xiang and Z. F. Shi, "Analysis of flexural vibration band gaps in periodic beams using differential quadrature method," *Computers and Structures*, 2009.

[73] C. Zhou, M. Ichchou, J.-P. Lainé, and A. Zine, "Application of wave finite element method on reduced models for the analysis of flexural waves in periodic beams," in *1st Euro Mediterranean Conference on Structural Dynamics and Vibroacoustics*, apr 2013.

[74] D. J. Thompson, "A continuous damped vibration absorber to reduce broad-band wave propagation in beams," *Journal of Sound and Vibration*, 2008.

[75] Y. Xiao, J. Wen, and X. Wen, "Broadband locally resonant beams containing multiple periodic arrays of attached resonators," *Physics Letters, Section A: General, Atomic and Solid State Physics*, vol. 376, no. 16, pp. 1384–1390, 2012.

[76] V. Candido de Sousa, C. Sugino, C. De Marqui Junior, and A. Erturk, "Adaptive locally resonant metamaterials leveraging shape memory alloys," *Journal of Applied Physics*, vol. 124, p. 064505, aug 2018.

[77] C. Sugino, S. Leadenham, M. Ruzzene, and A. Erturk, "On the mechanism of bandgap formation in locally resonant finite elastic metamaterials," *Journal of Applied Physics*, vol. 120, p. 134501, oct 2016.

[78] H. Sun, X. Du, and P. F. Pai, "Theory of metamaterial beams for broadband vibration absorption," *Journal of Intelligent Material Systems and Structures*, 2010.

[79] M. Y. Wang and X. Wang, "Frequency band structure of locally resonant periodic flexural beams suspended with force–moment resonators," *Journal of Physics D: Applied Physics*, vol. 46, p. 255502, jun 2013.

[80] Y. Xiao, J. Wen, G. Wang, and X. Wen, "Theoretical and Experimental Study of Locally Resonant and Bragg Band Gaps in Flexural Beams Carrying Periodic Arrays of Beam-Like Resonators," *Journal of Vibration and Acoustics*, vol. 135, p. 041006, jun 2013.

[81] Y. Xiao, J. Wen, D. Yu, and X. Wen, "Flexural wave propagation in beams with periodically

attached vibration absorbers: Band-gap behavior and band formation mechanisms," *Journal of Sound and Vibration*, 2013.

[82] L. Liu and M. I. Hussein, "Wave Motion in Periodic Flexural Beams and Characterization of the Transition Between Bragg Scattering and Local Resonance," *Journal of Applied Mechanics*, vol. 79, p. 11003, jan 2012.

[83] X. Wang and M. Y. Wang, "An analysis of flexural wave band gaps of locally resonant beams with continuum beam resonators," *Meccanica*, vol. 51, pp. 171–178, jan 2016.

[84] D. Krattiger and M. I. Hussein, "Bloch mode synthesis: Ultrafast methodology for elastic band-structure calculations," *Physical Review E - Statistical, Nonlinear, and Soft Matter Physics*, 2014.

[85] C. Goffaux, J. Sánchez-Dehesa, A. L. Yeyati, P. Lambin, A. Khelif, J. O. Vasseur, and B. Djafari-Rouhani, "Evidence of Fano-Like Interference Phenomena in Locally Resonant Materials," *Physical Review Letters*, vol. 88, p. 225502, may 2002.

[86] P. F. Pai, "Metamaterial-based Broadband Elastic Wave Absorber," *Journal of Intelligent Material Systems and Structures*, vol. 21, pp. 517–528, mar 2010.

[87] P. F. Pai, H. Peng, and S. Jiang, "Acoustic metamaterial beams based on multi-frequency vibration absorbers," *International Journal of Mechanical Sciences*, vol. 79, pp. 195–205, feb 2014.

[88] Y. Xiao, B. R. Mace, J. Wen, and X. Wen, "Formation and coupling of band gaps in a locally resonant elastic system comprising a string with attached resonators," *Physics Letters A*, vol. 375, pp. 1485–1491, mar 2011.

[89] F. ROMEO and A. LUONGO, "Invariant Representation Of Propogation Properties For Bi-Coupled Periodic Structures," *Journal of Sound and Vibration*, vol. 257, pp. 869–886, nov 2002.

[90] S. Hajarolasvadi and A. E. Elbanna, "Dispersion properties and dynamics of ladder-like metachains," *Extreme Mechanics Letters*, vol. 43, p. 101133, feb 2021.

[91] H. H. Huang, C. T. Sun, and G. L. Huang, "On the negative effective mass density in acoustic metamaterials," *International Journal of Engineering Science*, vol. 47, pp. 610–617, apr 2009.

[92] G. L. Huang and C. T. Sun, "Band gaps in a multiresonator acoustic metamaterial," *Journal of Vibration and Acoustics, Transactions of the ASME*, vol. 132, pp. 0310031–0310036, jun 2010.

[93] H. Chen, X. P. Li, Y. Y. Chen, and G. L. Huang, "Wave propagation and absorption of sandwich beams containing interior dissipative multi-resonators," *Ultrasonics*, vol. 76, pp. 99–108, apr 2017.

[94] R. Zhu, X. N. Liu, G. K. Hu, F. G. Yuan, and G. L. Huang, "Microstructural designs of plate-type elastic metamaterial and their potential applications: a review," *International Journal of Smart and Nano Materials*, vol. 6, pp. 14–40, jan 2015.

[95] A. A. Mokhtari, Y. Lu, and A. Srivastava, "Optimized phononic crystals for bandGap and metamaterial properties," in *Health Monitoring of Structural and Biological Systems XII*, vol. 10600, p. 68, SPIE-Intl Soc Optical Eng, mar 2018.

[96] A. A. Mokhtari, Y. Lu, and A. Srivastava, "On the emergence of negative effective density and modulus in 2-phase phononic crystals," *Journal of the Mechanics and Physics of Solids*, vol. 126, pp. 256–271, may 2019.

[97] Q. Chen and A. Elbanna, "Tension-induced tunable corrugation in two-phase soft composites:

Mechanisms and implications," *Extreme Mechanics Letters*, vol. 4, pp. 26–37, sep 2015.

[98] A. Bylinskii, D. Gangloff, I. Counts, and V. Vuletić, "Observation of Aubry-type transition in finite atom chains via friction," *Nature Materials*, vol. 15, pp. 717–721, jul 2016.

[99] B. A. Erickson, B. Birnir, and D. Lavallée, "Periodicity, chaos and localization in a Burridge-Knopoff model of an earthquake with rate-and-state friction," *Geophysical Journal International*, vol. 187, pp. 178–198, oct 2011.

[100] A. E. Elbanna and T. H. Heaton, "A new paradigm for simulating pulse-like ruptures: The pulse energy equation," *Geophysical Journal International*, vol. 189, pp. 1797–1806, jun 2012.

[101] Léon Brillouin, *Wave Propagation in Periodic Structures: Electric Filters and Crystal Lattices*. New York: McGraw-Hill Book Company, inc., 1st editio ed., 1946.

[102] N. Boechler, J. Yang, G. Theocharis, P. G. Kevrekidis, and C. Daraio, "Tunable vibrational band gaps in one-dimensional diatomic granular crystals with three-particle unit cells," in *Journal of Applied Physics*, vol. 109, p. 074906, American Institute of PhysicsAIP, apr 2011.

[103] F. Li, P. Anzel, J. Yang, P. G. Kevrekidis, and C. Daraio, "Granular acoustic switches and logic elements," *Nature Communications*, vol. 5, pp. 1–6, oct 2014.

[104] L. Bonanomi, G. Theocharis, and C. Daraio, "Wave propagation in granular chains with local resonances," *Physical Review E - Statistical, Nonlinear, and Soft Matter Physics*, vol. 91, p. 033208, mar 2015.

[105] A. Darabi, L. Fang, A. Mojahed, M. D. Fronk, A. F. Vakakis, and M. J. Leamy, "Broadband passive nonlinear acoustic diode," *Physical Review B*, vol. 99, p. 214305, jun 2019.

[106] P. A. Deymier, "Introduction to Phononic Crystals and Acoustic Metamaterials," in *Acoustic Metamaterials and Phononic Crystals*, pp. 1–12, Springer, 2013.

[107] C. M. Da Fonseca and J. Petronilho, "Explicit inverses of some tridiagonal matrices," *Linear Algebra and Its Applications*, vol. 325, pp. 7–21, mar 2001.

[108] D. Leykam, A. Andreanov, and S. Flach, "Artificial flat band systems: From lattice models to experiments," jan 2018.

[109] V. Yantchev, L. Arapan, I. Katardjiev, and V. Plessky, "Thin-film zero-group-velocity Lamb wave resonator," *Applied Physics Letters*, vol. 99, p. 033505, jul 2011.

[110] K. H. Matlack, M. Serra-Garcia, A. Palermo, S. D. Huber, and C. Daraio, "Designing perturbative metamaterials from discrete models," *Nature Materials*, vol. 17, pp. 323–328, apr 2018.

[111] R. A. Vicencio, C. Cantillano, L. Morales-Inostroza, B. Real, C. Mejía-Cortés, S. Weimann, A. Szameit, and M. I. Molina, "Observation of Localized States in Lieb Photonic Lattices," *Physical Review Letters*, vol. 114, p. 245503, jun 2015.

[112] P. Celli, B. Yousefzadeh, C. Daraio, and S. Gonella, "Bandgap widening by disorder in rainbow metamaterials," *Applied Physics Letters*, vol. 114, mar 2017.

[113] M. A. Hasan, Y. Starosvetsky, A. F. Vakakis, and L. I. Manevitch, "Nonlinear targeted energy transfer and macroscopic analog of the quantum Landau-Zener effect in coupled granular chains," *Physica D: Nonlinear Phenomena*, vol. 252, pp. 46–58, jun 2013.

[114] C. Wang, S. Tawfick, and A. F. Vakakis, "Irreversible energy transfer, localization and non-reciprocity in weakly coupled, nonlinear lattices with asymmetry," *Physica D: Nonlinear Phe-*

nomena, jan 2019.

[115] S. Foti, S. Parolai, D. Albarello, and M. Picozzi, "Application of Surface-Wave Methods for Seismic Site Characterization," *Surveys in Geophysics*, vol. 32, pp. 777–825, nov 2011.

[116] S. C. Griffiths, B. R. Cox, E. M. Rathje, and D. P. Teague, "Surface-Wave Dispersion Approach for Evaluating Statistical Models That Account for Shear-Wave Velocity Uncertainty," *Journal of Geotechnical and Geoenvironmental Engineering*, vol. 142, p. 04016061, nov 2016.

[117] G. Hévin, O. Abraham, H. A. Pedersen, and M. Campillo, "Characterisation of surface cracks with rayleigh waves: A numerical model," *NDT and E International*, vol. 31, pp. 289–297, aug 1998.

[118] J. H. Kim and H. G. Kwak, "Nondestructive evaluation of elastic properties of concrete using simulation of surface waves," *Computer-Aided Civil and Infrastructure Engineering*, vol. 23, pp. 611–624, nov 2008.

[119] A. Palermo, S. Krödel, A. Marzani, and C. Daraio, "Engineered metabarrier as shield from seismic surface waves," *Scientific Reports*, vol. 6, pp. 1–10, dec 2016.

[120] S. Brûlé, E. H. Javelaud, S. Enoch, and S. Guenneau, "Experiments on seismic metamaterials: Molding surface waves," *Physical Review Letters*, vol. 112, p. 133901, dec 2013.

[121] B. F. Spencer and S. Nagarajaiah, "State of the Art of Structural Control," *Journal of Structural Engineering*, vol. 129, pp. 845–856, jul 2003.

[122] T. H. Heaton, J. F. Hall, D. J. Wald, and M. W. Halling, "Response of high-rise and base-isolated buildings to a hypothetical M w 7.0 blind thrust earthquake," *Science*, vol. 267, pp. 206–211, jan 1995.

[123] W. L. Ellsworth, A. L. Llenos, A. F. McGarr, A. J. Michael, J. L. Rubinstein, C. S. Mueller, M. D. Petersen, and E. Calais, "Increasing seismicity in the U. S. midcontinent: Implications for earthquake hazard," *Leading Edge*, vol. 34, pp. 618–626, jun 2015.

[124] A. Colombi, P. Roux, S. Guenneau, P. Gueguen, and R. V. Craster, "Forests as a natural seismic metamaterial: Rayleigh wave bandgaps induced by local resonances," *Scientific Reports*, vol. 6, jan 2016.

[125] N. Boechler, J. K. Eliason, A. Kumar, A. A. Maznev, K. A. Nelson, and N. Fang, "Interaction of a contact resonance of microspheres with surface acoustic waves," *Physical Review Letters*, vol. 111, p. 036103, jul 2013.

[126] S. Benchabane, A. Khelif, J. Y. Rauch, L. Robert, and V. Laude, "Evidence for complete surface wave band gap in a piezoelectric phononic crystal," *Physical Review E - Statistical, Nonlinear, and Soft Matter Physics*, vol. 73, no. 6, pp. 1–4, 2006.

[127] K. Länge, B. E. Rapp, and M. Rapp, "Surface acoustic wave biosensors: A review," jul 2008.

[128] Muhammad, C. W. Lim, and J. N. Reddy, "Built-up structural steel sections as seismic metamaterials for surface wave attenuation with low frequency wide bandgap in layered soil medium," *Engineering Structures*, vol. 188, pp. 440–451, jun 2019.

[129] T. T. Wu, J. C. Hsu, J. H. Sun, and S. Benchabane, "Surface acoustic waves in phononic crystals," in *Phononic Crystals: Fundamentals and Applications*, pp. 145–189, Springer New York, jul 2015.

[130] O. B. Wright and O. Matsuda, "Watching surface waves in phononic crystals," *Philosophical Transactions of the Royal Society A: Mathematical, Physical and Engineering Sciences*, vol. 373,

p. 20140364, aug 2015.

[131] A. Khelif, Y. Achaoui, S. Benchabane, V. Laude, and B. Aoubiza, "Locally resonant surface acoustic wave band gaps in a two-dimensional phononic crystal of pillars on a surface," *Physical Review B - Condensed Matter and Materials Physics*, vol. 81, p. 214303, jun 2010.

[132] F. Zeighami, A. Palermo, and A. Marzani, "Rayleigh waves in locally resonant metamaterials," *International Journal of Mechanical Sciences*, vol. 195, p. 106250, dec 2020.

[133] M. Addouche, M. A. Al-Lethawe, A. Choujaa, and A. Khelif, "Superlensing effect for surface acoustic waves in a pillar-based phononic crystal with negative refractive index," *Applied Physics Letters*, vol. 105, p. 023501, jul 2014.

[134] N. Cselyuszka, M. Sečujski, N. Engheta, and V. Crnojević-Bengin, "Temperature-controlled acoustic surface waves," *New Journal of Physics*, vol. 18, no. 10, 2016.

[135] A. Palermo, Y. Wang, P. Celli, and C. Daraio, "Tuning of Surface-Acoustic-Wave Dispersion via Magnetically Modulated Contact Resonances," *Physical Review Applied*, vol. 11, no. 4, p. 1, 2019.

[136] A. Palermo, P. Celli, B. Yousefzadeh, C. Daraio, and A. Marzani, "Surface wave non-reciprocity via time-modulated metamaterials," *Journal of the Mechanics and Physics of Solids*, vol. 145, p. 104181, dec 2020.

[137] S. Alan, A. Allam, and A. Erturk, "Programmable mode conversion and bandgap formation for surface acoustic waves using piezoelectric metamaterials," *Applied Physics Letters*, vol. 115, p. 093502, aug 2019.

[138] W. Jiao and S. Gonella, "Doubly nonlinear waveguides with self-switching functionality selection capabilities," *Physical Review E*, vol. 99, p. 042206, apr 2019.

[139] K. J. Moore, J. Bunyan, S. Tawfick, O. V. Gendelman, S. Li, M. Leamy, and A. F. Vakakis, "Nonreciprocity in the dynamics of coupled oscillators with nonlinearity, asymmetry, and scale hierarchy," *Physical Review E*, vol. 97, p. 012219, jan 2018.

[140] L. Fang, A. Darabi, A. Mojahed, A. F. Vakakis, and M. J. Leamy, "Broadband non-reciprocity with robust signal integrity in a triangle-shaped nonlinear 1D metamaterial," *Nonlinear Dynamics*, vol. 100, pp. 1–13, mar 2020.

[141] D. Zhou, J. Ma, K. Sun, S. Gonella, and X. Mao, "Switchable phonon diodes using nonlinear topological Maxwell lattices," *Physical Review B*, vol. 101, p. 104106, mar 2020.

[142] W. Jiao and S. Gonella, "Intermodal and Subwavelength Energy Trapping in Nonlinear Metamaterial Waveguides," *Physical Review Applied*, vol. 10, p. 024006, aug 2018.

[143] W. Jiao and S. Gonella, "Mechanics of inter-modal tunneling in nonlinear waveguides," *Journal of the Mechanics and Physics of Solids*, vol. 111, pp. 1–17, feb 2018.

[144] R. K. Narisetti, M. Ruzzene, and M. J. Leamy, "Study of wave propagation in strongly nonlinear periodic lattices using a harmonic balance approach," *Wave Motion*, vol. 49, pp. 394–410, mar 2012.

[145] R. K. Narisetti, M. Ruzzene, and M. J. Leamy, "Study of wave propagation in strongly nonlinear periodic lattices using a harmonic balance approach," *Wave Motion*, vol. 49, pp. 394–410, mar 2012.

[146] K. Manktelow, M. J. Leamy, and M. Ruzzene, "Multiple scales analysis of wave-wave interactions

in a cubically nonlinear monoatomic chain," *Nonlinear Dynamics*, vol. 63, pp. 193–203, jan 2011.

[147] K. Manktelow, R. K. Narisetti, M. J. Leamy, and M. Ruzzene, "Finite-element based perturbation analysis of wave propagation in nonlinear periodic structures," *Mechanical Systems and Signal Processing*, vol. 39, pp. 32–46, aug 2013.

[148] R. Khajehtourian and M. I. Hussein, "Dispersion characteristics of a nonlinear elastic metamaterial," *AIP Advances*, vol. 4, p. 124308, dec 2014.

[149] B. S. Lazarov and J. S. Jensen, "Low-frequency band gaps in chains with attached non-linear oscillators," *International Journal of Non-Linear Mechanics*, vol. 42, pp. 1186–1193, dec 2007.

[150] J. M. Manimala and C. T. Sun, "Numerical investigation of amplitude-dependent dynamic response in acoustic metamaterials with nonlinear oscillators," *The Journal of the Acoustical Society of America*, vol. 139, pp. 3365–3372, jun 2016.

[151] K. L. Manktelow, M. Ruzzene, and M. J. Leamy, "Wave Propagation in Nonlinear Lattice Materials," in *Dynamics of Lattice Materials*, pp. 107–137, Chichester, UK: John Wiley & Sons, Ltd, jul 2017.

[152] S. P. Wallen, A. A. Maznev, and N. Boechler, "Dynamics of a monolayer of microspheres on an elastic substrate," *Physical Review B - Condensed Matter and Materials Physics*, vol. 92, no. 17, pp. 1–9, 2015.

[153] M. Hiraiwa, M. Abi Ghanem, S. P. Wallen, A. Khanolkar, A. A. Maznev, and N. Boechler, "Complex Contact-Based Dynamics of Microsphere Monolayers Revealed by Resonant Attenuation of Surface Acoustic Waves," *Physical Review Letters*, vol. 116, p. 198001, may 2016.

[154] S. P. Wallen, J. Lee, D. Mei, C. Chong, P. G. Kevrekidis, and N. Boechler, "Discrete breathers in a mass-in-mass chain with Hertzian local resonators," *Physical Review E*, vol. 95, p. 022904, feb 2017.

[155] A. H. Nayfeh and D. T. Mook, *Nonlinear Oscillations*. Wiley, may 1995.

[156] E. Rigaud and J. Perret-Liaudet, "Experiments and numerical results on non-linear vibrations of an impacting Hertzian contact. Part 1: Harmonic excitation," *Journal of Sound and Vibration*, vol. 265, pp. 289–307, aug 2003.

[157] J. Perret-Liaudet and E. Rigaud, "Experiments and numerical results on non-linear vibrations of an impacting Hertzian contact. Part 2: Random excitation," *Journal of Sound and Vibration*, vol. 265, pp. 309–327, aug 2003.

[158] A. Merkel, G. Theocharis, F. Allein, J. P. Groby, V. Gusev, and V. Tournat, "Testing a bead-rod contact with a nonlinear resonance method," *Journal of Sound and Vibration*, vol. 441, pp. 84–95, feb 2019.

[159] K. L. Manktelow, M. J. Leamy, and M. Ruzzene, "Analysis and experimental estimation of nonlinear dispersion in a periodic string," *Journal of Vibration and Acoustics, Transactions of the ASME*, vol. 136, jun 2014.

[160] F. Gao, A. Bermak, S. Benchabane, M. Raschetti, and A. Khelif, "Nonlinear effects in locally-resonant nanostrip phononic metasurface at GHz frequencies," dec 2020.

[161] J. Oliver, F. Press, and M. Ewing, "Two-dimensional Model Seismology," *GEOPHYSICS*, vol. 19, pp. 202–219, apr 1954.

[162] M. V. Wilde, M. V. Golub, and A. A. Eremin, "Experimental and theoretical investigation of

transient edge waves excited by a piezoelectric transducer bonded to the edge of a thick elastic plate," *Journal of Sound and Vibration*, vol. 441, pp. 26–49, feb 2019.

[163] K. L. Johnson, *Contact Mechanics*. Cambridge University Press, may 1985.

[164] *ABAQUS Analysis User's Manual, ed. 6.14*. Providence, IR.: Dassault Systèmes Simulia, 2014.

Appendix A

Fully-Coupled Chains

Dispersion relation for the fully-coupled chains can also be obtained using the dispersion relation of each subsystem (mono-atomic chains). We consider the unit-cell shown in Figure 3.1b and write the final eigenvalue problem following the approach proposed in [1] as

$$\left[\mathcal{K}(\mu) - \omega^2 M\right] e^{ij\mu} = 0 \tag{A.1}$$

where $\boldsymbol{\mathcal{K}(\mu) = \sum_{n=-1,0,1} e^{in\mu} K_n}$. K_n, with $n = -1, 0, 1$ are matrices that define the spring interactiong within a representative unit cell and its adjacent neighbors. For the fully-coupled configuration, this formulation gives

$$\begin{vmatrix} 2k_1(1 - cos\mu) - m_1\omega^2 + k_3 & -k_3 \\ -k_3 & 2k_2(1 - cos\mu) - m_2\omega^2 + k_3 \end{vmatrix} = 0 \tag{A.2}$$

The above may be rewritten in the following form

$$\left| \begin{bmatrix} 2k_1(1 - cos\mu) - m_1\omega^2 & 0 \\ 0 & 2k_2(1 - cos\mu) - m_2\omega^2 \end{bmatrix} + \begin{bmatrix} k_3 & -k_3 \\ -k_3 & k_3 \end{bmatrix} \right| = 0 \tag{A.3}$$

We notice that the diagonal elements in the leftmost matrix represent the dispersion relation for the individual spring-mass lattices. We refer to these as DR_1 and DR_2 to simplify notation. The second matrix shows the effect of connection elements and may be rewritten as the product of two vectors

$$\begin{bmatrix} k_3 & -k_3 \\ -k_3 & k_3 \end{bmatrix} = \begin{bmatrix} k_3 \\ -k_3 \end{bmatrix} \begin{bmatrix} 1 & -1 \end{bmatrix} \tag{A.4}$$

We recall the following matrix lemma:

$$|\boldsymbol{A} + \boldsymbol{u}\boldsymbol{v}^{\boldsymbol{T}}| = |\boldsymbol{A}|(\boldsymbol{1} + \boldsymbol{v}^{\boldsymbol{T}}\boldsymbol{A}\boldsymbol{u}) \tag{A.5}$$

and rewrite the original eigenvalue problem as follow

$$|D| \left(1 + \begin{bmatrix} 1 & -1 \end{bmatrix} D^{-1} \begin{bmatrix} k_3 \\ -k_3 \end{bmatrix} \right) \tag{A.6}$$

where $D = \begin{bmatrix} DR_1 & 0 \\ 0 & DR_2 \end{bmatrix}$. Therefore, dispersion relation for the overall structure may be written in terms of the dispersion relation of each subsystem.

$$DR_1 DR_2 + k_3(DR_1 + DR_2) = 0 \tag{A.7}$$

The first term shows the dispersion relation of the system when k_3 is zero while the second term captures the effect of connection elements in an isolated manner. Extending this type of analysis may offer a means of predicting the dispersive characteristics of a system from its constituents.